Efficient Supply-Modulated Transmitters for Variable Amplitude Radar

by

Andrew H. Zai

B.S., Virginia Tech, 2007

M.S., Virginia Tech, 2011

A thesis submitted to the

Faculty of the Graduate School of the

University of Colorado in partial fulfillment

of the requirements for the degree of

Doctor of Philosophy

Department of Electrical Engineering

2015

This thesis entitled:
Efficient Supply-Modulated Transmitters for Variable Amplitude Radar
written by Andrew H. Zai
has been approved for the Department of Electrical Engineering

_____

Prof. Zoya Popovic

_____

Prof. Dragan Maksimovic

Date _____

The final copy of this thesis has been examined by the signatories, and we find that both the content and the form meet acceptable presentation standards of scholarly work in the above mentioned discipline.

Zai, Andrew H. (Ph.D., Electrical Engineering)

Efficient Supply-Modulated Transmitters for Variable Amplitude Radar

Thesis directed by Prof. Zoya Popovic

This thesis introduces an efficient radar transmitter with improved spectral confinement, enabled by a pulse waveform that contains both amplitude and frequency modulation. The theoretical behavior of the Class-B power amplifier (PA) under Gaussian envelope is compared to that of a Class-A PA. Experimental validation is performed on a 4-W 10-GHz GaN MMIC PA, biased in Class B with a power added efficiency (PAE) of 50%. When driven with a Gaussian-like pulse envelope with a 5 MHz linear frequency modulation (LFM), the PA demonstrates a 31% average efficiency over the pulse duration. To improve the efficiency, a simple resonant supply modulator with a peak efficiency of 92% is used for the pulse Gaussian amplitude modulation, while the LFM is provided only through the PA input. This case results in a 5-point improvement in system efficiency, with an average PAE=40% over the pulse duration for the PA alone, and with simultaneous 40-dB reduction in spectral emissions relative to a rectangular pulse with the same energy.

A measurement bench, which was internally developed, and supply-modulation simulations with Applied Wave Research (AWR) Microwave Office and VSS are also presented. Supply-modulation simulation is helpful for predicting the performance of a supply-modulated system while a well calibrated bench is essential for verification. Both tools are used to demonstrate resonant supply-modulated GaN MMIC PAs.

Lastly, the design of an X-Band GaN Doherty MMIC PA for use in a variable power radar is presented. Simulations and preliminary measurement demonstrate power added efficiency of greater that 40% from 30 to 35 dBm of output power.

To Lindsey.

Acknowledgements

First and foremost, I would like to thank Professor Zoya Popovic for accepting me into her group, funding me throughout my entire program, sending me to France, and helping to sculpt me academically into the person I am today. I have learned a great deal from her and will always look back on my time in the group fondly. My adviser in my masters program, Professor Mili, was one of the first to teach me to think critically at a post-graduate level and he deserves thanks for that. Other professors who helped to inspire me are Professors Maksimovic, Keuster, and Filipovic at University of Colorado, and Professors Pratt, Bostian, and Buehrer at Virginia Tech.

I would also like to thank Dr. Salvador Talisa because he was a great mentor before I started my PhD and was supportive of my decision to pursue the degree, even though he lost an employee. I'm glad I was able to continue working with and look forward to future collaboration. Other noted mentors along my professional development path are David Dutton and Tom Cannon, employees of the Navy.

To former group members, thank you for the lessons you taught me and informative discussions. To current members, good luck with the rest of your program and thank you too for the helpful discussions. Please let me know if you ever discover how ghosts affect the resonant frequency of a cavity. Additionally, thank you Dr. Sardin for your assistance with MMIC design and test bench measurements.

I learned a great deal in my time in Limoges, France, both technically and culturally. This visit would not have been possible without Dr. Tibault Reveyrand being my guardian angel when I first arrived and showing the ropes of both France and XLIM. Also, thank you Professor Nebus

for advising me and technical discussions. The students of XLIM were extremely accepting of a foreigner, something I did not expect but am grateful for. I would especially like to thank Arnaud, Etienne, and Karthik for being great friends.

I would like to thank friends and family for being supportive throughout this process. To my old friends, I'm sorry that I've been less available while in the program and have missed some big events. I hope to see you all more often now that I am finished. Thank you to Uncle Alex and Aunt Julie for being my family for my time in Colorado. Lastly, thank you to Mom, Dad, Natalie, Colette, James, Jacksen, and of course, my future wife Lindsey.

Contents

Chapter

Tables

Table

Figures

Figure

Chapter 1

Introduction

1.1 Microwave Radar Transmitters

The focus of this work is on microwave power amplifiers, specifically for radar, with a secondary consideration of communications power amplifiers. The expectations of a radar power amplifier, or transmitter to be more general, where best said by Skolnik in the *Radar Handbook* [1]. Namely, the transmitter should

> *"provide the necessary transmitted energy with the needed average and peak power, as well as the required stability and low noise for good Doppler processing; operate with high efficiency; have wide bandwidth and be easily tunable; be readily modulated in amplitude, frequency, or phase as necessary; have high reliability and long life; require minimum maintenance; have no dangerous X-ray emissions; require no personnel to operate; be of an affordable price; and be of reasonable size and weight for the desired application."*

This is a long list of demands that proves challenging for all transmitter designers. While this thesis hopes to address as many of the concerns stated above as possible, it mainly focuses on operating with high efficiency while using amplitude modulated waveforms with the goal of spectral confinement. The carrier frequencies considered here are in the 10 GHz range and the power amplifiers are implemented as Monolithic Microwave Integrated Circuits (MMICs) in a wide-bandgap GaN process.

1.1.1 Radar Systems

A block diagram for a general pulsed-Doppler monostatic radar system is shown in Figure 1.1, with the transmitter outlined in red. A direct digital synthesizer generates a baseband pulsed waveform which is typically frequency modulated with a constant amplitude. The pulse is converted to the analog domain and up-converted to the carrier frequency where it is efficiently amplified before being transmitted into free space by the antenna. The signal is scattered off of a target at range, R, and incurs a path loss proportional to $1/R^4$ to account for round-trip propagation. The receive process begins with antenna reception and low-noise amplification. The received pulse is then down-converted to baseband and digitized. After digitization, the signal is processed to determine range, speed, and location. Although radar processing is not the focus of this work, we will discuss later the range resolution (defined below) and total energy of a pulse. It is important to note that in this type of transmitter, there is usually no signal present between pulses and the PA should be turned off to avoid dissipating extra power.

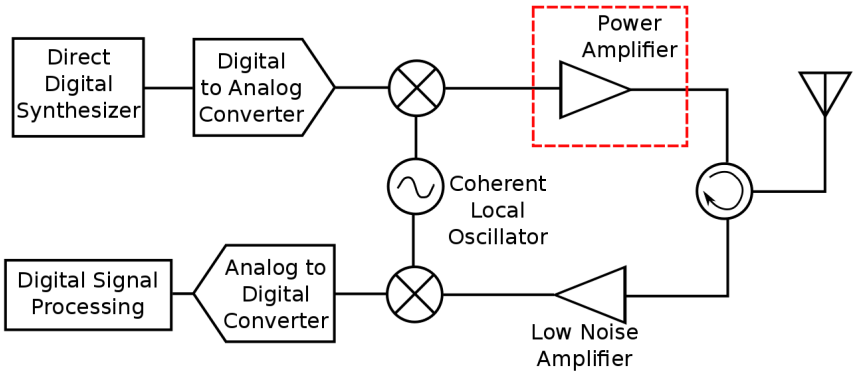

Figure 1.1: This radar system shown above is used to transmit a pulsed waveform which scatters off a target and is then processed by the receiver to discern information about the target. The transmit and receive signal are at the same frequency, aside from any Doppler shift imparted by the target, and are mixed with a coherent source.

1.1.2 Communications Systems

Communications systems use similar analog hardware to a radar system, with the main differences being: (1) radar systems use a waveform of *a priori* known shape; (2) pulsed radar transmitters are off most of the time while communications transmitters have a much higher duty cycle; and (3) the path loss of the signal is proportional to $1/R^2$ instead of $1/R^4$ since it is not a round-trip propagation. The block diagram for a general communications system is shown below [2]. The purpose of the communications system is to transmit and receive data on an up-converted, modulated signal, and a high-level block diagram is shown in Figure 1.2. The transmit portion modulates the digital data stream, then up-converts and amplifies it before free-space transmission. The reverse process amplifies the received signal, down-converts it, and finally demodulates it recover to the data. Another key difference from radar systems is that communications systems typically use separate frequencies for transmit and receive frequency conversion to avoid self-interference.

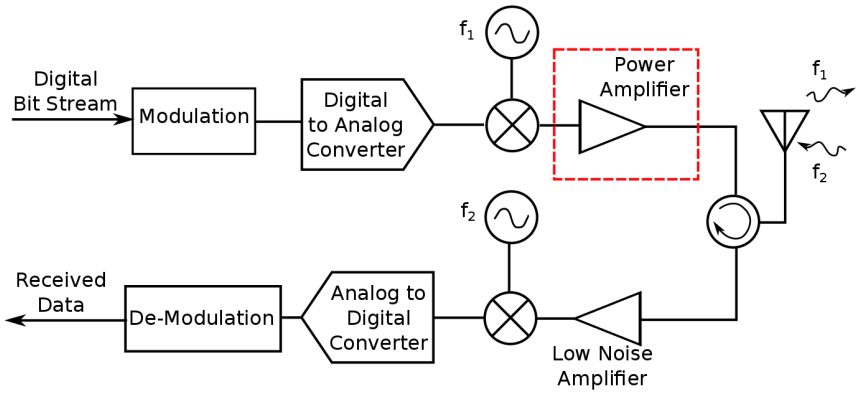

Figure 1.2: A communications system uses similar hardware to a radar system, but transmit and receive up and down-conversion are done at different frequencies to prevent the transmitted signal from leaking through into the receive path.

1.1.3 Vacuum Tube Technologies

The original transmitter sources for radars were vacuum tubes since the transistor was not invented until after decades of radar research had been performed. Although vacuum tube transmitter

technologies do not seem to get as much attention as solid-state ones in terms of development, they are still a vital and irreplaceable component of many fielded high-power radar systems. There is a trend for solid-state technologies to eventually replace all tube technologies, but the high power available from tubes will be difficult and costly to replace [3]. However, solid-state devices are preferable for higher-frequency active phased array systems because of their size and integrability, as well as much lower supply voltages.

Below, a brief history is given of the development of tube technologies as related to their use in radar. A performance range for the dominant tube technologies in radar: gridded tubes, magnetrons, klystrons, Traveling Wave Tubes (TWTs), and gyrotrons is also discussed. For a more detailed account of the history of tube technologies, an excellent reference is [4]. A more thorough account of the technology characteristics is given in [5]. Lastly, to gain a deeper understanding of the theory involved with vacuum tube technology, reference [6] is recommended.

The first type of amplifier to be used in radar systems was the gridded tube, or triode [5]. This type of technology uses a heated cathode to supply a flow of electrons towards an anode with a grid between the two. The voltage applied to the grid controls the flow of electrons between the cathode and anode which is the mechanism controlling the output signal of the device. Gridded tubes were an active area of research for radar transmitters prior to World War II, but could not be operated above UHF. Modern gridded tubes can supply output powers on the order of tens of kilowatts at 1 GHz, and Watts at 10 GHz. A particularly interesting gridded tube is the constant-efficiency amplifier [3], such as one made by L-3 Communications. It is able to maintain high-efficiency levels when backed of 13 dB from peak output power. It operates at UHF and is popular among television broadcasters.

In World War II, both sides had knowledge of radar principals by the start of the war [4]. However, the Allies developed the magnetron (in Britain) which allowed them to implement microwave radar. This and sensitive receivers (in the United States) allowed them to more accurately detect enemy air-raids, as well as mount radar on aircraft, a decisive advantage in hunting bombers. Typical magnetron performance at the time was 500 kW peak power for a device tunable from 1250

- 1350 MHz. Modern devices in that frequency range can achieve megawatt peak power levels, or reach 240 W at 10 GHz. Magnetrons are relatively cheap compared to other technologies and provide high power levels with relatively high efficiency. The drawback to the technology is that it is an oscillator, not an amplifier. This means that it is only able to generate tones, either pulsed or continuous wave (CW), and cannot generate more advanced modulated waveforms used in modern radars.

The klystron was actually invented before the magnetron by the Varian brothers, but at the time it was too low-power to be of interest for radar. The klystron was first used by the linear accelerator community and later adopted by the radar community when promising results were shown in 1953 with an S-Band klystron capable of 20 MW peak power. Since then, it has become a staple of high-power transmitters for radar applications and has even be quoted as being "*the first microwave power source to consider when designing a new high-performance radar* [1]." Klystron sources are capable of generating megawatts of power to X Band, and in the 10 W range at W Band. Their major drawbacks are they have limited bandwidth because of their use of resonant cavities, require high supply voltages (kilovolts), and have reliabilities from 5000 to 75000 hours [7].

The TWT is another type of linear-beam tube, but has a wider bandwidth than the klystron because it does not rely on resonant cavities, with octave-wide bandwidths possible. At lower frequencies, they have lower power than klystrons but higher power at high frequencies. The TWT can attain 200 kW of output power at 1 GHz and 800 W power at 100 GHz. The TWT demonstrates lower reliability than the klystron with only 2000 to 18000 hours of mean time between failure demonstrated [7].

If one were looking for the highest power attainable at high frequencies, the gyrotron would be the best choice. Gyrotrons have output powers of greater than 500 kW at 100 GHz and 1 kW at 400 GHz! The most notable use of a gyrotron in a radar was the Warloc system built by the Naval Research Laboratory. It operated at 94.2 GHz with a peak power of 102 kW [1]. However, it requires cryogenics to cool a large super-conducting magnet.

1.1.4 Solid-State Technologies

Although radar transmitters used to be be exclusively the domain of tube-type transmitters due to the power levels required, solid-state technologies have increasingly been incorporated due to their benefits over tubes: they do not require a hot cathode; they operate at a much lower voltage (volts instead of kilovolts); and they demonstrate higher longer lifetimes than tubes since they do not require a hot electron source that wears out [1]. Although silicon bipolar junction transistors have demonstrated their ability to produce power at microwave frequencies, it is more profitable for silicon foundries to fabricate digital components. For silicon-based technologies, LDMOS is the preferred high-power technology and is popular for cellular base-station transmitters [8]. LDMOS is capable of working through S-band where it is able to generate hundreds of watts of power [9], but it has recently demonstrated 1.5 watts as high as 6 GHz [10].

Since the power density of CMOS silicon is relatively low at high frequencies, compound semiconductors such as GaAs, InP, and GaN were developed. A common measure for power density is W/mm, which describes how much power a technology can reliably handle within a given gate periphery. While silicon has densities of about 0.8 W/mm, GaAs and GaN demonstrate 1-2 W/mm and 3-10 W/mm, respectively. Initially, GaAs and InP were the only solid-state technologies available from S Band through W Band [11], but GaN is acquiring more market share due to its significantly higher power handling abilities. Solid-state GaN PAs have demonstrated 100 watts at C Band [12], which is orders of magnitude higher than LDMOS. GaN is still capable of high powers at Ku Band with 60-watt PAs demonstrated [13], and gain demonstrated up to W Band [14]. The remainder of this work will focus exclusively on GaN technology where single-chip power levels of 10 watts have been demonstrated at 10 GHz [15]. However, the generalized theory and approach can be extended to any technology.

The decision to use vacuum tube or solid-state technology in radar transmitters depends largely on the radar architecture. If the radar uses a phased-array antenna, the placement of the PA in the antenna determines which type of technology is most appropriate. Figure 1.3 shows a

simplified block diagram for both a passive and active phased array. In a passive array, there is one PA for the entire array and this PA must supply all of the power. For an array radar which requires megawatts of power, tube-based technologies are the best solution. However, solid-state technologies are suitable for an active array with a PA in every antenna element because the total power from all PAs in the array can spatially combine to rival the power from a single tube-based transmitter.

1.1.5 Conservation of Power and Linearity

To understand the compromise between linearity and efficiency, Poynting's theorem [16] can be used, which is written as

$$\oint_{\mathbf{S}} (\mathbf{E} \times \mathbf{H} \cdot d\mathbf{S}) = -\frac{\partial}{\partial t} \int_v \left[\frac{1}{2}\epsilon E^2 + \frac{1}{2}\mu H^2 \right] dv - \int_v \sigma E^2 dv. \tag{1.1}$$

and says that the power leaving a volume plus the change in stored energy and dissipated power equals zero. For a wave with a constant envelope and time-harmonic electric and magnetic fields, as is the case with a CW signal in a power amplifier, the change in stored energy is zero. The only powers present are those shown in Figure 1.4.Substituting the powers from Figure 1.4 into (1.1) and rearranging them results in

$$P_{In} + P_{DC} = P_{Diss} + P_{Out} + P_{Radiated} \tag{1.2}$$

as shown in [17]. It is normally assumed that $P_{Radiated} = 0$. A metric for efficiency is defined

$$\eta_{Drain} = \frac{P_{Out}}{P_{DC}} \tag{1.3}$$

where η_{Drain} is the drain efficiency. and the gain is defined as

$$G = \frac{P_{out}}{P_{In}}. \tag{1.4}$$

Equation (1.3) does not include the input power, and thus leaves out the influence of the gain in its definition; however, gain can be accounted for by defining a new metric for efficiency

$$\eta_{PAE} = \frac{P_{Out} - P_{In}}{P_{DC}} \tag{1.5}$$

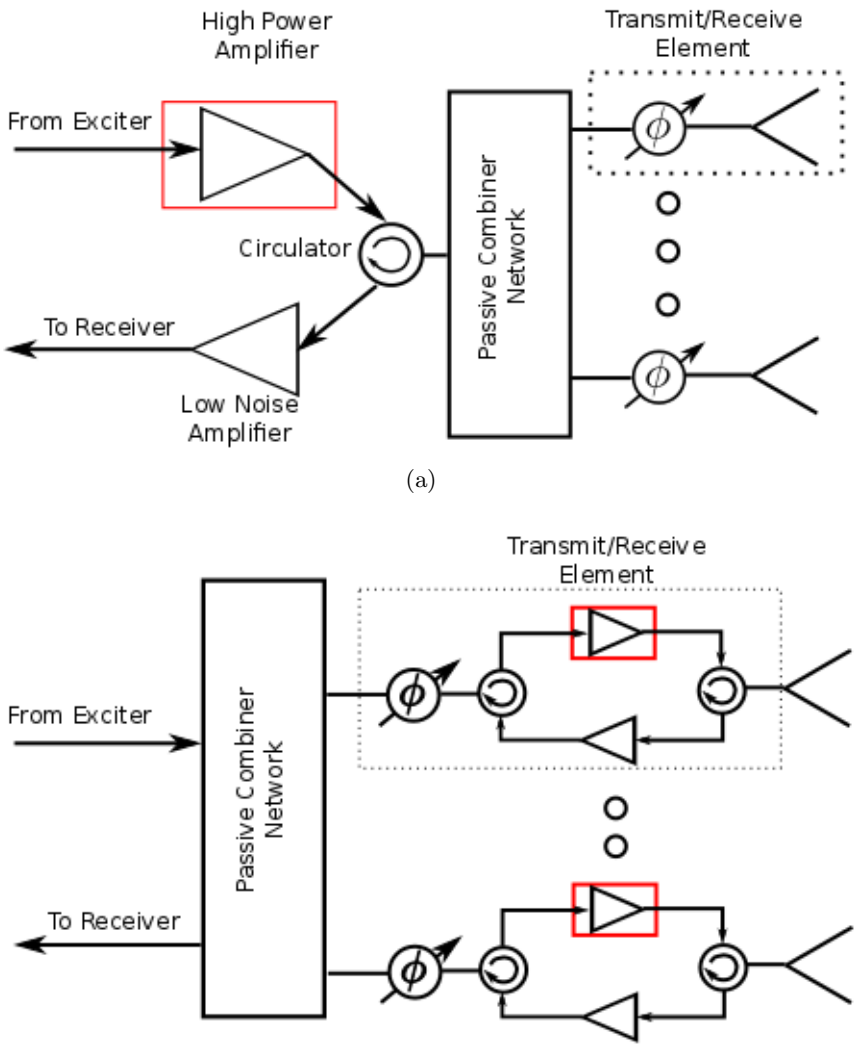

Figure 1.3: Differences in the architectures of a passive (a) and active (b) phased-array radar. Both architectures use many elements with progressive phase delays to electrically steer the direction of the transmitted wave. The passive array relies on one PA to supply all of the power for the radar while the active array distributes the power amongst PAs at every element of the array which then spatially combine in the far field. Vacuum tubes are more appropriate for passive arrays because of their high transmit power while solid-state PAs are better for active arrays because of their size.

where η_{PAE} is the Power Added Efficiency (PAE). Equations (1.2), (1.4), and (1.5) can be combined into

$$\eta_{PAE} = (G-1)\frac{P_{In}}{P_{DC}} \tag{1.6}$$

to show that linearity and efficiency are directly at odds with one another. It is obvious from 1.6 that for a constant P_{DC} and gain, and thus linear amplifier, that a decrease in P_{In} results in a decrease in efficiency. This shows that a linear amplifier with constant bias cannot maintain peak efficiency when its P_{In} is decreased.

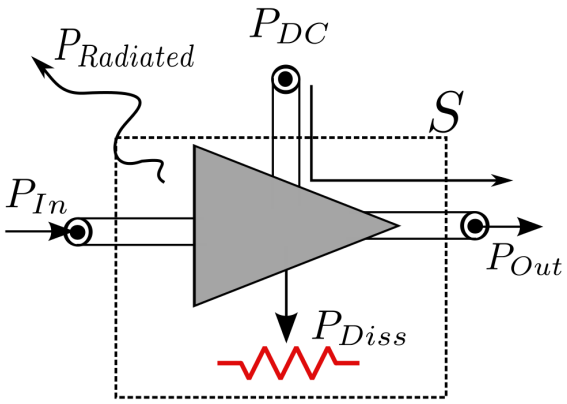

Figure 1.4: When a surface is drawn around a power amplifier with no change in the stored electric or magnetic field, the power leaving the volume plus the dissipated power is equal to zero.

Power amplifiers that use only a single transistor or do not use any special high efficiency architectures have only three ways to improve their PAE: (1) to decrease P_{DC}, (2) to increase P_{Out} without increasing P_{DC}, or (3) to decrease P_{Diss}. The first method can be done using a reduced conduction angle amplifier, such as Class-B [18]. The second can be done by driving the amplifier into compression, but this has diminishing returns, does not have constant gain, and can be damaging to the transistor. Lastly, reducing the dissipated power can be done using switched mode PAs which use waveform shaping [19][20]. However, all of these approaches add harmonic content and operate the transistor in the non-linear region of the transconductance curve, thus making them non-linear.

1.2 Overview of Efficient PAs with a Peak-to-Average Ratio

It was shown in (1.6) that linearity and efficiency are directly at odds with each other when only a single transistor is used in the PA. However, techniques which maintain linearity and effi-

ciency for backed-off power levels do exist, but all require two amplifiers. These architectures are supply modulation, the Doherty, and outphasing which are described below.

1.2.1 Supply Modulation

Traditionally, amplifiers are biased so that there is sufficient DC power at the drain of the transistor to supply for peak output RF power conditions. If one must us only a single drain supply voltage, it makes sense to choose a voltage which will provide for the peak power. However, when the amplifier is backed-off from peak power the extra DC power must be dissipated in the transistor since it is not being transformed into useful RF power. The first method of supply modulation was proposed by Kahn [21] and is today known as Envelope Elimination and Restoration (EER); however, we will start our discussion of supply modulation by talking about Envelope Tracking (ET).

Figure 1.5 shows what the PAE looks like for a typical power amplifier plotted against output power. In the case of a constant amplitude signal, the amplifier is always operating at its peak efficiency point. When the signal has a high Peak-to-Average Power Ratio (PAPR) and thus varying envelope, the amplifier is forced to operate in less efficient regions, as shown in Figure 1.5.

One way to compensate for the lower efficiency in backed off regions is to lower the drain voltage; which increases the efficiency for the lower output powers. To understand why lowering the drain voltage improves efficiency, consider the IV curves and load line of the Class-A amplifier in Figure 1.6. This class is not conducive to efficiency, but it is beneficial for a pedagogical explanation of envelope tracking.

For a Class-A amplifier to generate the maximum output power for a transistor, it must be biased in the middle of the IV curves so it can swing from I_{max} to V_{max}, as illustrated by the dashed red line. The bias in this case would be $V_{bias} = \frac{V_{max}-V_{knee}}{2} + V_{knee}$ and $I_{bias} = \frac{I_{max}}{2}$. In this configuration, the transistor would be able to supply

$$P_{out} = \frac{(V_{max} - V_{knee})\, I_{max}}{8}. \tag{1.7}$$

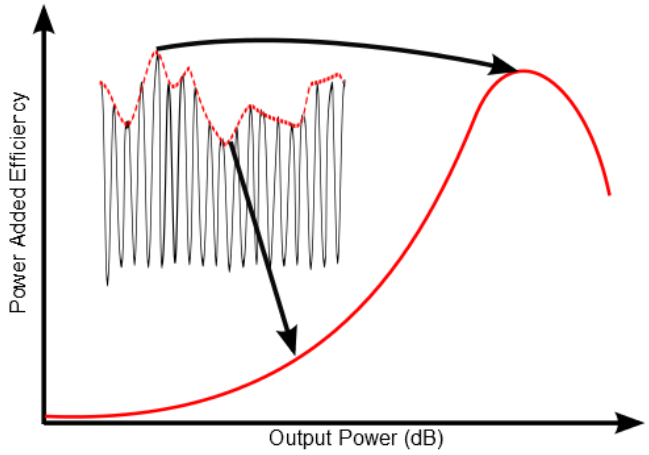

Figure 1.5: This shows how the efficiency decreases for signals with a non-constant envelope. The function of efficiency versus power takes the shape of the curve drawn above. While a constant envelope signal can always operate at peak efficiency, an amplitude modulated signal can not and must operate in backed-off, low-efficiency regions.

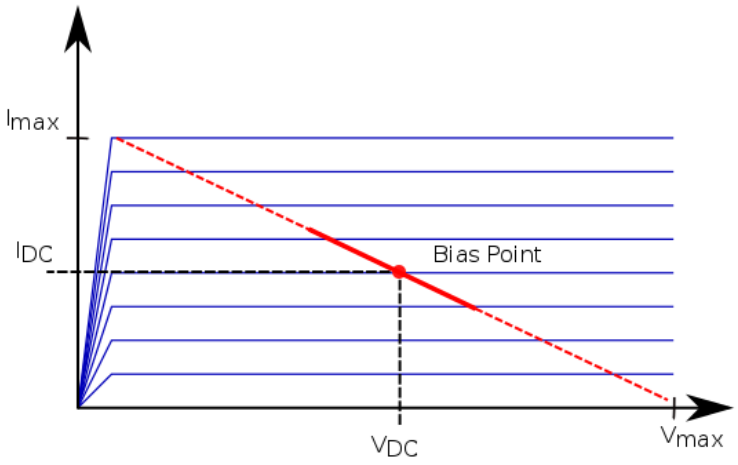

Figure 1.6: When biasing a device for Class-A operation, it is biased for the situation with the highest output power. This requires the quiescent current and voltages to be at half of their maximum values. Although this bias point allows for peak output power, it also has a high level of DC power consumption, even at lower output power levels.

Now consider the case when less power is needed from the transistor. The load line for this case is drawn with a solid red line in Figure 1.6. Even though less RF power is being generated by the transistor, the transistor still has the same supply voltage and average current, and thus

DC power, more of which must be dissipated as heat. Rather than keep this bias point, it is more efficient to adjust the bias voltage so that only enough is present to allow for the necessary load line swing, as shown in Figure 1.7. In this case, the load line is still able to swing to both of its peaks without saturating or cutting off but requires less supply voltage and DC power. In the case of Class-A amplifiers the average current does not decrease for lower power levels, but it does for classes with reduced conduction angles such as Class-B.

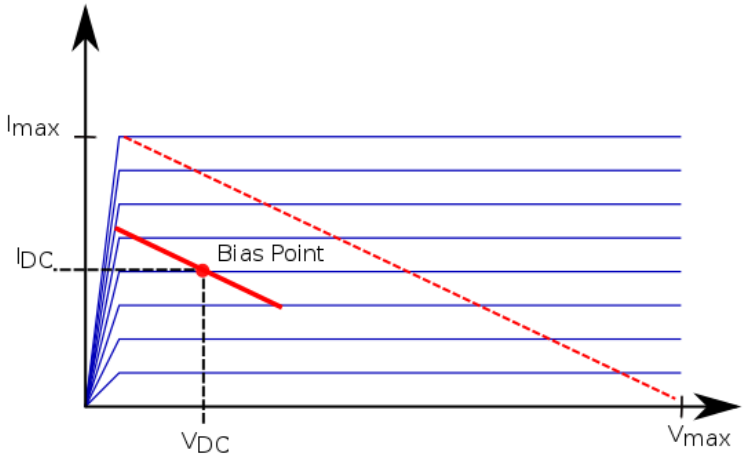

Figure 1.7: If one were able to decrease the bias voltage of the device when the full output power is not used, there would be a reduction in the DC power needed. This is how supply-modulation is able to improve efficiency over static bias conditions.

When the PAE curves are drawn for swept drain voltages, the peak in efficiency occurs at a lower power as shown in Figure 1.8. Instead of tracing the efficiency of the maximum bias voltage, envelope tracking allows for the efficiency to follow the peaks of the swept bias voltage, a dramatic improvement. This exercise was shown for Class-A amplifiers, but the same principles apply for other classes of operation.

Envelope tracking adjusts the voltage to ensure that only enough voltage bias is present as is needed for the varying envelope of the input signal. EER on the other hand, uses the bias voltage to shape the output waveform. An input signal with a constant amplitude is applied to the amplifier and the supply level adjusts the gain of the amplifier to shape the output. When

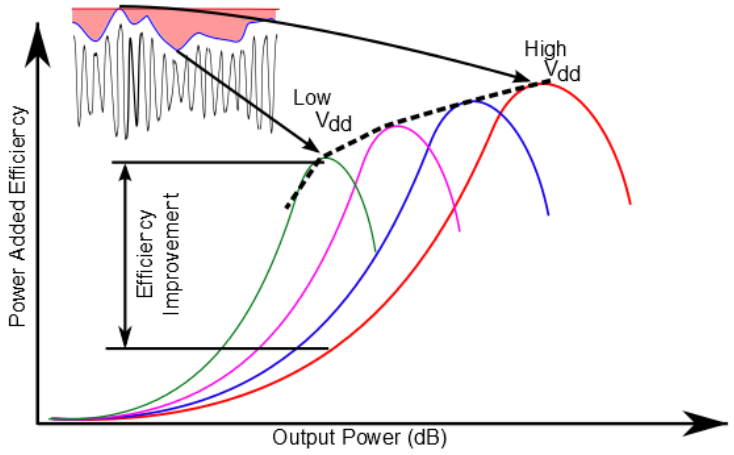

Figure 1.8: To get an idea of how supply modulation improves the efficiency, the efficiency curves can be drawn for several static bias conditions. The supply modulated efficiency can be designed to follow the peak efficiencies of these bias conditions.

Kahn first conceptualized this mode of supply modulation he proposed a Class-C amplifier be used; however, nowadays switched mode amplifiers are typically used. EER requires a highly compressed amplifier and thus is a highly non-linear technique. Envelope tracking on the other hand, while it does not improve the linearity of an amplifier, is certainly more linear than EER.

1.2.2 Doherty

Another topology for high backed-off efficiencies is the Doherty power amplifier which demonstrates two efficiency peaks 6 dB apart, in the theoretical analysis. The Doherty uses two RF PAs in parallel as shown in Figure 1.9. The carrier amplifier is biased such that it is always on in Class AB or Class B, while the peaking amplifier is biased in Class C so that it is normally off. When the input power is sufficiently high, the peaking amplifier turns on. Although it is not usually explicitly stated, it is assumed that the carrier and peaking amplifiers are pre-matched into a $50\,\Omega$ system. When this is the case, $Z_L = \frac{Z_0}{2} = 25\,\Omega$.

In the regime where only the carrier amplifier is on, the peaking amplifier presents an open circuit in parallel with the load. Thus, the impedance seen by the carrier PA is adjusted by the

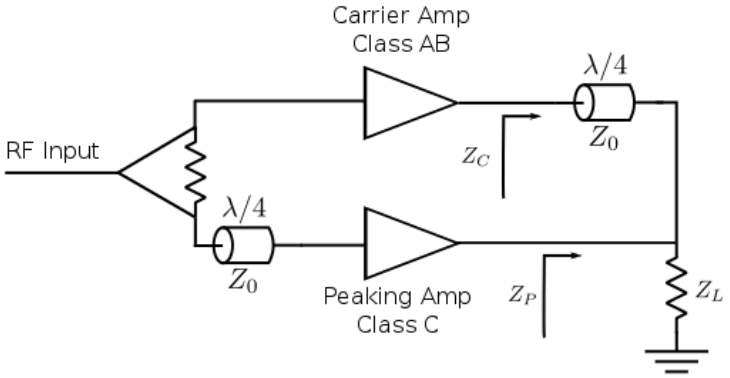

Figure 1.9: Block diagram for a Doherty power amplifier consisting of a carrier amplifier, which is always on and biased in Class AB, and a peaking amplifier, which is biased in Class C.

quarter-wave transformer to

$$Z_C = \frac{Z_0^2}{Z_L} = 100\,\Omega. \tag{1.8}$$

For a standard PA topology, the load impedance is static. However, in the Doherty architecture, the peaking amplifier is designed to turn on when the carrier reaches saturation. When this happens, the impedance seen by the carrier amplifier can be written as

$$Z_C = \frac{Z_0^2}{Z_L\left(1 + I_P/I_C\right)} \tag{1.9}$$

where I_P and I_C are the magnitudes of the fundamental current for the peaking and carrier amplifiers. By turning on the peaking amplifier when the carrier amplifier is about the saturate, the carrier amplifier is load-pulled so that it is not saturated. At peak output power, $Z_C = 50\,\Omega$. When turned on, the peaking amplifier sees an impedance of

$$Z_P = Z_L\left(1 + I_C/I_P\right), \tag{1.10}$$

which also is $50\,\Omega$ at peak output power. By load-pulling the impedances seen by the two amplifiers in this topology, they are both able to remain in a non-compressed mode of operation across a wider range of output powers than traditional PA topologies.

1.2.3 Outphasing

The last technique for efficient backed-off transmission is outphasing, first proposed by Chirex in 1935 [22] and a simplified diagram of the system is shown in Figure 1.10. The technique uses two efficient, non-linear PAs combined at their output. The amplifiers are individually driven at their peak output power so they are able to maintain efficient operation. Amplitude modulation is achieved by varying the phase for each PA with the outphasing block at the PA input ports. If the goal of the transmitter is to amplify the signal

$$s(t) = A(t)\sin\left(\omega t + \phi(t)\right) \tag{1.11}$$

where $A(t)$ is the amplitude modulation, ω is the carrier frequency, and $\phi(t)$ is the phase modulation, then the amplitude modulation is imparted on the output signal by adding $\theta(t)$ to PA 1, and subtracting $\theta(t)$ from PA 2. The value of $\theta(t)$ is calculated in the outphasing block as

$$\theta(t) = \cos^{-1}\frac{A(t)}{A_{max}} \tag{1.12}$$

where A_{max} is the maximum output amplitude of the transmitter. Thus, the signal entering PA 1 is

$$s_1(t) = \frac{A_{max}}{2}\sin\left(\omega t + \phi(t) + \theta(t)\right) \tag{1.13}$$

and

$$s_2(t) = \frac{A_{max}}{2}\sin\left(\omega t + \phi(t) - \theta(t)\right) \tag{1.14}$$

enters PA 2. The output combiner follows the trigonometric identity

$$\sin(u) + \sin(v) = 2\sin\left(\frac{u+v}{2}\right)\cos\left(\frac{u-v}{2}\right) \tag{1.15}$$

thus giving the output signal $Gs(t)$. Much like the Doherty, the bandwidth of the transmitter is limited by the combiner network. Additionally, the PAs are always operating at peak output power, even when the transmitter is backed off. This means that the excess power is either reflected into the PAs or dissipated by the combiner network, hardly improving the overall efficiency. However, there is work focusing on how to reuse this extra power [23].

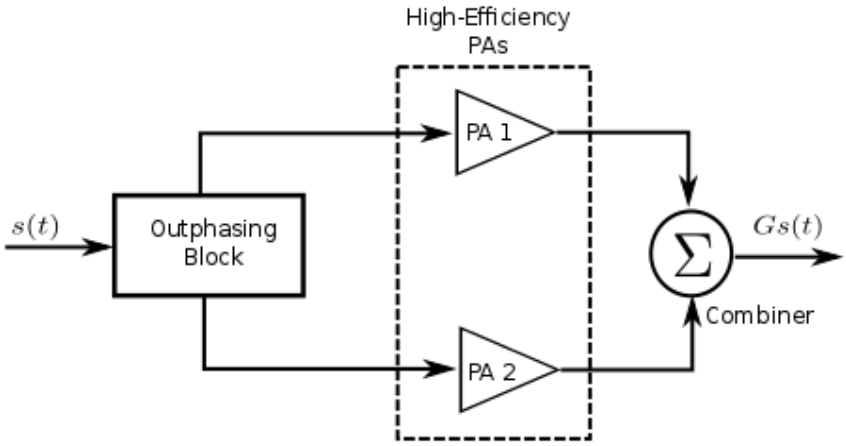

Figure 1.10: A block diagram for the outphasing architecture which uses two high-efficiency PAs operating at peak power. The outphasing block adds a phase $\theta(t)$ to PA 1 and subtracts it from PA 2. The value of $\theta(t)$ is solved by (1.12).

1.3 Definitions

1.3.1 System Definitions

Signal Envelope: When discussing the envelope of a signal, it is referring to the amplitude modulated portion. In a baseband signal

$$s_{BB}(t) = A(t)e^{\phi(t)} \tag{1.16}$$

or signal at a carrier frequency

$$s_{RF}(t) = A(t)e^{j\omega t+\phi(t)} \tag{1.17}$$

$A(t)$ is the envelope, $\phi(t)$ is the phase modulation, and ω is the carrier frequency.

Supply Modulator Trajectory: A function used to determine the supply modulator output voltage for a given PA input power level. This is determined by empirically measuring the characteristics of the PA, such as output power and efficiency, for swept values of input power and drain bias. With this data, the drain voltage is chosen which optimizes a PA characteristic, usually efficiency, for a given PA drive level.

Transmitter Linearity: A system is defined to be linear if its input signal, $x(t)$, and output signal, $y(t)$, obey superposition. This can be simplified by the statement

$$ax_1(t) + bx_2(t) = ay_1(t) + by_2(t) \tag{1.18}$$

where a and b are complex constants [24].

Non-linearity is introduced by operating the transistor in a non-linear fashion, such as compressing the amplifier. The two effects of non-linearity are: (1) an amplitude distortion which changes the signal of interest; (2) added frequency components in the spectrum which cause interference.

Adjacent Chanel Power Ratio: The intermodulation products can be measured by the Adjacent Chanel Power Ratio (ACPR) which is defined as

$$ACPR = \frac{\int_{f_c - \frac{BW}{2}}^{f_c + \frac{BW}{2}} P(f)df}{\int_{\left(f_c + BW + \delta - \frac{BW}{2}\right)}^{\left(f_c + BW + \delta + \frac{BW}{2}\right)} P(f)df} \tag{1.19}$$

where $P(f)$ is the power spectrum as a function of frequency and δ is an arbitrary guard offset.

Peak-to-Average Power Ratio: Power amplifiers have a point of maximum efficiency which is in the compressed region. As the amplifier is driven with less input power it becomes less efficient because the amplifier is no longer producing as much output power but is still requires bias voltages and currents. Since the bias is still on and less power is going to the output, the power is thus being dissipated by the transistor.

Signals with a constant amplitude are convenient for use in a power amplifier because they can always operate at their point of maximum efficiency. However, signals with an envelope

$$v_{env}(t) = A(t) \tag{1.20}$$

decrease the efficiency because the portions of the signal with lower amplitude cause higher dissipation in the transistor. These signals are said to have a Peak-to-Average Power Ratio

(PAPR) with

$$PAPR = 20log\frac{maximum(v_{env(t)})}{mean(v_{env(t)})} \tag{1.21}$$

and a higher PAPR being more taxing on the efficiency of a power amplifier because the average power level is further backed off from peak efficiency.

Matched Filter: Received signals are filtered in the time domain with the convolution integral

$$s_o(t) = \int_{-\infty}^{\infty} s(\tau)h(t-\tau)d\tau \tag{1.22}$$

or with multiplication in the frequency domain

$$S_o(f) = S(f)H(f). \tag{1.23}$$

In the above equations $s(t)$ and $s_o(t)$ are the input and output signals of the filter $h(t)$. It has been shown that the filter which provides the highest signal to noise ratio is the matched filter [25]. The matched filter is represented mathematically as

$$h(t) = Ks^*(t_0 - t) \tag{1.24}$$

in the time domain or

$$H(f) = KS^*(f)e^{j2\pi f t_0} \tag{1.25}$$

where K is a constant and t_0 is the delay corresponding to the range bin being processed. The matched filter can be thought of as a delayed mirror image of the transmitted signal in the time domain [25]; however, it is usually easier to perform the filtering, in a computational sense, in the frequency domain. This is because it is easier to multiply two spectra than convolve a time series. A representation of the receive and filter process is shown in Figure 1.11.

Power Added Efficiency The Power Added Efficiency (PAE) is the average PA efficiency over the signal with a varying amplitude, while the Composite Power Added Efficiency (CPAE) is

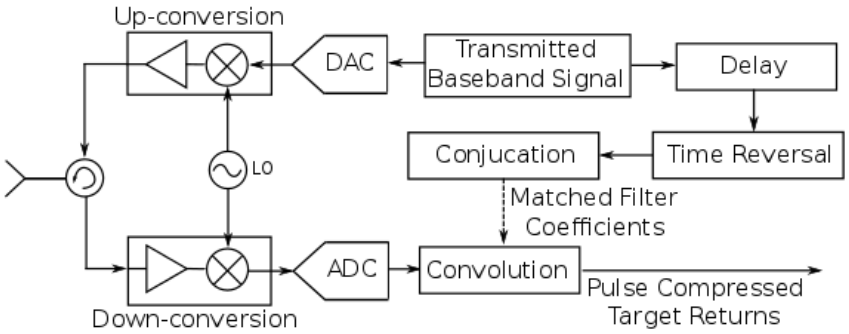

Figure 1.11: Representation of how the matched filter is implemented. The target return is amplified and down-converted to baseband by a quadrature receiver, then sampled by an analog-to-digital converter. The matched filter is then applied in the digital domain to compress the signal.

the total efficiency including the fixture losses,supply modulator efficiency and PA efficiency, defined as:

$$PAE = \frac{\int_0^T P_{out}\,dt - \int_0^T P_{in}\,dt}{\int_0^T V_{ds}\,dt \int_0^T I_{ds}\,dt} \tag{1.26}$$

$$CPAE = \frac{\int_0^T P_{out}\,dt - \int_0^T P_{in}\,dt}{V_{DD} \int_0^T I_{ds}\,dt} \tag{1.27}$$

where V_{DD} is the DC supply voltage of the supply modulator and T is the time over which the measurement is performed. These equations are used when our measurements do not provide access to time domain current data, only the average current. If another definition of PAE or CPAE is used in this thesis, it will be specifically defined.

1.3.2 Radar Definitions

Detection Threshold: Since radar signals are received in the presense of noise, radar operators must choose a detection threshold to signify when a target echo has been received. This threshold should be high enough that low levels of noise power do not trigger false alarms, but not so high that legitimate target signals are rejected. The selection of this threshold is the result of a statistical analysis of the noise and the noise plus target signal which maximizes the probability of detection for a given probabilty of false alarm.

Probability of False Alarm Based on the detection threshold, it is the probability that noise will indicate a target when no such target is present. This metric should be minimized.

Probability of Detection The probablility that a target with a given radar cross section will be detected with the current detection threshold. This value should be as high as posssible so that legitimate targets are not ignored.

Radar Range The range of a radar is determined by the power of the transmitter, the size of the target, and the sensitivity of the receiver. Consider a Continuous Wave (CW) signal with mono-static boresight transmission and reception. The power density received from the target will be

$$P_r = S_{target}\frac{\sigma}{4\pi R^2}A_e = \frac{P_t G^2 \lambda^2 \sigma}{(4\pi)^3 R^4} \tag{1.28}$$

where S_{target} is the transmitted power density at the target, σ is the radar cross section of the target, R is the range to the target from the radar, and A_e is the effective area of the receive antenna [26]. We were able to arrive at the right most expression of (1.28) by applying the definition of effective aperture area

$$A_e = G\frac{\lambda^2}{4\pi} \tag{1.29}$$

where G is the gain of the antenna.

As with all communications systems, the received signal competes with receiver and antenna noise. The noise power present is equal to

$$P_n = k(T_A + T_r)B \tag{1.30}$$

where $k = 1.38x10^{-23}$ J/K (Boltzmann's constant), T_A is the antenna noise temperature, T_r is the receiver noise temperature, and B is the receiver noise equivalent bandwidth [27]. With (1.28) and (1.30), the Signal-to-Noise Ratio (SNR) of the target echo can be written as

$$\frac{P_r}{P_n} = \frac{P_t G^2 \lambda^2 \sigma}{(4\pi)^3 R^4 k T_0 B} \tag{1.31}$$

where $T_0 = T_A + T_r$. In order to detect the target, the SNR must exceed the detection threshold, δ_t, which is determined by detection theory to provide for a certain probability of false alarm (P_{fa})[28]. This requirement is expressed as

$$\frac{P_t G^2 \lambda^2 \sigma}{(4\pi)^3 R^4 k T_0} > \delta_t \tag{1.32}$$

and can be re-written as

$$R \leq \sqrt[4]{\frac{P_r}{P_n \delta_t}} = R_{max}. \tag{1.33}$$

Eq. (1.33) states that characteristics G, λ, T_0, P_t of a radar and σ of a target result in a maximum detectable range R_{max}. This model considers only one pulse and does not consider the processing gain of integrating pulses. Additionally, it does not include the effects of atmospheric propagation which has a tremendous impact on how the radar performs. However, since the purpose of this work is to compare single pulses, these complicating additions to the model are omitted.

Range Resolution: The range resolution of a rectangular pulse is $T_p c/2$, where T_p is the pulse width and range resolution is directly proportional to it [29]. A shorter pulse has smaller, and thus better, range resolution. As the name implies, range resolution is a measure of how well the waveform can distinguish to closely spaced targets. The range resolution is solved for by applying a radar waveform to its matched filter and measuring the distance between the two half amplitude points[1] .

Range Bin: Based on the time between pulses, or Pulse Repetition Interval (PRI), radars have a maximum unambiguous range of

$$R_{max-u} = \frac{c t_{PRI}}{2} \tag{1.34}$$

where c is the speed of light and t_{PRI} is the PRI. This is not to be confused with R_{max} which is based on received power. Rather, it tells the maximum range a radar operator can

[1] It should be noted that the output of a matched filter is a voltage signal even though the filter is squaring the matched input signal. Thus, the range resolution is measured from 0.5 on the normalize linear scale, or -6 dB on the normalized decibel scale.

be certain a target echo comes from the current and not the previous pulse. The distance from where the radar is located to the maximum unambiguous range is the range profile. The range profile is divided into units called range bins which are as wide as the range resolution of the radar. When a target is identified, its distance is annotated by its range bin.

Time-Bandwidth Product: The range resolution of an un-modulated pulse is inversely proportional to the pulse width. The range resolution can be improved by adding phase or frequency modulation. The time-bandwidth product is the product of the pulse width and bandwidth of the modulation. For a given modulated pulse, its range resolution improvement is directly proportional to the time-bandwidth product. That is to say, a pulse with a time-bandwidth product of 10 has a range resoultion 10 times better than the same pulse without modulation.

1.4 Thesis Outline

This thesis introduces an efficient radar transmitter with improved spectral confinement, enabled by a pulse waveform that contains both amplitude and frequency modulation. The thesis is organized as follows:

- Chapter 2 presents the theory comparing a rectangular pulse to a Gaussian shaped envelope in terms of the range resolution, pulse energy, and spectral confinement. When the energy inside the envelope is kept constant, it is shown that a Gaussian type envelope results in elimination of out-of-band emissions which is a considerable improvement over a rectangular pulse. In addition, the pulse-compressed response of a Gaussian pulse does not have the -13 dB time side lobes that a rectangular pulse does. The use of a Gaussian shaped pulse decreases the efficiency of the PA, but analysis shows that the efficiency can be recovered by supply modulation. Theoretical efficiency of different classes of amplifiers under supply modulation is also presented, with a conclusion that Class-B PAs are well suited for this

transmitter architecture.

- There are no standard tools for analyzing supply-modulated transmitters, especially in the case of radar. Chapter 3 describes a simulation environment developed for such transmitters. System level simulations which include the digital baseband signal are combined with microwave harmonic balance simulations with non-linear GaN transistor models. The simulation environment is designed to correspond closely to a hardware test bench which is also described in this chapter and used to evaluate well-known communications type signals amplified by supply-modulated transmitters.

- Chapter 4 develops the implementation of a Gaussian-type envelope transmitters for radar. A Class-B X-Band GaN MMIC is measured in two modes: (1) drive-modulated and (2) supply-modulated. For supply modulation, a simple resonant modulator is developed and implemented with inexpensive off-the-shelf components. The supply modulator is capable of producing pulses of various widths and amplitudes, between 7-15 μs and up to 20 V. The pulse width is controlled digitally. Both simulations and measurements of a resonant supply-modulated X-Band GaN MMIC demonstrate that this topology provides an improved efficiency relative to a system using a constant supply.

- Chapter 5 introduces a new variable power radar concept which uses resonant supply modulation. The envisioned radar transmitter is required to support three distinct power modes designed to provide increased capabilities for shorts bursts of time. An X-Band GaN Doherty MMIC is designed as the basic PA that can support these advanced radar transmitter specifications.

- Finally, some conclusions are drawn and suggestions for future work are outlined in Chapter 6 along with a summary of thesis contributions.

Chapter 2

Radar Signals with Amplitude Modulated Pulses

The National Telecommunications and Information Administration (NTIA), the organization which regulates spectrum allocated to the federal government, places strict requirements for out of band emissions by any transmitter. These requirements are known for radar as the Radar Spectrum Engineering Criteria (RSEC) and are described in chapter five of the NTIA manual [30]. The RSEC impose a spectral mask for radar transmitters which is depicted in Figure 2.1. The mask is split into three regions: the in-band, out-of-band, and spurious. The in-band and out-of-band bandwidths depend on characteristics such as pulse width and time-bandwidth product. There are no regulations for the in-band signal aside from the peak power. A taper is present for the out-of-band region to which the radar must comply. There is a strict mathematical description of the taper, but can be simplified by stating it increased from 40 dB below peak transmitter power, at the near edge of the in-band region, to 60 dB below at the far edge. Beyond the out-of-band region, in the spurious region, transmitter emissions must be 60 dB below peak power. The exact limits and widths of the regions are different for different classes of radar, but the spurious region can have limits as strict as 80 dB below peak power.

Radar transmitters generally have very poor spectral properties that do not comply with RSEC unless special precautions are taken. It will be shown in this chapter that high spectral side lobes are inherent to the rectangular pulse and are due to the fast rise and fall times. Techniques have been used for decades to improve the spectrum of pulsed radars. Slowing down the rise and fall times of the pulse has been shown to improve the spectral properties at the cost of power

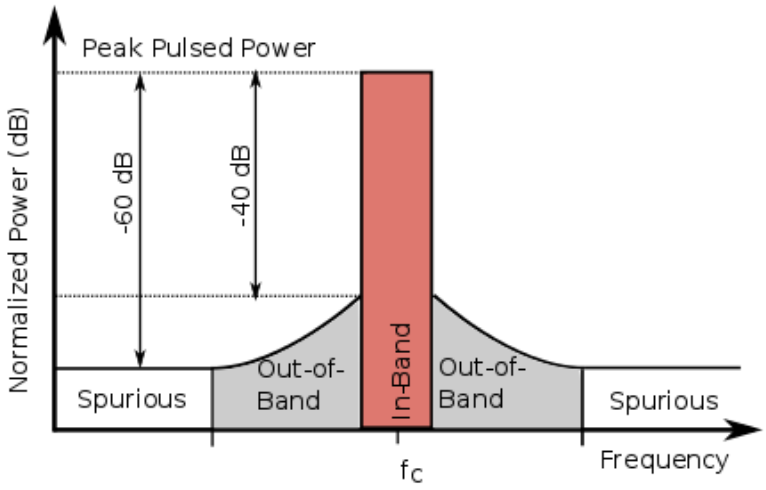

Figure 2.1: Figure from the NTIA report [30] demonstrating RSEC for a class of pulsed radar. The in-band and out-of-band bandwidths depend on characteristics such as pulse width and time-bandwidth product. The regulation on spurious emissions is -60 dB relative to peak power for this figure, but they can be as severe as -80 dB.

amplifier efficiency [1]; Filtering has also been shown to improve radar spectral compliance [31], but these filters must be able to handle the high power from radar transmitters. Additionally, filters have in-band losses which decrease the effectiveness of the transmitter. Although previous techniques have been sufficient to limit spectrum within existing regulations, there is pressure to further improve the spectral properties of radars.

The need for more bandwidth of wireless systems is beginning to impose more stringent requirements on radars, and some are calling the need for more spectrum a crisis [32][33]. If radars are going to operate in a more congested communications environment, they need to start behaving like communications transmitters. Recently, there has been increased activity in how to improve the spectral properties of radars while maintaining the efficiency. Work has been done to optimize the load of the PA, with load pull, for maximum efficiency while complying to a given ACPR [33]. Work has also been done to apply weighting functions to waveforms to ensure they have contained spectra [34].

This chapter motivates the use of the Gaussian pulse for spectral purposes. It compares the Gaussian pulse to the traditional rectangular pulse in terms of total pulse energy, range resolu-

tion, and spectral properties. Methods of improving the total energy and range resolution of the Gaussian are presented. We show that these modifications to the Gaussian pulse allow for the same performance as the rectangular pulse while vastly improving upon the spectral properties, a necessary step in operating radars in a congested environment.

2.1 Waveform Definitions

2.1.1 Rectangular Pulse

The most basic envelope for a pulsed radar is the rectangular pulse, mathematically described by

$$R(t) = \begin{cases} A & |t| < \frac{T_p}{2} \\ 0 & \text{otherwise} \end{cases} \tag{2.1}$$

where T_p is the length of the pulse. The time domain representation is shown in Figure 2.2. The rectangular pulse maintains peak power throughout the pulse thus having the highest energy of a pulse of duration T_p; however, it has the major drawback of having sharp edges with a power spectrum vs. frequency shown in Figure 2.2.

2.1.2 Gaussian Pulse

To eliminate sharp edges, a pulse with a smooth transition from off-state to on-state is next considered. An infinite number of shapes can be thought of which fulfill this condition, but this work will focus on the Gaussian shape.

The Gaussian is most commonly known to describe the Normal probability distribution function and is defined in most statistics books as [35]

$$f_X(x) = \frac{1}{\sqrt{2\pi\sigma^2}} e^{\frac{-(x-\mu)^2}{2\sigma^2}} \tag{2.2}$$

where μ is the mean, σ is the standard deviation, X is a random variable, and the function is normalized so that the total integral is one. Since the Gaussian expands to infinity in both directions, it is not technically a pulse, so its definition must be modified as follows. Like the

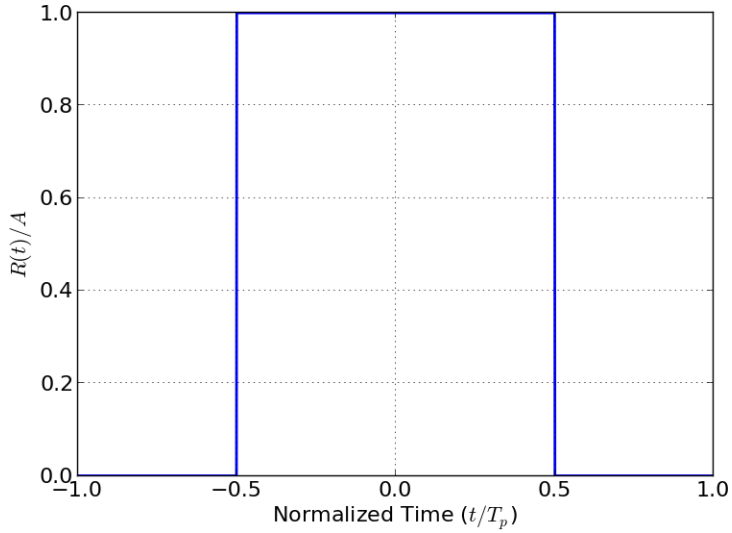

(a)

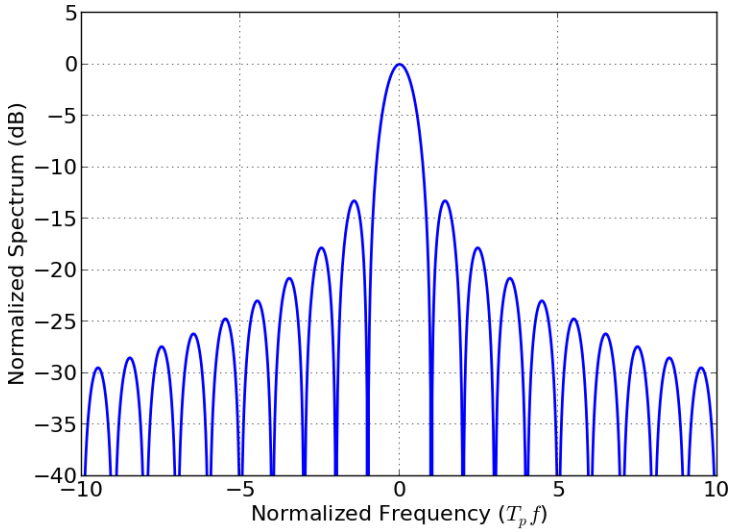

(b)

Figure 2.2: (a) The time domain representation of $R(t)$ which has a total pulse energy of AT_p. (b) Spectrum of $R(t)$ when normalized to the energy of the pulse. The sharp edges of the time domain signal cause infinite frequency content with significant side lobes.

rectangular pulse,we define it to be non-zero from $-\frac{T_p}{2}$ to $\frac{T_p}{2}$, will be centered around zero (i.e. $\mu = 0$), and is chosen to fit 4 standard deviations within the pulse. This definition contains 99.95% of the total energy of (2.2) and almost equals zero at the edges of the pulse. The selection of

4 standard deviations is somewhat arbitrary and other widths can be considered as well. The equation for this pulse is

$$G(t) = \begin{cases} Ae^{\frac{-(32t/T_p)^2}{32}} & |t| < \frac{T_p}{2} \\ 0 & \text{otherwise} \end{cases} \tag{2.3}$$

where A is a scaler for the signal power. The time domain signal and power spectrum of the Gaussian pulse are shown in Figure 2.3. Notice that the pulse contains less energy when defined in this fashion, but has a much more confined spectrum.

2.1.3 Linear Frequency Modulation

Whereas $R(t)$ and $G(t)$ defined the amplitude of the radar waveform, the phase of the waveform is also modulated. The phase modulation used in this work is linear frequency modulation, also known as a linear chirp, which sweeps the immediate frequency from below to above the center frequency [29]. The frequency can also be swept down, but an up-chirp is used for this research. The center frequency is zero, in the case of baseband, but shifts to the carrier frequency when up-converted. The definition of this waveform is

$$C(t) = A(t)e^{\frac{j\pi\beta t^2}{T_p}}. \tag{2.4}$$

The chirp is defined from negative to positive infinity and relies on $A(t)$ to bind its energy. For this work, $A(t)$ will either be $R(t)$ or $G(t)$, and β is the bandwidth swept (Hz) within T_p. It will be the convention of this work to fully define the waveform as either $R_{\beta T_p}(t)$ or $G_{\beta T_p}(t)$ where the name specifies the envelope and βT_p defines the time-bandwidth product. An example of $R_{\beta T_p}(t)$ is shown in Figure 2.4 for $\beta T_p = 10$

$$R_{10}(t) = R(t)e^{\frac{j\pi 10t^2}{T_p^2}} \tag{2.5}$$

and $\beta T_p = 50$

$$R_{50}(t) = R(t)e^{\frac{j\pi 50t^2}{T_p^2}} \tag{2.6}$$

.

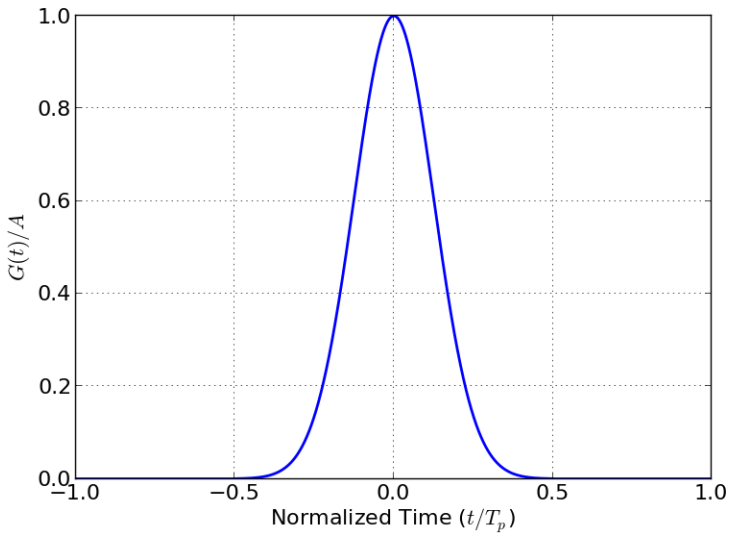

(a)

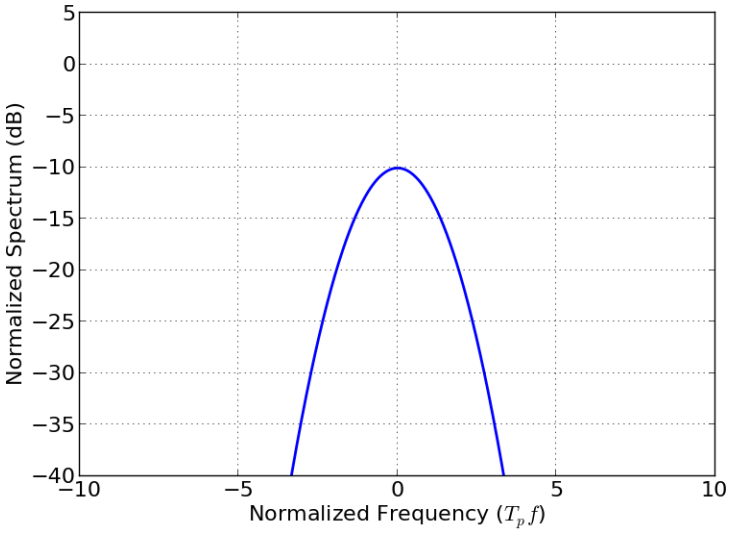

(b)

Figure 2.3: (a) The time domain representation of $G(t)$. (b) Spectrum of $G(t)$ when normalized to the total energy of $R(t)$ with the same T_p and peak power. Notice that the pulse contains less energy when defined in this fashion, but has a cleaner spectrum.

2.2 Modifying the Gaussian to Match Rectangular Performance

2.2.1 Improving Gaussian Total Energy

When considering the design of radar signals, there are numerous metrics that need to be addressed. Among theses are R_{max} and range resolution, which determine radar performance,

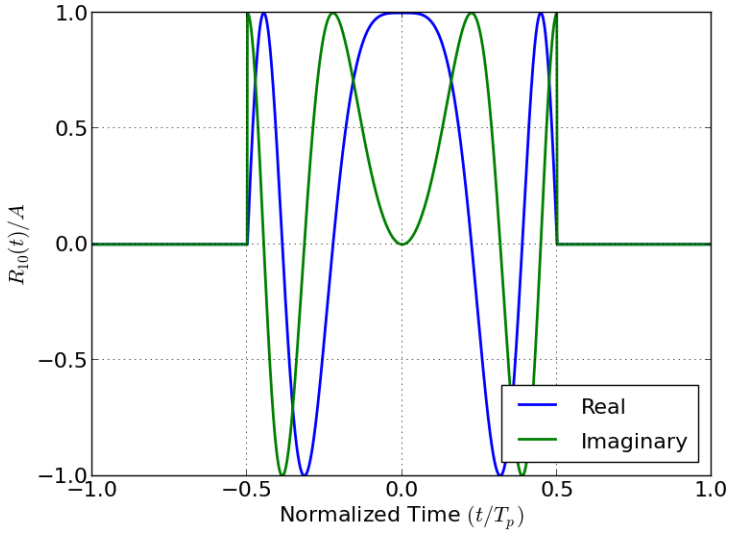

(a)

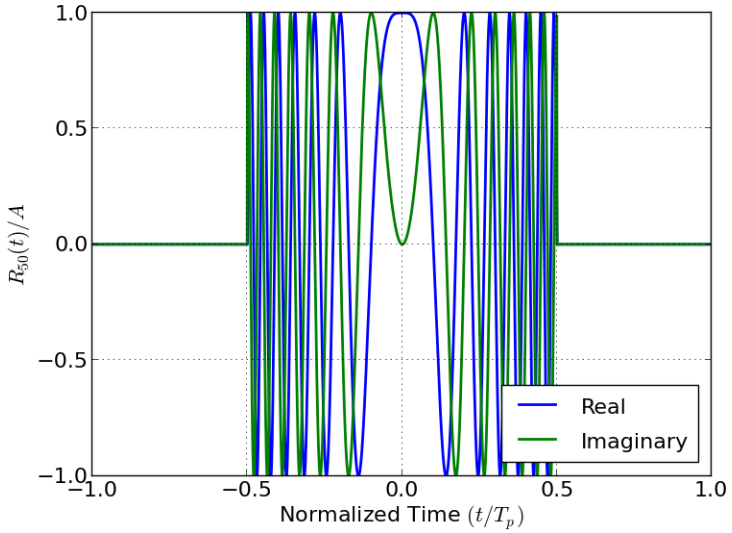

(b)

Figure 2.4: Real and imaginary waveforms for (a)$R_{10}(t)$ and (b)$R_{50}(t)$.

and the spectral properties of the waveform, determining how out-of-band systems are affected. Additionally, the different waveforms have unique characteristics within the power amplifier which impact system efficiency and spectral properties. This section addresses these metrics for the waveforms considered in this thesis.

R_{max} in (1.33) is expressed for a given P_t and B. Although it was not explicitly stated, the mathematics imply a constant P_t of a rectangular pulse. Since the analysis is for pulsed radar, the bandwidth is approximated as $B = 1/T_p$. Since (1.33) is for a rectangular pulse, it must be modified for determining the maximum range or a Gaussian pulse.

The total energy of a Gaussian pulse is

$$\int_{-Tp/2}^{Tp/2} \left[Ae^{\frac{-(32t/T_p)^2}{32}} \right]^2 dt \approx 0.221 A^2 T_P, \tag{2.7}$$

a substantial reduction from the energy of a rectangular pulse for the same peak power. To adjust for this, the pulse width of (2.3) needs to be scaled so that it contains the same energy; otherwise, it would be an unfair comparison of the pulses. This can be done by either increasing the transmitter power or by widening the pulse. It is assumed that the same transmitter is used to transmit $R(t)$ and $G(t)$, so the pulse is widened with the time scaling transformation and solving for the variable which provides the same energy as $R(t)$. Solving for the variable, a, is done with the equation

$$\int_{-\infty}^{\infty} G\left(\frac{t}{a}\right)^2 dt = A^2 T_p \tag{2.8}$$

and numerical techniques; the solution is $a = 4.51$. The Gaussian pulse is now redefined as

$$G(t) = \begin{cases} Ae^{\frac{-(32t/4.51T_p)^2}{32}} & |t| < 4.51\frac{T_p}{2} \\ 0 & \text{otherwise} \end{cases} \tag{2.9}$$

This new definition of $G(t)$ will be used from now on in place of (2.3) when referring to a Gaussian pulse unless otherwise stated. A comparison of the original $R(t)$ and the longer $G(t)$ is shown in Figure 2.5. It is obvious from the figure that the Gaussian pulse has much more desirable spectral properties when it contains the same amount of energy as the rectangular pulse. Another thing to note about the shorter Gaussian pulse in (2.3) is its wider spectrum. If the time scaling were not performed, the receiver bandwidth of $1/T_p$ would be too narrow for this pulse and even less energy would received. However, the wider Gaussian pulse fits inside the $1/T_p$ bandwidth until the spectrum in more than 50 dB below the peak, although only the spectrum is only plotted to -40 dB in Figure 2.5 (b). One complication that emerges when using the longer Gaussian pulse is that

the minimum range of the radar increases because the transmitter must stay on longer, forcing the receiver to remain off.

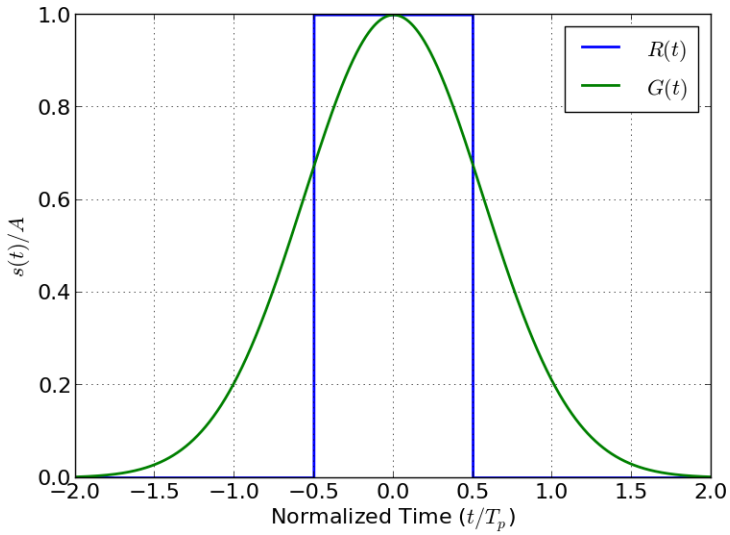

(a)

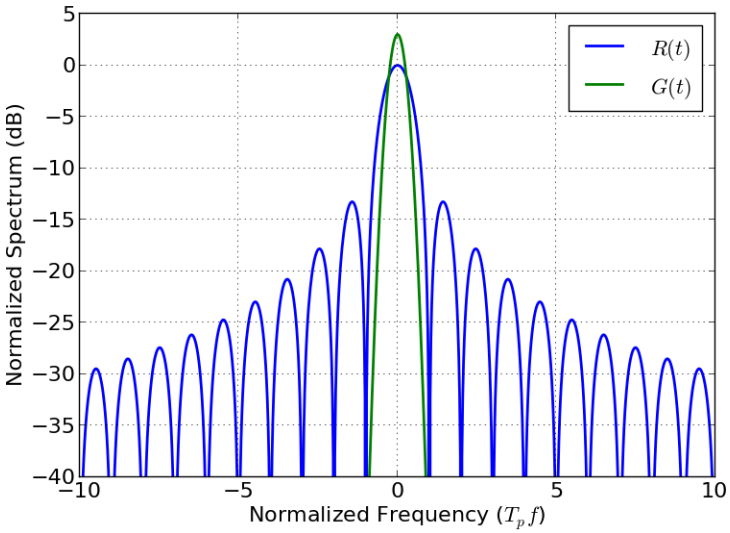

(b)

Figure 2.5: (a) Comparison of $R(t)$ and the time-scaled $G(t)$ in the time domain. In this case, the energy under the pulses is the same. (b) Comparison of the spectra of $R(t)$ and $G(t)$. The Gaussian pulse has a much cleaner spectrum and fits inside the bandwidth of $1/T_p$.

This is a simplified analysis of how Gaussian pulses perform relative to rectangular which

focused on the total energy in a pulse and the noise power in an assumed bandwidth. A more detailed analysis would require one to consider the desired probabilities of detection and false alarm and then how the matched filter impacts these for each shape [28][2]. The next section discusses the matched filter, but only how it impacts the range resolution and not the PDF of the noise only and signal-plus-noise hypotheses.

2.2.2 Improving Gaussian Range Resolution

Figure 2.6 shows the range resolution for both a rectangular pulse, and the time-scaled Gaussian. It is clear from the figure that the Gaussian has degraded resolution[1] .

As with the rectangular pulse, the resolution of the Gaussian pulse is proportional to its pulse width. The resolution could be improved by shortening the pulse, but this returns to the problem of less energy on target. Another method of improving the resolution is by increasing the bandwidth of the pulse, such as with a chirp. The logical question to ask is how much bandwidth needs to be added, or what is the value of βT_p, to allow $G_{\beta T_p}(t)$ to match the range resolution of $R(t)$ for a given T_p. Computer simulation shows $\beta T_p = 0.8$ allows for a chirped Gaussian pulse

$$G_{0.8}(t) = \begin{cases} Ae^{\frac{(32t/4.51T_p)^2}{32}} e^{\frac{j\pi 0.8t^2}{T_p^2}} & |t| < 4.51\frac{T_p}{2} \\ 0 & \text{otherwise} \end{cases} \tag{2.10}$$

to match the range resolution of an unmodulated rectangular pulse. The matched filter response of $G_{0.8}(t)$ is shown in Figure 2.7 and the pulse is shown in Figure 2.8.

The rectangular pulse can also add phase modulation to improve range resolution. For a given T_p, the resolution improvement is proportional to βT_p. This is demonstrated in Figure 2.9 where the range resolution is improved ten-fold with $R_{10}(t)$. Although $R_{10}(t)$ has improved range resolution, it generates unwanted artifacts known as time side lobes. They can be problematic because a strong reflector can generate side lobes that mask a smaller target. Even worse, a decoy can use an attack known as a range-gate pull-off [36] to confuse the radar and cause it to lose the track on the true target hidden in a time side lobe.

[1] In range resolution plots, the time scale can be converted to meters by multiplying the scaler by $T_p c/2$.

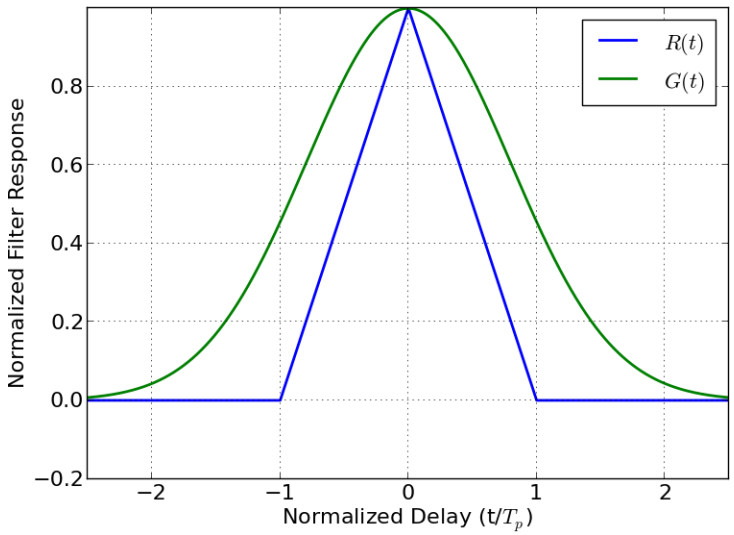

(a)

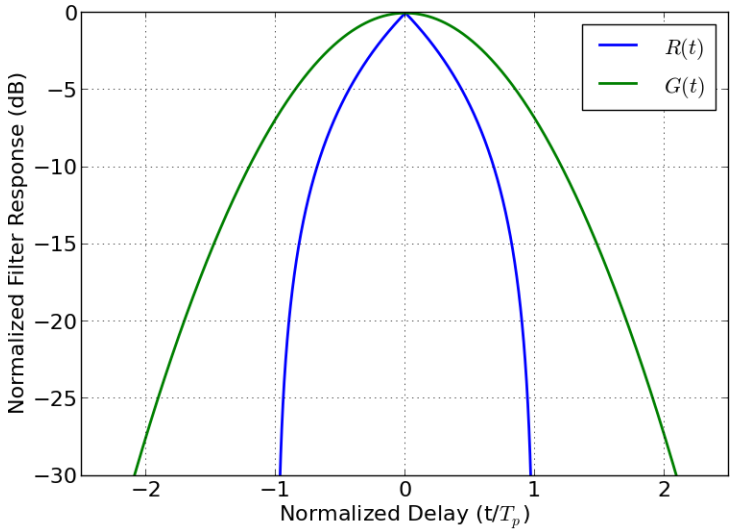

(b)

Figure 2.6: The range resolution of a rectangular pulse is $cT_p/2$. The time-scaled Gaussian pulse has a degraded range resolution for the same T_p.

Time side lobes can be mitigated by applying a window in the pulse compression [29]. Although windowing decreases time side lobes in the receiver, the transmitter is still sending a rectangular pulse and nothing is done to address the transmitted spectrum. Additionally, windowing

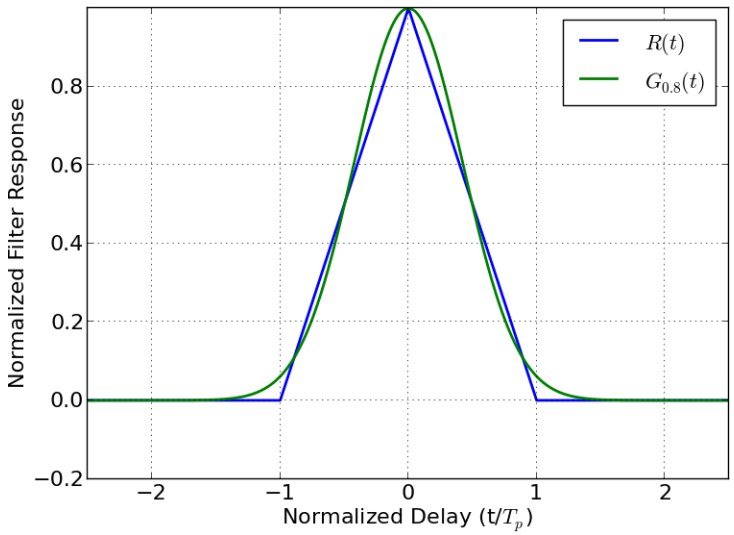

(a)

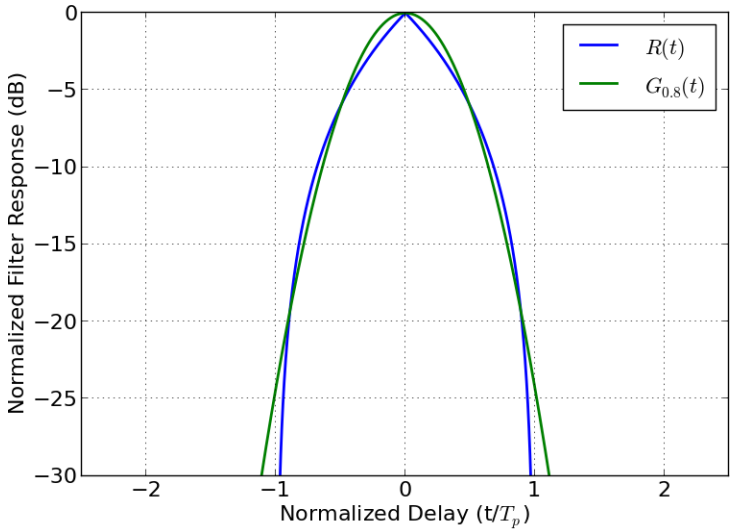

(b)

Figure 2.7: An unmodulated rectangular pulse and Gaussian chirp with bandwidth of $\beta T_p = 0.8$ have the same range resolution.

widens the pulse-compressed response and decreases the signal energy. Windows are typically applied to the matched filter in the frequency domain with element-wise vector multiplication. Figure 2.10 shows the spectrum for $R_{50}(t)$ with a Hamming window[2] . The definition for a Hamming

[2] Many types of windows exist, such as Hanning, Hamming, Chebyshev and Taylor windows.

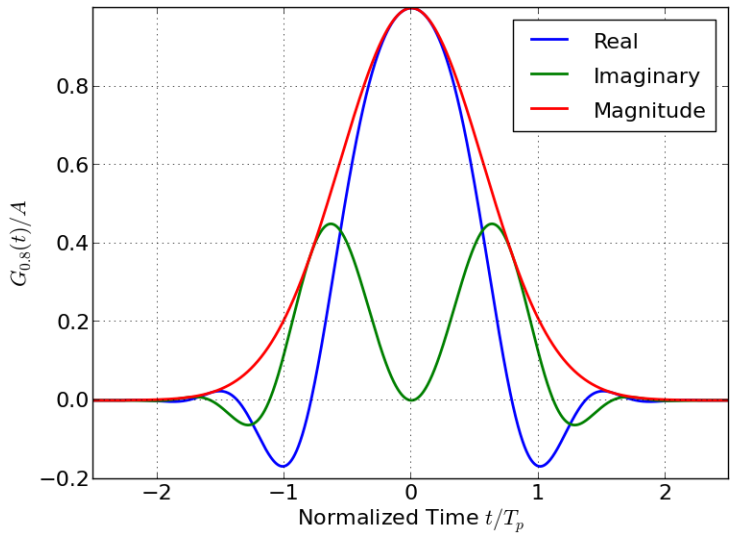

Figure 2.8: In-phase, quadrature, and magnitude of $G_{\beta T_p}(t)$ for $\beta T_p = 0.8$.

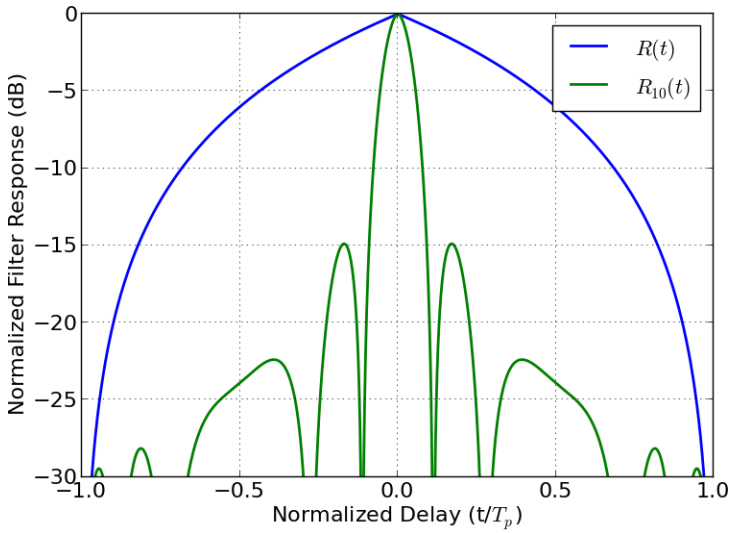

Figure 2.9: The rectangular pulse demonstrates an improvement in range resolution proportional to the bandwidth of the chirp modulated inside. The downside to this technique is the generation of time side lobes.

window is

$$w[n] = a - b\cos\left(\frac{2\pi n}{N}\right) \tag{2.11}$$

where $a = .54$, $b = 1 - a = .46$, N is the number of samples and the edges of the window align with half-magnitude points of the normalized spectrum. The pulse-compressed response of $R_{50}(t)$ is shown in Figure 2.11 without and with the Hamming window applied. The window decreases the time side lobe from -13 dB to -48 dB, but the main lobe is widened and the peak signal level decreases by 5.5 dB. An estimate of how badly signal-to-noise ratio is degraded is given by the processing loss (PL) and can be calculated for any widow with

$$\mathrm{PL} \approx \frac{|\Sigma_{\mathrm{n}=0}^{\mathrm{N}-1}\mathrm{w[n]}|^2}{\mathrm{N}\,\Sigma_{\mathrm{n}=0}^{\mathrm{N}-1}|\mathrm{w[n]}|^2}, \tag{2.12}$$

which is PL ≈ -1.3 dB for a Hamming window, .

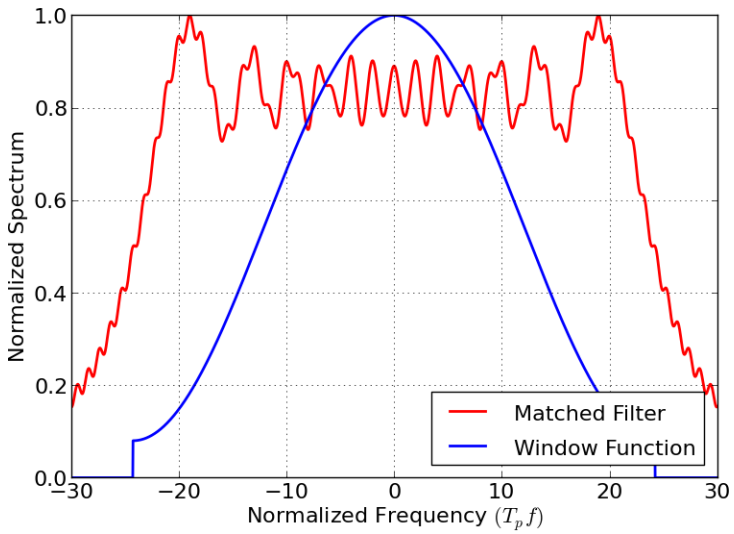

Figure 2.10: The spectrum of the matched filter of $R_{50}(t)$ and the Hamming window applied to it. It is applied with element-wise vector multiplication in the frequency domain. The edges of the window are aligned with the half-magnitude points of the matched-filter spectrum.

At this point one should be wondering how much bandwidth is needed for a given range resolution for both $R_{\beta T_p}(t)$ and $G_{\beta T_p}(t)$. It was just shown that a ten-fold improvement can be achieved with a rectangular chirp with $\beta T_p = 10$; computer simulations show the same can be achieved with a Gaussian chirp for $\beta T_p = 7.6$. The matched filter output of these two pulses is shown in Figure 2.12 which shows the same range resolution, but the Gaussian does not have time

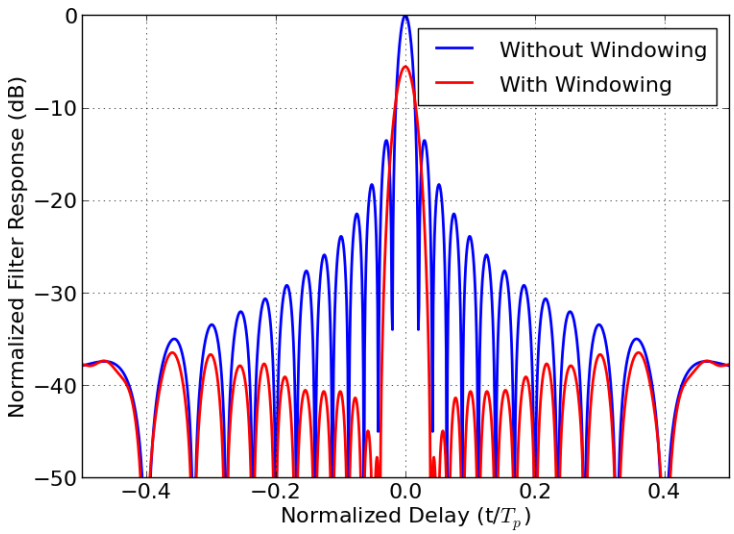

Figure 2.11: The Hamming window decreases the first time side lobe of the pulse-compressed response from -13 to -48 dB, but broadens the main lobe and decreases peak signal level by 5.5 dB.

side lobes. It should be noted that even though there are no time side lobes, the Gaussian chirp does still have energy where the rectangular time side lobes exist. Although it is not visible in Figure 2.12, the Gaussian chirp has energy -45 dB below the peak at the location of the rectangular time side lobe. Figure 2.13 shows the βT_p required for a sweep of range resolution values for both envelopes. For values of $\beta T_p > 5$, the ratio of the range resolution for the rectangular to Gaussian envelopes is about $1.3 : 1$.

2.2.3 Spectrum

To conclude the comparison of the Gaussian to rectangular envelope, the spectra must be compared. For a fair comparison, the spectrum of a modulated and time scaled Gaussian is compared to a rectangular pulse of width T_p as shown in Figure 2.14. The Gaussian pulse is that of (2.10) so that the energy on target and range resolution match the rectangular pulse. This figure shows (2.10) achieves similar performance to a rectangular pulse while vastly improving the spectral characteristics. Side lobes are entirely eliminated and the main-lobe is only slightly widened. When

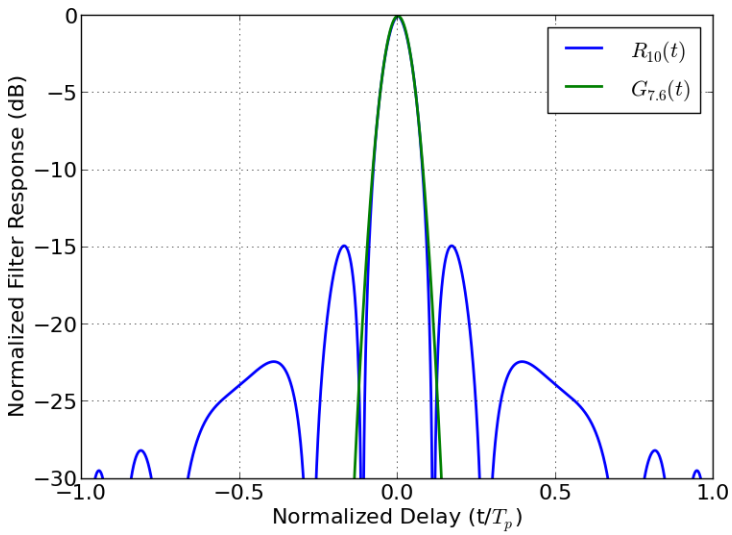

Figure 2.12: Range resolution for both $R_{10}(t)$ and $G_{7.6}(t)$. Both achieve a ten-fold improvement over $R(t)$ with the same T_p, but the Gaussian chirp does not have the time side lobes.

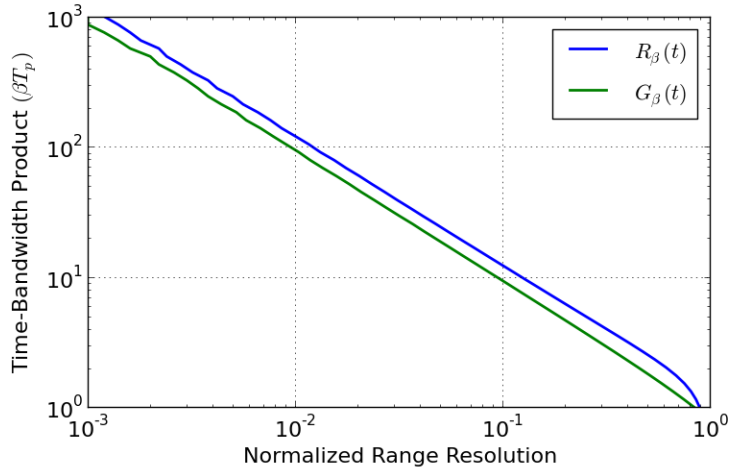

Figure 2.13: Time-bandwidth needed for the rectangular and Gaussian chirps to improve the range resolution of un-modulated rectangular pulse. A normalized range resolution of 10^{-1} corresponds to a tenfold improvement over the $R(t)$. The Gaussian always has a better range resolution for a given βT_p and the ratio of rectangular to Gaussian resolution is about $1.3:1$.

the spectrum of $G_{\beta T_p}(t)$ is compared to that of $G(t)$, one notices the peak power is decreased. That is because both are normalized to the energy in a rectangular of duration T_p and $G_{\beta T_p}(t)$ has more

high frequency content due to the frequency modulation.

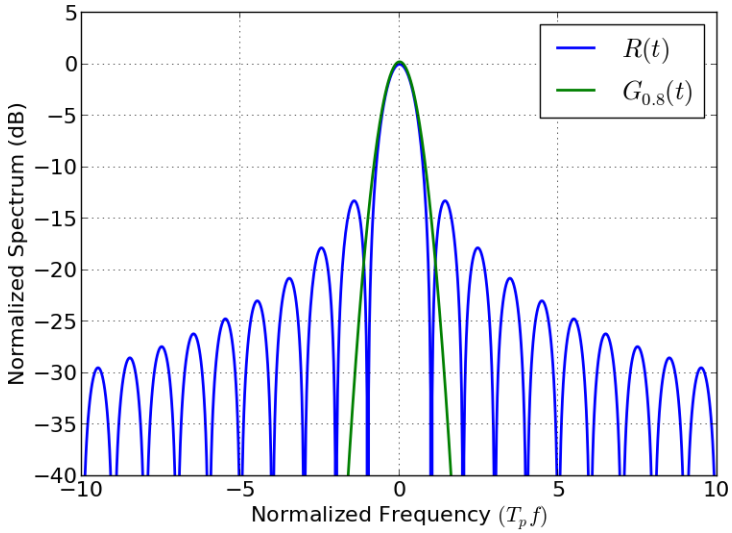

Figure 2.14: A comparison of the spectra of $R(t)$ and $G_{\beta T_p}(t)$ when the Gaussian has the same range resolution and energy as the unmodulated rectangular pulse. Both are normalized to the energy of the rectangular pulse. The Gaussian pulse shows great improvement in spectral properties.

Since pulse-compression radars are now ubiquitous, it is necessary to compare the spectra of chirped rectangular and Gaussian pulses. Again, the Gaussian is modulated and time scaled so that it provides the same range resolution and energy as the rectangular chirp. In this case, both pulses have a range resolution ten times better than an unmodulated rectangular pulse of duration T_p. Figure 2.15 shows the spectrum of a rectangular pulse of duration $T_p/10$ and amplitude $10A$, which has the same range resolution and energy as the first two pulses. Again, the Gaussian pulse demonstrates superior spectral characteristics.

2.3 Classes of Amplifiers

An important aspect of a power amplifier is its class of operation which describes how the power amplifier is biased. The quiescent current is the drain current of the PA when in small-signal operation, which is controlled by the gate bias voltage and drain voltage (for a field-effect transistor). Class-A operation is when the quiescent current is half of the maximum current of the

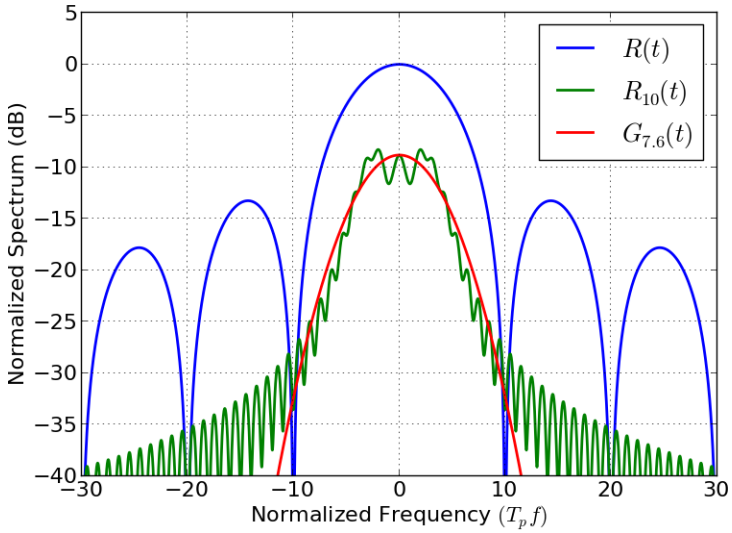

Figure 2.15: Spectra of $R(t)$ with ten times shorter width and higher amplitude, $R_{\beta T_p}(t)$, and $G_{\beta T_p}(t)$. All provide a ten-fold improvement in range resolution over unit width and amplitude $R(t)$ while maintaining the same energy.

transistor and the DC drain voltage is half the breakdown voltage. Drain waveforms for Class-A operation are shown in Figure 2.16. By biasing the transistor in this way, the current and voltage waveforms have the room to swing from their maximum and minimum values when operating at peak un-compressed power. However, the average current and voltage remain the same as power is backed-off, resulting in constant DC power even for small signal levels and thus poor efficiency.

Class-B operation is when the quiescent current is chosen to be 0 A, but the drain voltage remains half the breakdown voltage as shown if Figure 2.17. At peak power, the current swings to the maximum value during half a cycle, and is cut off for the other half cycle. Although the waveform appears distorted, it is only the fundamental component of this waveform which makes it to the RF load. For Class-B, the fundamental component is the same as Class-A but requires a higher input power. The benefit of Class B is that as the power is decreased, the average current also decreases, thus improving backed-off efficiency. Class-AB is when the PA has a quiescent current greater than zero, but less than the Class-A quiescent current; Class C is when the PA is biased below Class B.

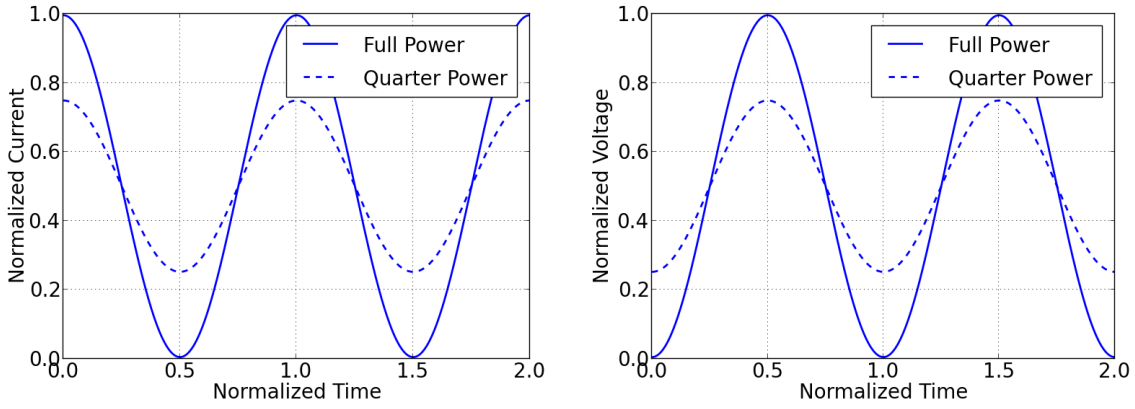

(a) (b)

Figure 2.16: (a) Drain current and (b) drain voltage of an ideal Class-A PA. Notice that as power is backed off, it continues to consume the same amount of DC power.

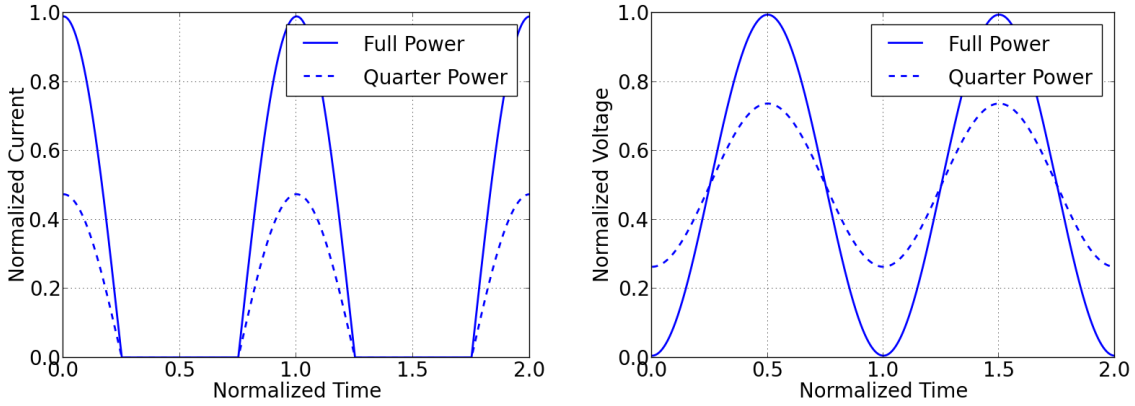

(a) (b)

Figure 2.17: (a) Drain current and (b) drain voltage of an ideal Class-B PA. As the output power is decreased, so does the average current and thus DC power consumption.

2.4 Efficiency of Supply Modulation

The advantages for using a Gaussian chirp were shown in the last section. Although these pulses certainly have their benefits, a major impediment to their implementation in real-world systems is the power amplifier efficiency. This section will show the theoretical efficiencies for two classes of amplifiers for variable amplitude signals, and how they may be improved.

Typical radar power amplifiers are biased in Class C for two reasons: (1) it is a very efficient mode of operation and (2) it is a self biasing topology [1]. That is to say, the amplifier draws no current when no pulse is present. When a pulse is present, it turns on the amplifier. Biasing below the transistor pinch-off voltage, as is done with Class C, works well for rectangular pulses but not amplitude modulated pulses. To understand this point, consider Figure 2.18 which shows the normalized output of an amplifier as it is biased progressively deeper into cutoff. As the bias voltage goes deeper into cut-off, the tails of the Gaussian become sharper. This shows why a Class C amplifier is not conducive to Gaussian pulses.

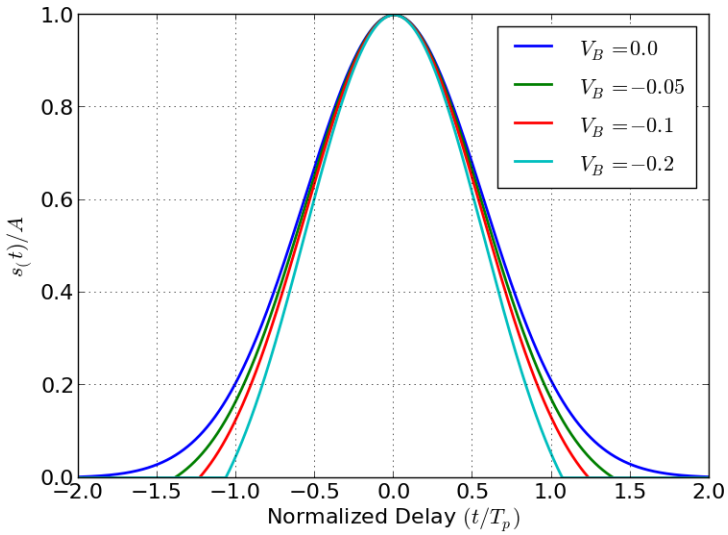

Figure 2.18: Shape of the output Gaussian pulse from a Class C amplifier. The Gaussian shape is perfectly maintained when $V_B = 0$, where V_B is normalize to the bias voltage that would provide I_{max} of the device (i.e. $V_B = 0.5$ for Class A). As the bias voltage is more negative, the tails of the Gaussian become sharper.

To demonstrate the impact of amplifier class on efficiency, consider the definition of drain efficiency

$$\eta = \frac{P_L}{P_{DC}} = \frac{{I_1}^2 R_L}{2 V_{DD} I_0} \tag{2.13}$$

where I_1 is the magnitude of the current at the fundamental frequency, R_L is the load resistance and is set to the Class-A and Class-B optimal value of V_{max}/I_{max}, V_{DD} is the drain bias voltage,

I_0 is the average drain current. A Class-A amplifier is biased such that the quiescent drain current and voltage are $I_{DC} = I_{max}/2$ and $V_{DC} = V_{max}/2$ respectively. The efficiency for any envelope level, A, can be found by substituting the average current

$$I_0 = \frac{1}{T}\int_0^T \left[A \sin\left(\frac{2\pi t}{T}\right) + \frac{I_{max}}{2} \right] dt = \frac{I_{max}}{2} \tag{2.14}$$

and the fundamental Fourier component

$$I_1 = \frac{2}{T}\int_0^T \left[A \sin\left(\frac{2\pi t}{T}\right) \sin\left(\frac{2\pi t}{T}\right) \right] dt = A \tag{2.15}$$

into (2.13), where T is the RF period. The result is

$$\eta_{ClassA} = \frac{2A^2}{{I_{max}}^2}; \quad \text{for } 0 \leq A \leq \frac{I_{max}}{2}. \tag{2.16}$$

The same procedure can be followed for Class B to obtain

$$I_0 = \frac{1}{T}\int_0^{\frac{T}{2}} A \sin\left(\frac{2\pi t}{T}\right) dt = \frac{A}{\pi}, \tag{2.17}$$

$$I_1 = \frac{2}{T}\int_0^{\frac{T}{2}} \left[A \sin\left(\frac{2\pi t}{T}\right) \sin\left(\frac{2\pi t}{T}\right) \right] dt = \frac{A}{2} \tag{2.18}$$

and

$$\eta_{ClassB} = \frac{A\pi}{4I_{max}}; \quad \text{for } 0 \leq A \leq I_{max}. \tag{2.19}$$

These results show that Class-A amplifier efficiency decreases quadratically with decreased amplitude while the Class-B efficiency only decreases linearly. Both of these classes have their DC voltage biased for the worst case scenario for required output power. If both classes of PAs had an adjustable voltage bias such that only the necessary amount was present to allow for full voltage swing at that power level, and no more, then there would be a savings in consumed DC power and thus an improvement in efficiency. This adjustable supply voltage can be expressed as

$$V_{DD} = I_1 R_L \tag{2.20}$$

and substituted into (2.13) to show

$$\eta_{ClassA-SM} = \frac{A}{I_{max}}; \quad \text{for } 0 \leq A \leq \frac{I_{max}}{2} \tag{2.21}$$

$$\eta_{ClassB-SM} = \frac{\pi}{4}; \quad \text{for } 0 \leq A \leq I_{max} \tag{2.22}$$

where SM denotes supply modulation. The Class-A amplifier is improved by supply modulation in that its efficiency decreases linearly with amplitude, but the maximum remains at 50%. As for the Class-B, the efficiency always remains at its peak of 78%; however, this does not include the impact of the knee voltage of the transistor. When the knee-voltage, V_k, is taken into account, the efficiency becomes

$$\eta_{ClassB-SM} = \frac{\frac{V_{max}-V_k}{8}A}{\frac{V_{max}-V_k}{2\pi}A + \frac{V_k I_{max}}{\pi}}. \tag{2.23}$$

The efficiencies of these four modes of operation are shown as a function of signal amplitude in Figure 2.19. These efficiencies can be calculated over the duration of a Gaussian pulse and are

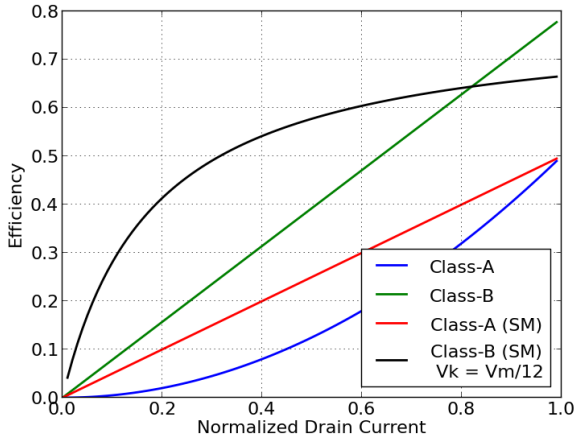

Figure 2.19: The efficiencies of different amplifier classes as a function of envelope level normalized to maximum drain current. Both static and dynamic bias conditions are shown.

shown in Figure 2.20. The average efficiencies of the PA are calculated in two ways in Table 2.1: the average instantaneous efficiency and pulse efficiency. The average instantaneous efficiency is the time-average of the curves in Fig. 2.20, which underestimates the efficiency for Class-B performance in low power regions. The pulse efficiency metric calculates the average output power over average DC power for the entire pulse. This shows improvement in the efficiency for the Class B cases, which do not use DC power when there in no output power. This analysis motivated our choice of

a Class-B MMIC PA used in the validation experiments in Section V.

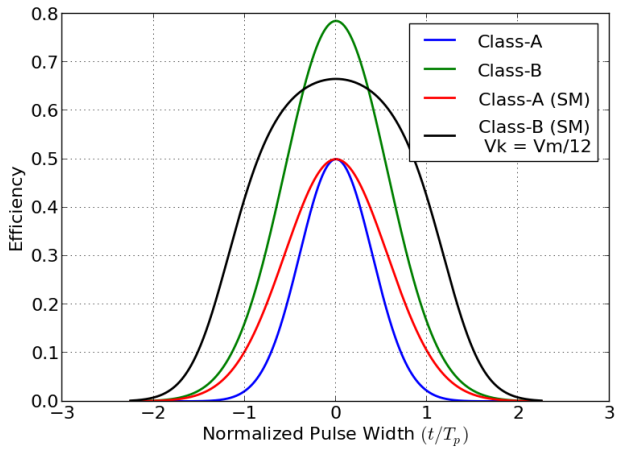

Figure 2.20: The efficiencies of different amplifier classes over the duration of a Gaussian pulse.

Table 2.1: Amplifier Efficiencies for a Gaussian Pulse

	Average Instantaneous Efficiency	Pulse Efficiency
Class-A	11.1%	11.1%
Class-B	24.6%	55.5%
Class-A (SM)	15.7%	15.7%
Class-B (SM)	33.1%	62.6%

Chapter 3

Supply-Modulated Transmitter Measurements and System-Level Simulations

3.1 Architecture of a Supply Modulated System

In this chapter, the implementation of a supply-modulated transmitter is presented. Although what follows is the implementation in a test bench and simulation environment, it is consistent with the necessary steps for the design of a fielded system, as discussed at the end of this chapter.

To understand the architecture of a supply-modulated system, consider the block diagram in Figure 3.1. The purpose of the system is to efficiently amplify the up-converted signal with minimal distortion and spectral regrowth. The signal is shown in baseband as $\tilde{s}[n]$, where the tilde represents that it is complex, and the brackets signify that it is in discrete time. The source of the signal can be many things depending on the application, such as a voice codec, digital modulator, or radar signal generator. This discussion will be agnostic to the source of $\tilde{s}[n]$, but it is assumed to be a baseband signal, usually given in in-phase (I) and quadrature (Q) format.

In the supply-modulated transmitter application, the signal is first represented in polar form and divided into an envelope and drive signal. The envelope signal, $\alpha[n]$ is determined by a trajectory optimized to some criterion, such as maximum efficiency or gain flatness. The trajectory maps the drain-voltage-based output power and is often a trade-off between the optimization criteria and what the supply modulator is able to efficiently supply [37]. Additionally, the drive signal, $\beta[n]$, can also be processed to adjust the amplitude, $A[n]$, and phase, $\theta[n]$, of the input signal. The signal split is the signal processing step which applies the trajectory to $\alpha[n]$ and any static compensation to $\beta[n]$ in either amplitude or phase. Two common types of supply modulation are are Envelope

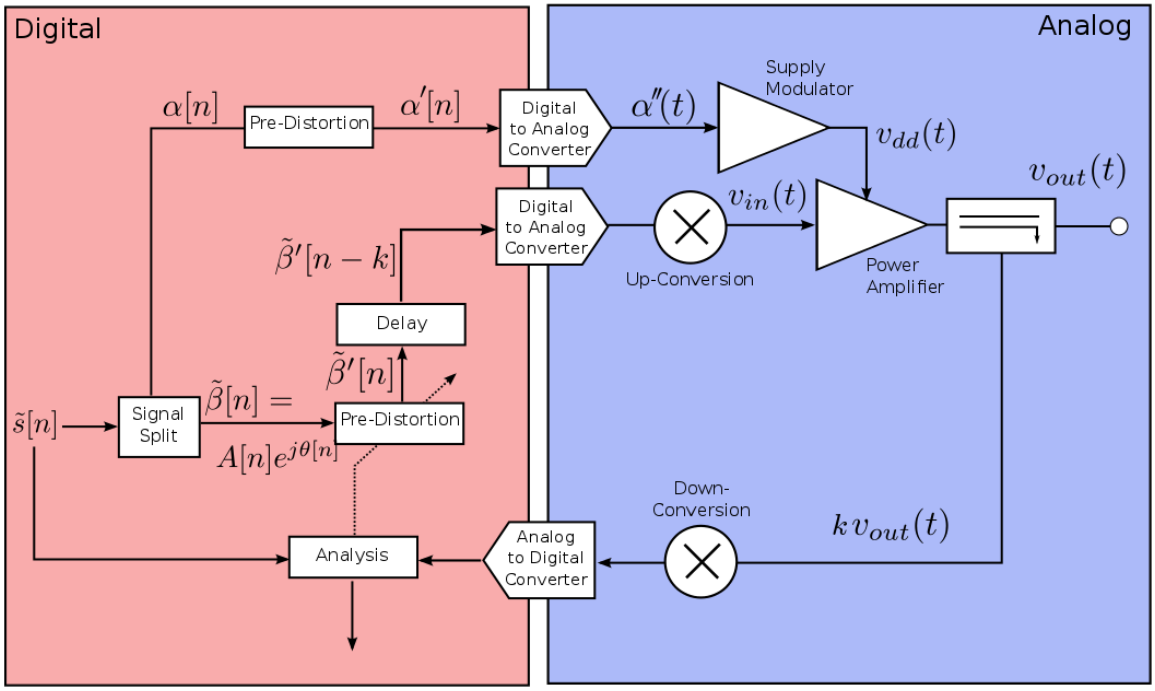

Figure 3.1: To amplify a signal, $\tilde{s}[n]$, with a supply-modulated system, it must be separated into drive and envelope paths based on a trajectory. The envelope path is converted to an analog signal and fed to the supply modulator. Pre-distortion can be used in the envelope path to correct any errors of the supply modulator. The drive signal is pre-distorted and delayed before it is converted to a microwave frequency analog signal. The output of the PA should ideally be a continuous version of $\tilde{s}[n]$ centered around the carrier frequency. This is verified by down-converting and digitizing the signal to compare to the original.

Tracking (ET) and Envelope Elimination and Restoration (EER). In ET, $\tilde{\beta}[n] = \tilde{s}[n]$ and the envelope signal is the lowest possible drain voltage which does not cause saturation of the amplifier at that particular power level [38]. In EER, the drive signal is limited to a constant amplitude, $\tilde{\beta}[n] = e^{j\theta}$, and $\alpha[n]$ is used to adjust the gain of the PA, thus controlling the shape of the amplitude. The selection of the trajectory is further discussed later in this chapter.

For the drive signal, the signal split is the point where a look-up-table can be applied to compensate for AM-AM and AM-PM effects. This is not to be confused with the Digital Pre-Distortion (DPD) block that comes next. If one chooses to use this block, it applies an adaptive algorithm based on a model of the PA, such as a memory polynomial [39]. It relies on feedback from the sampled output of the system and adapts weights to find an input to the PA which will

provide the desired output [40].

After DPD, the drive signal must be delayed so that it is time-aligned with the envelope signal at the virtual drain of the power amplifier. The time alignment step is discussed in Section 3.2.6. This step must be done on either the drive or envelope path, but experience shows that the envelope path is usually longer, so it is the drive path that is delayed.

At this point, both signals must be converted from the digital domain to the analog domain. For a fielded system, this would be done with digital-to-analog converter chips. On a test bench, it is done with arbitrary waveform generators that have $\alpha[n]$ and $\beta'[n]$ loaded into memory as waveform vectors. Additionally, the drive signal must be up-converted to RF once it is in the analog domain. On a test bench, this is accomplished with a signal generator that allows for amplitude and phase modulation via the AWG.

The signals are applied to the devices under test in this work: the power amplifier and supply modulator. In a fielded transmitter, the output of the PA would feed an antenna, usually matched to $50\,\Omega$. However, the main purpose of the bench is characterization, so the output is recorded by a 50-Ω signal analyzer instead. This step brings the signal back into the digital baseband domain for performance analysis and to provide information for training the weights of DPD.

3.2 Bench Design and Setup

3.2.1 Equipment

Figure 3.2 shows a diagram of the equipment used in the setup. Pieces not pertaining to signal generation or capture, such as power supplies and meters, are not shown. Two Agilent (Keysight) N8241A dual-channel Arbitrary Waveform Generators (AWG) are used: one for the envelope signal, $\alpha[n]$, and one for the baseband drive signal, $\beta[n]$. The envelope AWG only requires one channel since it is a real signal, whereas the complex drive signal requires both. The drive signal is modulated and up-converted using the Agilent E8267D PSG signal generator. Likewise, the signal is down-converted and sampled with an Agilent N9030A PXA signal analyzer. Before

the RF signal enters the PA, it is amplified by a driver and coupled to the PXA. The output is also captured by the PXA. An RF switch determines if the PA input or output are captured. A driver amplifier is used so that the input to the PA is sufficient to reach the desired output power while the attenuator protects the PXA. A photograph of the AWGs, PXA, and PSG are shown in Figure 3.3. All equipment is controlled and waveforms processed with Matlab or Python.

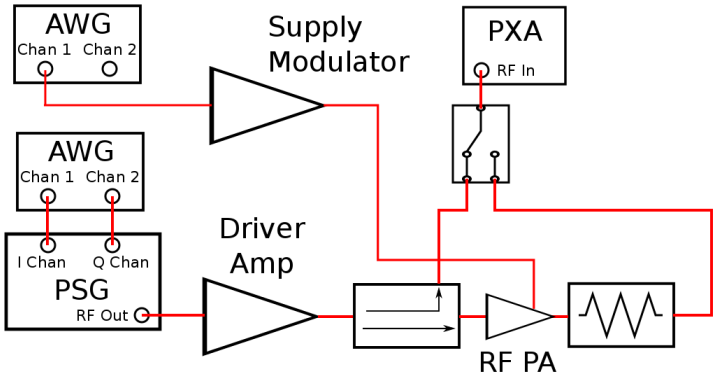

Figure 3.2: Configuration of the equipment in Figure 3.3. One channel of the envelope AWG feeds the supply modulator. Both channels of the drive AWG feed the signal generator, which is further amplified by a driver before entering the PA. The PA output signal is attenuated to protect the signal analyzer before reception.

There are two modulators used in the work reported in this chapter: a linear modulator [41] and a switching [42] modulator. The linear modulator is a series of cascaded op-amps with a final stage GaN High Electron Mobility Transistor (HEMT) source-follower. It is classified as linear because it satisfies (1.18), even though it uses non-linear transistors, as long as the output voltage does not exceed the supply voltage for any stage of the amplifier. This is the modulator used for the following sections discussing bench characterization and linear system theory.

The linear modulator is inefficient because it reduces power supplied to the PA at low bias conditions by dissipating it in the source-follower. Although it has the desired property of linearity, the inefficiency is undesirable, so a switching modulator is also used in bench measurements. The switching modulator modulates its output voltage using two transistors, one connected to the high-side supply and the other to the low-side ground. The duty cycle of the switching times controls

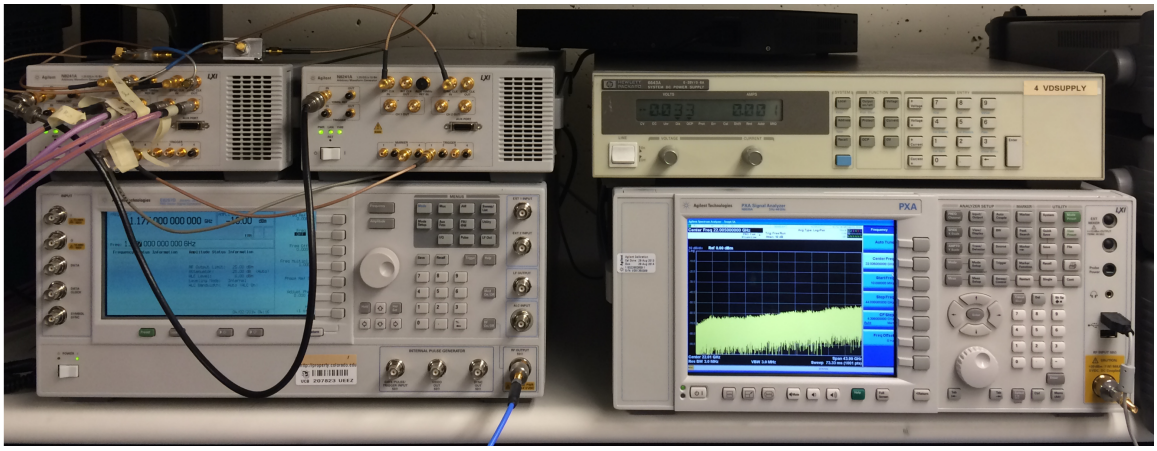

Figure 3.3: Photograph of the two N8241A Arbitrary Waveform Generators, E8267D PSG signal generator, and N9030A PXA signal analyzer used in the bench-top measurements. The driver is an HP 83020A microwave system power amplifier with ¿30 dB gain and ¿27dBm output power at 10 GHz.

the output voltage. The operation of the switching modulator will be further elaborated upon in a later section discussing supply-modulation simulations.

What follows are the steps necessary to implement a supply modulation bench. The equipment must be power-calibrated for accurate measurements. One must also have a sense of the drain voltages to expect when waveforms are loaded to the AWG. For instance, if a normalized sine wave is loaded into the AWG, then the peak and trough of the linear modulator can be found using linear system theory. The use of linear system theory is justified because the supply modulator is used as a linear component in that the output signal is linearly proportional to the offset input. Although the supply modulators use non-linear transistors, the linear relationship between input and output allows us to use linear system theory to characterize the modulator path.

Of critical importance is how the modulator behaves when attached to the PA because it is necessary to know of any resonances, which cause instability. Resonances of sufficient power levels will exceed V_{max} of the transistor in the modulator and/or PA and destroy the device. The designer's job is to ensure that any resonant frequencies of the supply modulator connected to the PA are much higher than the envelope bandwidth. Of equal importance is to make sure the drain

and RF signals are aligned at the virtual drain of the PA so that there is no signal distortion or loss of efficiency. Lastly, the PA must be characterized appropriately in order to design an optimal trajectory.

3.2.2 Power Calibration

Both input and output waveforms are analyzed with a signal analyzer, which is typically not calibrated in terms of absolute power; however, it is necessary to know the true power at the input and output connectors. The process of calibrating the PXA is illustrated in Figure 3.4. The first step is to measure the true power at the input to the PA with a power sensor, and compare this to the power measured by the PXA. This allows for the measurement of PA input power with the PXA even though it is not at the reference plane.

The output power of the PA must be similarly calibrated. To do this, a "through" is connected in lieu of a PA so that the output is in the same reference plane as the embedded input. It would be impractical to interchange the output network and power sensor to perform this calibration. Instead, the calibrated input power measurement is used as the true power reference. To solve for the true power at the output, the switch at the input of the PXA is toggled to switch between input and output powers. In this fashion, the offset from true power for the output is determined.

3.2.3 Equipment Characterization

All the equipment previously mentioned is controlled using computer software via the VISA interface. Waveforms are created as a vector in software and uploaded to the AWGs. In order to effectively operate the bench, one needs to know the voltage that will be applied to the PA's drain for a given software waveform. Additionally, the AWG voltage must be known so that the modulator can be properly designed and controlled. Linear system theory is helpful in determining the "transfer function" from software to voltage waveform, which is described in the following sub-sections.

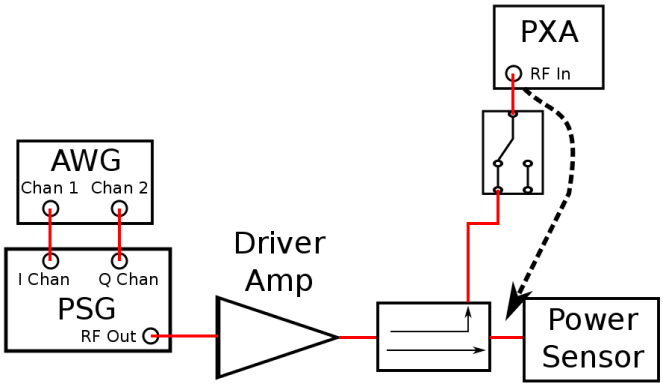

(a) Input power calibration

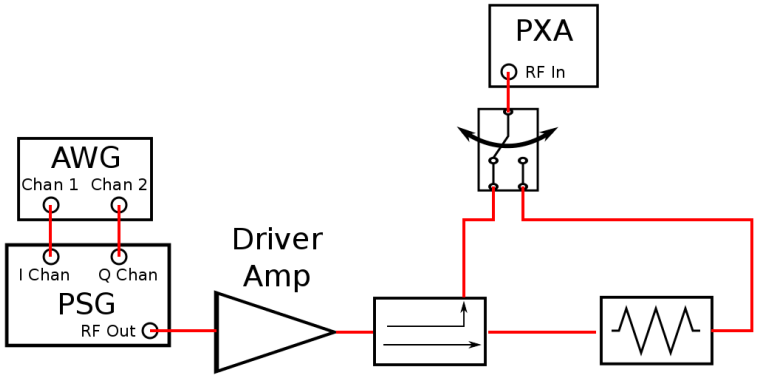

(b) Output power calibration

Figure 3.4: Shown here is the two-step calibration process for input and output power to the PA. (a) The offset from true input power is measured for the coupled input power at the PXA. (b) the input power measured by the PXA is used to measure the losses in the output network between the PA and PXA.

3.2.3.1 Linear System Characterization

Suppose a linear system can be modeled as

$$x\left[n\right] \rightarrow S \rightarrow y\left[n\right]$$

where $x[n]$ is the input signal, $y[n]$ is the output, and the system S maps $y[n]$ as

$$y[n] = mx[n] + b.$$

In this configuration the variables m and b can be understood to be the gain and the offset that the system imparts on a digital input signal. Solving for m and b is a linear regression problem

with the form of

$$\mathbf{y} = A\mathbf{c} + \mathbf{e} \tag{3.1}$$

where

$$\mathbf{y} = \begin{bmatrix} y[0] \\ y[1] \\ \vdots \\ y[N-1] \end{bmatrix}, A = \begin{bmatrix} x[0] & 1 \\ x[1] & 1 \\ \vdots & \vdots \\ x[N-1] & 1 \end{bmatrix}, \mathbf{c} = \begin{bmatrix} m \\ b \end{bmatrix}$$

and $\mathbf{e}$ is an error vector in the same form as $\mathbf{y}$. The goal of the linear regression problem is to find $\mathbf{c}$ which minimizes the sum of the squares of the error vector [43]. The solution to this problem is

$$\mathbf{c} = (A^T A)^{-1} A^T \mathbf{y}. \tag{3.2}$$

With the information in $\mathbf{c}$, the inverse problem of solving the software waveform for a particular voltage can be solved and used to characterize the linear supply modulator.

3.2.3.2 Arbitrary Waveform Generator

The output of the AWG is measured with an oscilloscope with the channel impedance set to 50 Ω. A triangular wave is input to the AWG with a normalized magnitude with the results shown in Fig. 3.5. One can see that there is no offset and that the voltage gain is about 0.25. Next, the same waveform is input but with a magnitude of 1.1. Values of less than -1 are clipped and values of greater than 1 wrap the voltage waveform to the negative clipping point. It is very important to always use normalized vector waveforms, otherwise non-linearity will be experienced in the AWG.

The gain of a frequency sweep from 10 kHz to 100 MHz gives the results shown in Fig. 3.6. After 1 MHz, the gain of the system begins to drop and decreases by almost 1.2 dB at 100 MHz. The manufacturers include a pre-distortion option to flatten the gain across frequency, but it comes at the expense of output voltage magnitude. Notice that there is a different scale on the y-axis for the pre-distorted mode which has a much lower output voltage. We chose not to use the manufacturer pre-distortion to avoid the decrease in output voltage and use our own algorithm.

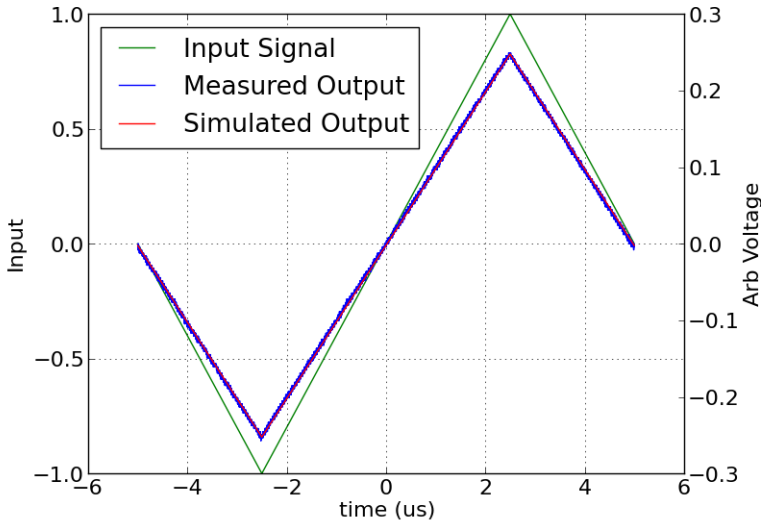

(a)

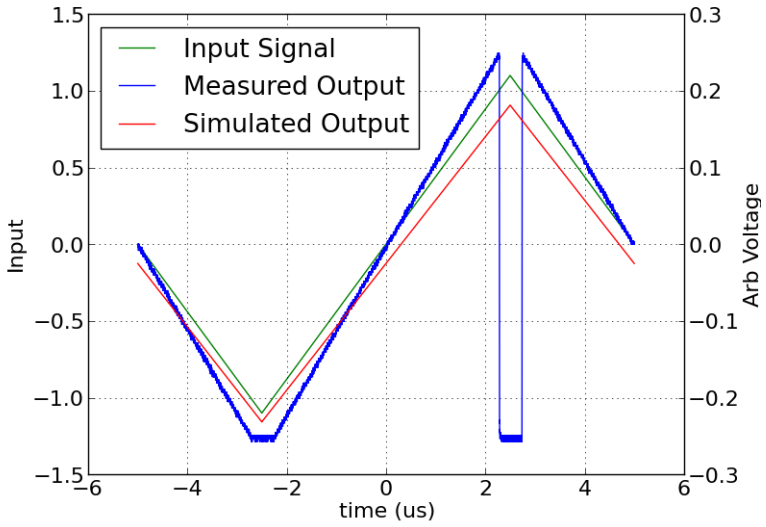

(b)

Figure 3.5: Figure depicting the linear characterization of AWG. The input (software) signal is shown in green and plotted on the left axis. The measured voltage from the AWG is plotted in blue along the right axis. Lastly, the predicted AWG voltage when the linear regression results are applied to the input signal are plotted in red along the right axis. The plot (a) shows good agreement between prediction and measurement; however, when the input amplitude exceeds 1.0 (b), the system becomes non-linear and the linear regression prediction is no longer valid.

3.2.4 Linear Modulator

To characterize the supply modulator it is assumed that the combination of the AWG and modulator is a linear system and that one can use linear regression to solve the gain and offset of

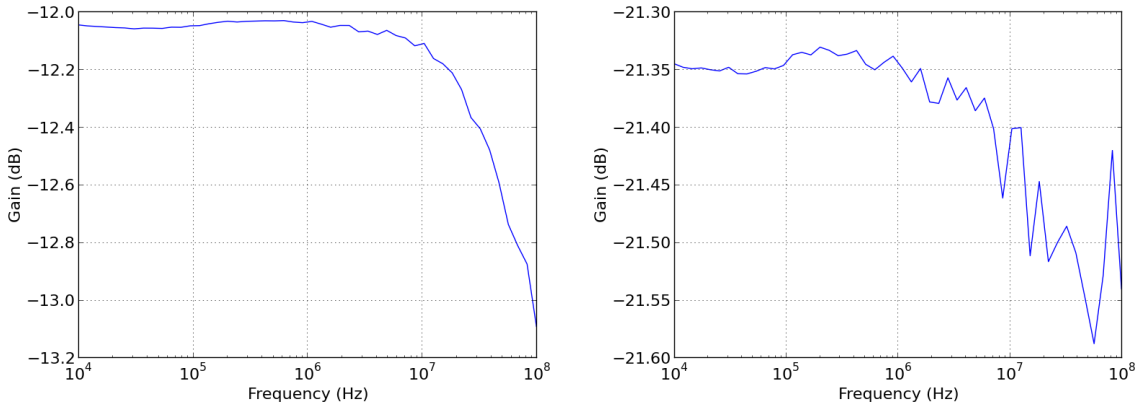

(a) (b)

Figure 3.6: Frequency response from the vector software waveform to AWG voltage when the manufacturer provided pre-distortion is disabled (a) and enabled (b). The manufacturer supplied pre-distortion has a much flatter frequency response, but comes at the expense of voltage magnitude.

the whole chain. However, for the m solved by linear regression to include the phase shift of the system, complex signals are needed. With this configuration, (3.2) is re-written as

$$\mathbf{c} = (A^H A)^{-1} A^H \mathbf{y} \tag{3.3}$$

where A^H is the conjugate transpose of matrix A. For (3.3) to result in the gain and phase, the measured signal needs to be complex. To synthetically create a complex signal from a real one, an imaginary component can be added by time shifting the real component by a quarter period. Fig. 3.7 shows the gain and phase as a function of frequency and shows there is a resonance at 57 MHz for the 75Ω load.

The modulator response to a Gaussian pulse further demonstrates the issues associated with the 57 MHz resonance. The purity of the output pulse depends on the length of the pulse, because the length of the pulse is directly related to the frequency content. The shorter the pulse, the more high frequency content it contains. The modulator becomes unstable when the resonant frequency is present in the pulse's spectrum. Figure 3.8 shows the time domain measurements of Gaussian pulses generated by the supply modulator. As the pulses become shorter, the 57 MHz ring becomes stronger in the output signal. Figure 3.8 also shows the normalized frequency domain

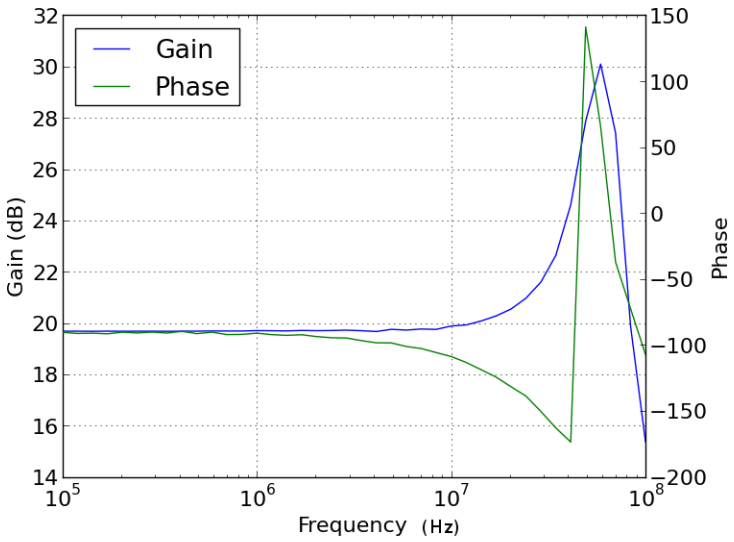

Figure 3.7: Measurement of the supply modulator frequency response into a 75 Ω load. Results show a resonance at 57 MHz.

representation of these pulses at the input of the modulator. One can see that the shorter blue and green traces have 57 MHz content in their spectra which cause the oscillation. The longer pulses without this content in their spectra exhibit no such oscillation.

The ringing is a symptom of the transient response with this load attached. Fig. 3.9 shows the step response, and this same ringing occurs, implying it is inherent to the system whenever high frequency content is present. Filtering is therefore essential for the input signals to the supply modulator. The ringing is caused by a capacitive pole which is too close to the unity gain point of the feedback network which results in low phase margin [44]. This could be solved by lowering the capacitance.

3.2.5 Connecting the PA to the Modulator

Loading the modulator with the dynamic PA load instead of a static resistive load impacts the performance of the modulator, and this must be characterized. Figure 3.10 shows the performance of the modulator when a Gaussian pulse is applied. For the first plot, the PA is in pinch-off and has a 1000 pF off-chip bypass capacitor. The time required to discharge the capacitor is unacceptable

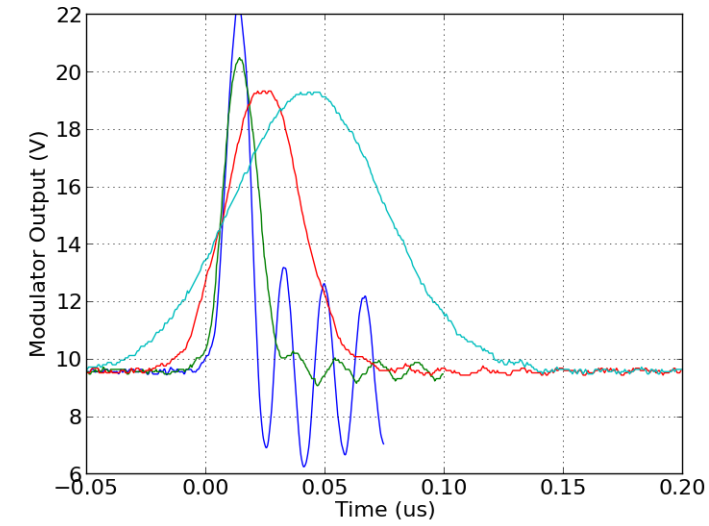

(a)

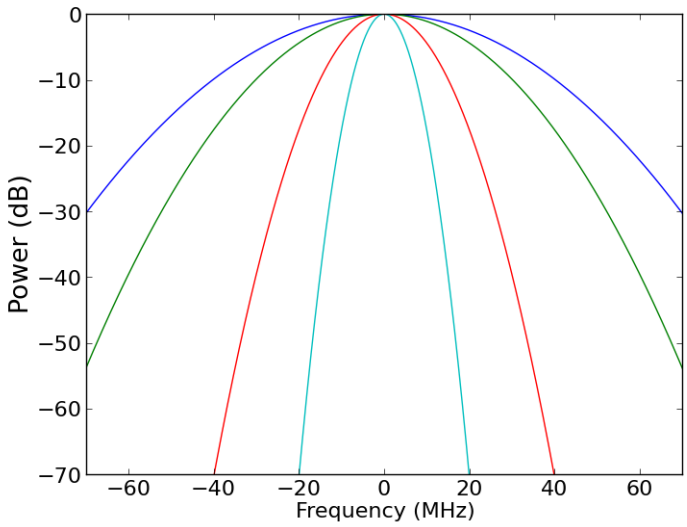

(b)

Figure 3.8: (a) Modulator time-domain response to Gaussian pulses of decreasing pulse widths. As the pulse becomes shorter, ringing from the transient response becomes more significant. The frequency content for these pulses (b) helps to demonstrate why the ringing is present. The shorter blue and green pulses contain 57 MHz content which excites the modulator resonance.

for this application; however, the capacitor is often needed for PA stability. This stresses the point that it is essential to design the PA for stability without a large bypass capacitance, as was the case for this amplifier. The next plot shows the result of the Gaussian pulse without the large off-chip

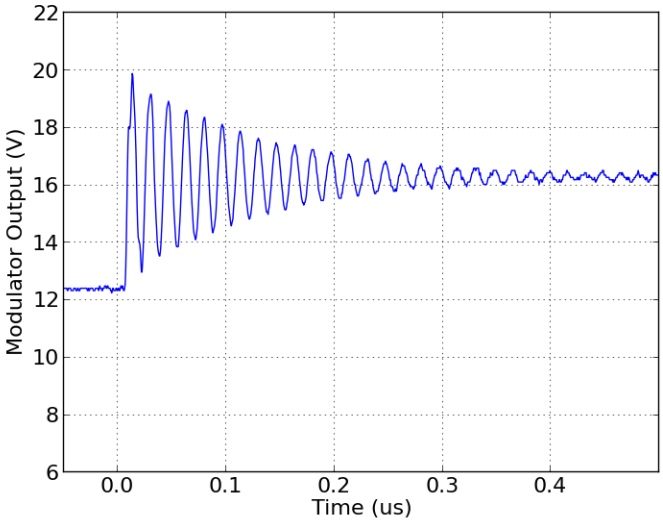

Figure 3.9: Step response for the linear modulator. The 57 MHz resonance causes ringing.

capacitor, but the amplifier was still biased in pinch-off. This was done to ensure the interaction of the modulator and PA would remain stable without damaging equipment. Lastly, when we were convinced it was safe to turn on the PA, we biased in Class AB and modulated the drain with a Gaussian pulse. The figure shows the drain is successfully modulated without any distortion or ringing.

3.2.6 Bench Alignment

Envelope tracking poses significant problems if $v_{dd}(t)$ is not synchronized at the drain with $v_{in}(t)$; it is essential that these two paths be properly time-aligned. One method to align the signals is to monitor the output waveform and compare it to what is expected. When the error between these two is minimized, good alignment is assumed [45][46]. Other methods include sweeping the delay and monitoring the ACPR for minimum out-of-band power [47]. Our novel method to achieve alignment is to use a chirp with a Gaussian envelope. Since a chirp crosses through the zero frequency when converted to base band, it provides an easily identifiable center point of the pulse. The amplitude of a Gaussian also peaks at the center of the pulse. Examination of the RF output

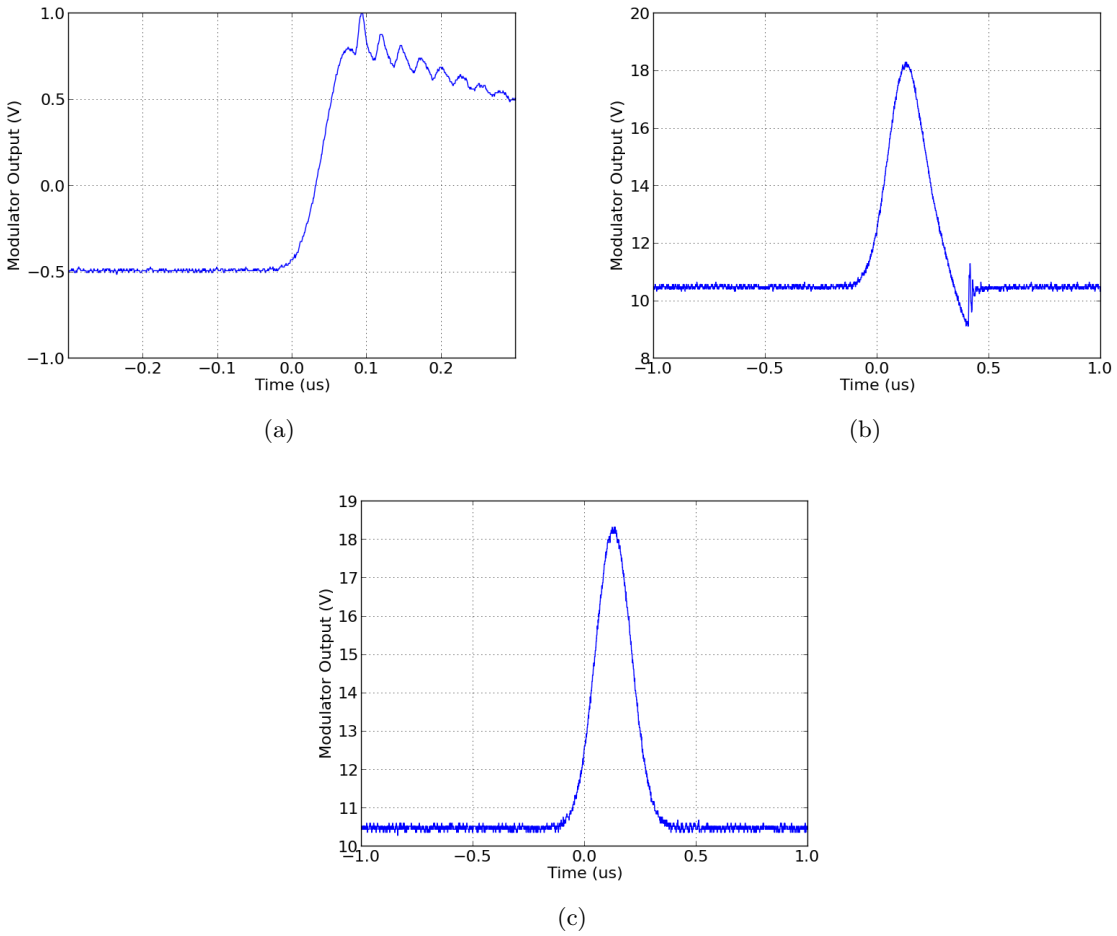

Figure 3.10: Measurement of the modulated PA drain voltage for (a) pinch-off conditions with an off-chip bypass capacitor, (b) pinch-off without the capacitor, and (c) Class AB operation without the capacitor. This steady progression to Class AB operation was performed to catch stability issues when they occurred; however, none were encountered.

shows the paths are aligned if the pulse peak and zero frequency occur simultaneously. This is not the case for the example in Figure 3.12 (a) because no alignment has been performed.

To align the signals, one must delay the RF path until the peak and zero phase point of the Gaussian chirp coincide. This is easier to see if one looks at the magnitude in dB and the derivative of the phase, as shown in Figure 3.12 (b). It turns out that this setup needs a 152 ns delay in the RF path. Good alignment results in the chirp shown in Figure 3.12 (c).

The accuracy of this approach depends on the sampling rate of both the AWG and PXA. Since the PXA has a slower sampling frequency, 150 MHz, it is the limiting factor in the measurement

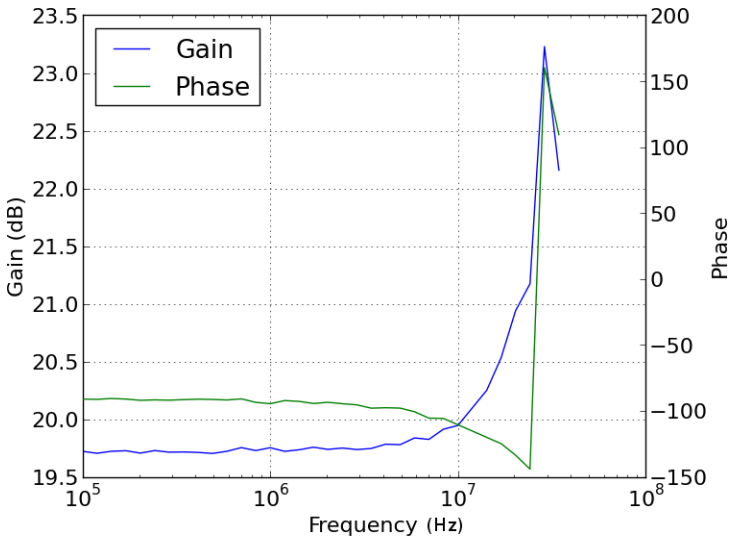

Figure 3.11: Bode plot of modulator when attached to the PA in Class-AB.

and limits the alignment accuracy to within 7 ns. We believe this method to be superior to other methods of alignment mainly because of its simplicity. However, it is also beneficial because one can "see" the alignment instead of inferring it from error measurements.

Note that a major part of getting the alignment to work is dealing with the peculiarities of the AWGs. The process for synchronizing the N8241 AWGs is covered in the manual: one needs to declare a master and a slave in software, then use the master reference and sync clock outputs as the inputs for both master and slave (as shown in Figure 3-8 of the reference manual [48]). What is not made clear is that the marker pulse width of the master needs to be wider than two cycles in the Ref Clock. Following this procedure is the only way to ensure the master is properly triggering the slave.

3.2.7 Characterizing the PA

One must characterize the PA for different drain bias levels to understand how to design the trajectory and implement supply modulation. This is done by sweeping the input power at each drain bias in stepped increments, for this measurement from 7 to 20 V. Within each power sweep

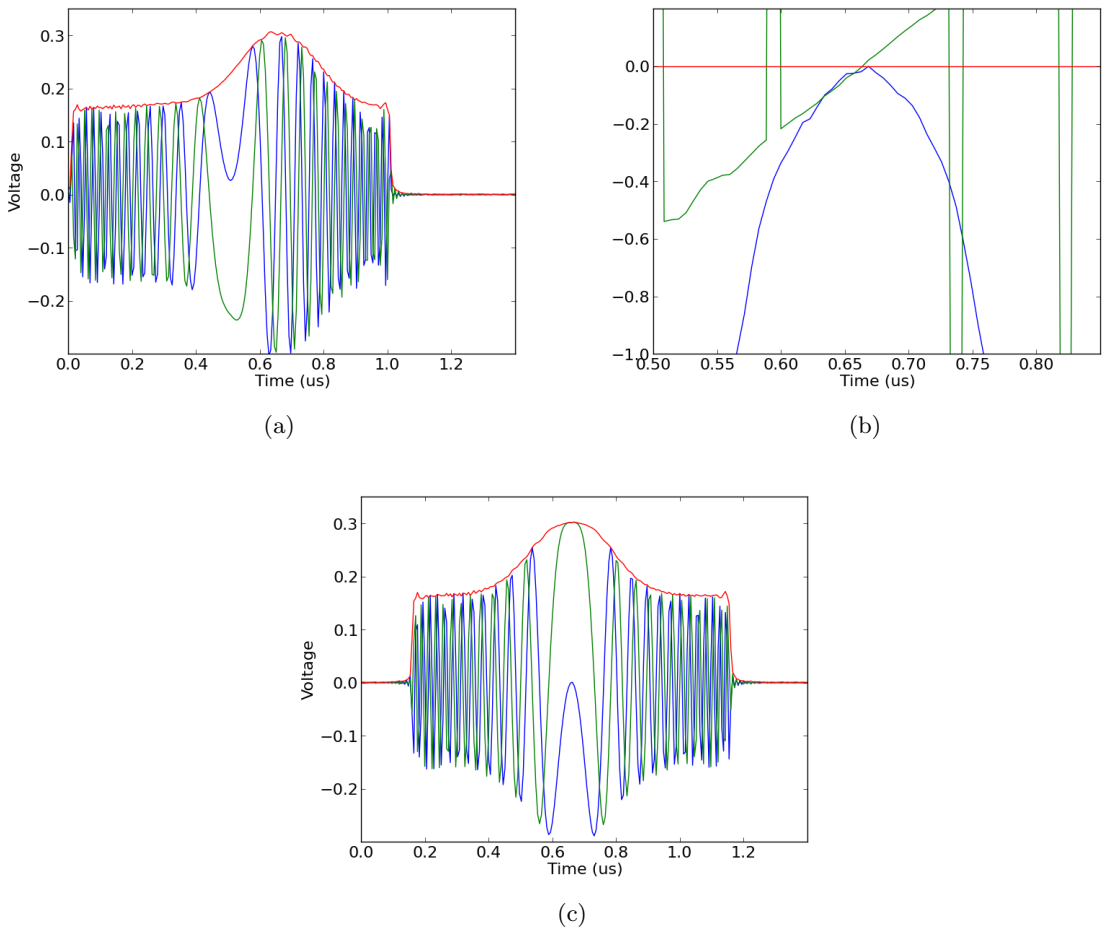

Figure 3.12: The IQ output from the PA before alignment (a), the magnitude and derivative of phase used to align the signal paths (b), and aligned IQ output after alignment is performed (c).

the output power, gain, and PAE are recorded. This was done for both the 4-Watt and 10-Watt X-Band MMIC PAs shown in Figure 3.13 and descibed in [15]. The measured gain and PAE are shown for the 4-Watt PA in Figure 3.14.

From the measurements shown in Figure 3.14, a trajectory for max PAE was designed. The algorithm which solves the trajectory works by sweeping through desired output powers. For each point in the sweep, it examines all the combinations of supply voltage and input power, and chooses the most efficient. The trajectory for both PAs is shown in Figure 3.15.

The trajectory is used to solve the drain supply waveform. To do this, the input signal is converted to dBm and the gain at the maximum output power is added to the input power waveform.

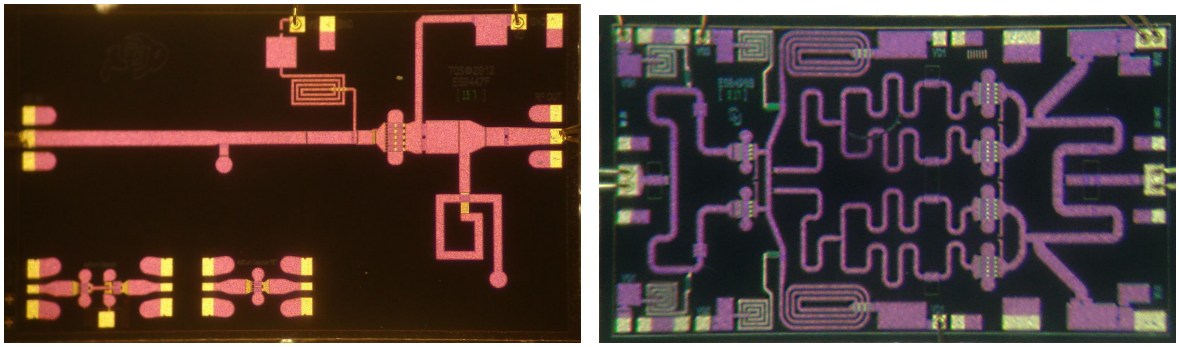

(a) 4-Watt (b) 10-Watt

Figure 3.13: Photographs of the two X-Band MMIC PAs used in supply modulation bench experiments. Both were made in the Triquint 0.15 μm GaN process. The 4-Watt PA is a single stage with 8 dB of gain at its peak CW PAE of 69.4% [15]. It has a total gate periphery of 1 mm and measures 3.8 mm x 2.3 mm. The 10-Watt PA has two stages with 27 dB of small-signal gain, and 22 dB compressed gain. The maximum CW efficiency was measured as 56%. The total output gate periphery is 3.6 mm and the chip size is 2.3 mm x 4.0 mm.

This expected output power waveform is used as the argument, or x-axis, for the trajectory function shown in Figure 3.15. The function output, or y-axis, is the corresponding drain voltage for that expected output power. Figure 3.16 shows a comparison of the efficiency of the different bias levels, in blue, to that of the maximum efficiency trajectory for supply modulation, in red. The PDF of the expected output power for the OFDM signal is superimposed over the efficiency to give a sense of the efficiencies for various output power levels.

The bandwidth of the drain waveform is about 20 MHz but we chose to filter it to 15 MHz to avoid the 30 MHz resonance of the supply modulator. It has been shown in [49] that filtering the drain waveform by as much as a factor of four only raises the ACPR from 3 to 5 dB. The waveforms of the pre-filtered and post filtered drain voltages are shown in Figure 3.17.

3.3 Measurements with an OFDM Signal

3.3.1 Linear Modulator with 15 MHz Bandwidth

The linear modulator bandwidth tested with a constant real load is about 50 MHz, but the PA is a dynamic complex impedance, limiting the stable bandwidth to slightly above 15 MHz, and

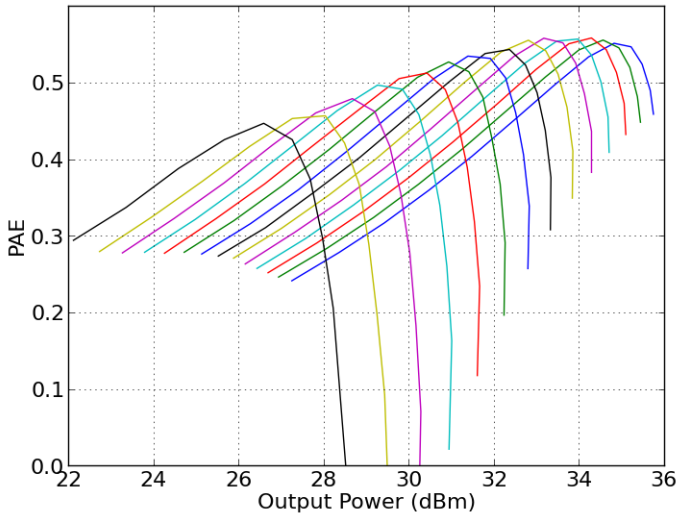

(a) PAE Sweep

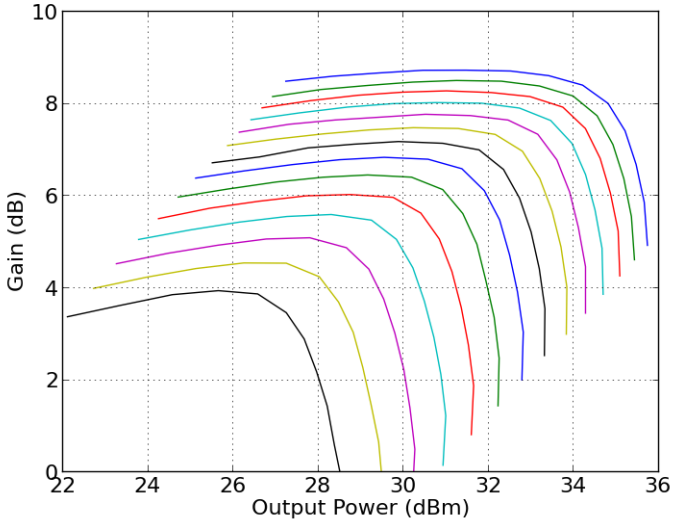

(b) Gain Sweep

Figure 3.14: (a)PAE and (b) gain of power amplifier plotted against input power for drain supply voltage stepped from 7 to 20 Volts. The data from these sweeps was used to design the trajectory for the 4-Watt PA.

the signal envelope was filtered to meet the stability by monitoring the Bode plot of the SM with the PA connected.

Fig. 3.18 shows measured spectra at the output of the 4-W MMIC integrated with the linear supply modulator. As the drain voltage decreases, the gain of the 4-W PA compresses. When the

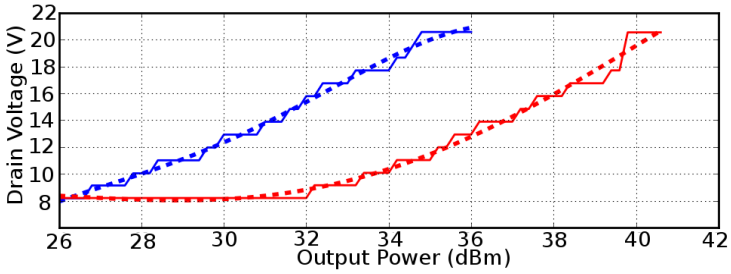

Figure 3.15: Trajectories for the 4-Watt (blue) and 10-Watt (red) MMIC PA. The trajectories were designed so that the drain voltage which provided maximum efficiency for output power was chosen. The solid lines represent the discrete results from the trajectory design algorithm while the dashed lines are polynomial interpolations of the discrete results. The interpolations are what are used to design the envelope signal from a expected output power waveform.

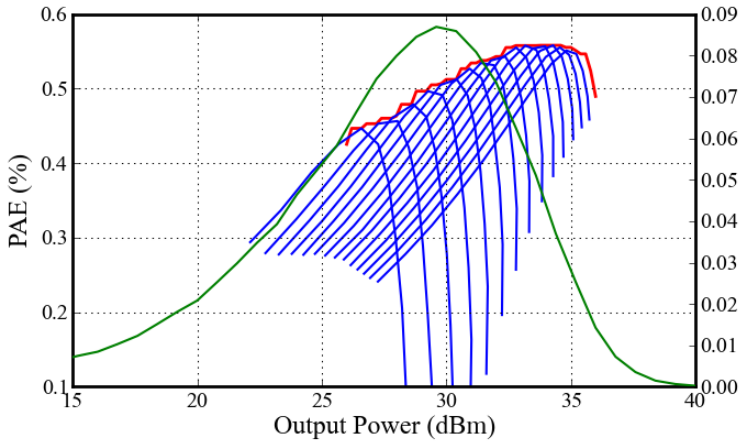

Figure 3.16: Comparison of the efficiency of an envelope tracked system (red) with that of a static bias systems for decreasing bias levels (blue) superimposed over a histogram of expected output power of an OFDM signal (green).

trajectory envelope information is input completely through the SM, the linearity is degraded with respect to the constant drain supply case, as expected [37]. After a signal split is applied using a look-up table derived from static gain measurements, the ACPR improves and can now be more easily linearized using DPD. Table 3.1 compares the constant supply, envelope tracking and signal split cases for the 4-W MMIC PA with the linear modulator. The supply modulation improves the efficiency by 20% but degrades the ACPR, while the signal split improves the ACPR with minimal impact on efficiency. The CPAE is lower than that for the constant bias case, as expected because

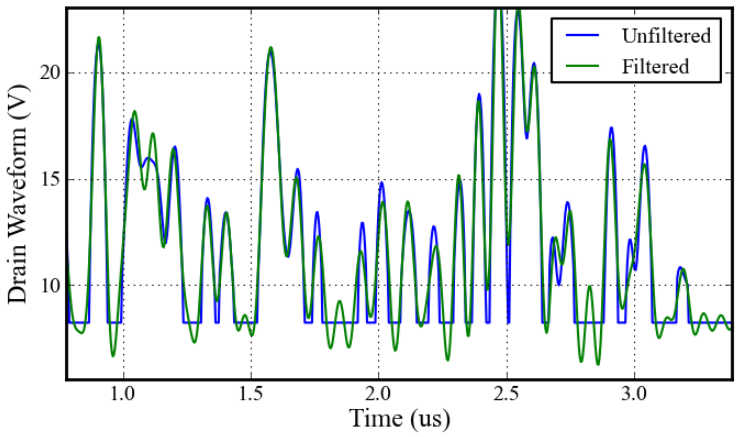

Figure 3.17: A comparison of the unfiltered drain waveform (blue), which results from applying the trajectory to the input waveform, to a filtered drain waveform (green). Filtering is applied so that the resonant frequencies in the modulator which cause ringing are avoided.

the SM is linear and shapes the drain waveform by dissipating power.

Table 3.2 shows the results with the 10-W MMIC. In this case, the signal split does not provide additional benefit, because the PA is biased in such a way that the trajectory follows constant gain contours, even with a maximum efficiency trajectory. In this two-stage PA with only final-stage supply modulation, and with the inefficient linear supply modulator, the CPAE nevertheless increases to 23% from the 13% efficiency for a constant 20-V supply.

3.3.2 EER with a 5-MHz Switching Modulator

Since the linear supply modulator is inefficient, the 4-W PA is also characterized with the 5-MHz efficient switching modulator. The switching modulator used in these experiments does not have an input port, but rather plays a waveform stored in memory. Additionally, it does not accept a trigger. Instead, it provides the trigger. This made it difficult to initially align the $v_{dd}(t)$ and $v_{in}(t)$. For this reason, envelope elimination and restoration (EER) was used since it does not require time alignment. From Table 3.1, the CPAE is 35.8%, which includes the losses of the SM. In this measurement, the input is always at peak power, which reduces overall efficiency. The

Table 3.1: Summary of Results with 4-Watt PA

	Constant Supply	Modulated Supply	Signal Split	EER
Channel Power (dBm)	30.6	28.6	28.5	30.8
Peak Power (dBm)	36.3	36.5	36.5	35.5
Gain (dB)	8.5	6.4	6.4	-
PAE	43.9%	65.4%	62.6%	-
CPAE	43.9%	34.8%	33.1%	35.8%
$\eta_{Composite}$	-	-	-	60.4%
Drain Current (mA)	108.0	75.6	80.2	83.6
ACPR (dB)	-27.1	-23.3	-28.0	-

Table 3.2: Summary of Results with 10-Watt PA

	Constant Supply	Modulated Supply
Channel Power (dBm)	32.5	31.8
Peak Power (dBm)	40.3	40.3
Gain (dB)	20.4	19.6 dB
PAE	13.3%	41%
CPAE	13.3%	23.3%
Drain Current (mA)	282	255
ACPR (dB)	-26.2	-23.1

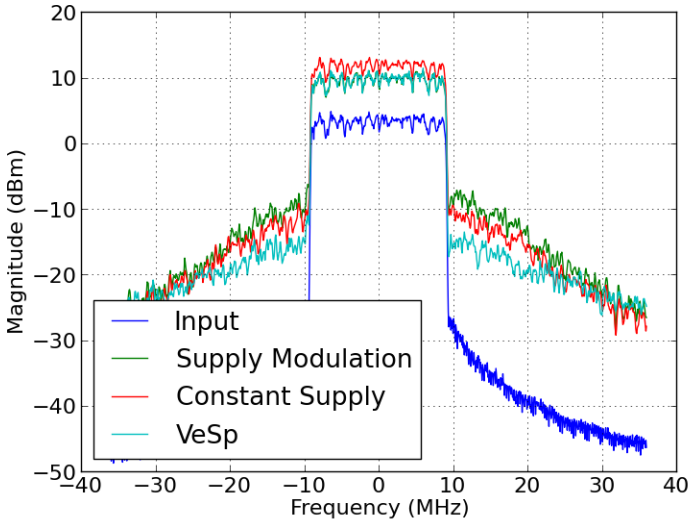

Figure 3.18: Normalized power spectra of the input, modulated supply, signal split, and constant supply for the purposes of showing spectral regrowth.

composite drain efficiency, calculated as

$$\eta_{Composite} = \frac{\int_0^{T_w} P_{out}(t)\,dt}{V_{DD}\int_0^{T_w} I_{ds}(t)\,dt} \tag{3.4}$$

where T_w is the period of the waveform stored in the switching modulator's memory. The result of this efficiency is $\eta_{Composite} = 60.4\%$ which is much higher than the CPAE since it does not depend on the unaligned input drive. Given the PAE of the amplifiers and the efficiency of SM, the projected CPAE is above 55%.

After the EER measurement, we attempted to make an aligned measurement of the PA and switching modulator. The alignment procedure with the switching modulator triggering the rest of the bench was successful, but the resulting measurement was unstable. The system was stable when the drain was modulated and the PA was driven with CW. However, it became unstable when the PA input and drain were modulated simultaneously.

3.4 System-Level Simulations of a Supply-Modulated Power Amplifier

It is without question that computer aided design tools have helped the microwave community to design better systems. For example, tools like electromagnetic solvers give much more insight into how passive networks will behave compared to circuit solvers, which don't consider effects like coupling between traces. The Method of Moments (MoM) is the preferred method for planar circuits, but Finite Element Method (FEM) and Finite Difference Time Domain (FDTD) can be used for more complex 3-D structures [50]. Additionally, non-linear transistor models, such as the Angelov Model, developed at Chalmers University [51][52], have allowed for more accurate simulation of non-linear transistor circuits than older S-Parameter measurements and linear models [53]. The combination of better passive simulators and active models have drastically lowered the risk in designing MMIC PAs, at least in CW scenarios.

Even tools that can solve the currents in non-linear circuits, such as harmonic balance [54], are only able to solve steady-state results. Newer techniques, classified as envelope simulators, are able solve waveforms with amplitude and phase modulation, and centered around a carrier frequency [55]. The envelope simulator works by sampling the modulated signal at a frequency much lower than the carrier frequency. This is permissible because it is assumed that the carrier frequency is much higher than the bandwidth of the modulation. A harmonic balance is then performed at the carrier frequency, with the amplitude and phase of the sample point as the source, for each sample point. Keysight Technologies Advanced Design System (ADS) and Applied Wave Research (AWR) Microwave Office both have tools for circuit envelope simulations. To our knowledge, a complete simulation of a supply-modulated transmitter has not been demonstrated or published. In this section, we chose the National Instruments (formerly Applied Wave Research) Microwave Office circuit simulator with VSS system simulator to perform simulations of an X-Band 10-Watt GaN MMIC with a GaN switching supply modulator. The VSS system simulator is used for signal processing operations not implemented in circuitry, such as alignment, applying the LUT, and generating Pulse Width Modulation (PWM) waveforms for the switcher, while the circuit envelope

simulator is used for integrated simulation of the switcher and PA [1] .

3.4.1 ADS Validation of Fixed Bias

The envelope simulator for AWR is a new feature in the 2014 version software, so it required validation. To do this, we compared it to the results from a simulation in Agilent's ADS Ptolomy tool, which is also not validated. The circuit used is a two-stage 10-Watt Class-E GaN MMIC, Circuit B from [15]. The total gate periphery is 3.6 mm and the maximum output power is 13.2 W at 59.9% PAE. In both the Agilent and NI/AWR simulations, the circuit is simulated using the system simulator with a circuit envelope simulator as one of its system blocks. The envelope simulator has two inputs: an 18 MHz OFDM signal with a PAPR of 10 dB, and a constant 20 V signal used to bias the drain of the final stage of the PA. The resulting output waveforms from ADS are compared to those of AWR in Figure 3.19. One can see the magnitude of the load voltage follows the same trend for both simulators. There are instances where the magnitude differs by as much as 7 V. We are not privy to the source code of these simulators or the non-linear models of the devices, so we are not certain of the causes of these differences. However, we are satisfied with the similarities of the simulators to continue with system level supply-modulation simulations. To get another look at how the data compares, Figure 3.20 shows the histograms of the load voltage for the two waveforms. Again, the results are similar and gave us confidence that the AWR simulator was working as it should.

3.4.2 Ideal Supply Modulation of an OFDM Signal

An ideal supply modulator can be implemented in the envelope simulator using the input signal and mathematical blocks. The mathematical blocks condition the input wave such that it can be used in a Look-Up-Table (LUT) to find the desired drain voltage for a given input power level. The LUT is based on a trajectory, such as the one in Figure 3.15. The output of the

[1] The author would like to thank David Sardin for his initial work on ADS envelope simulation of a full transmitter. Without his prior work and inputs, the task of an envelope simulation in Microwave Office/VSS would have been considerably more difficult.

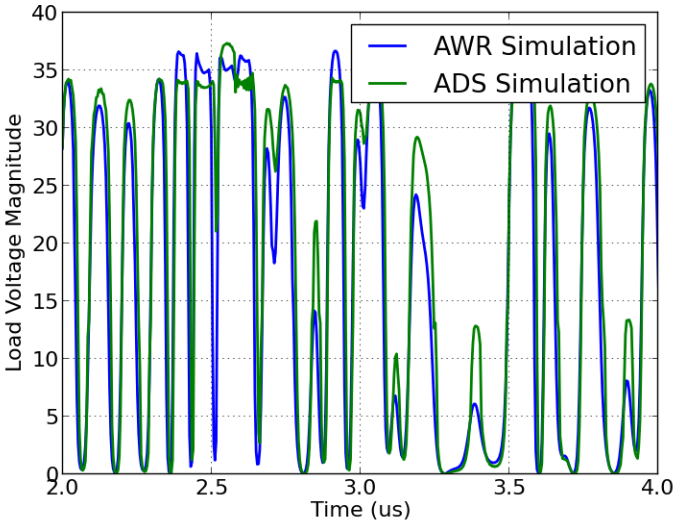

Figure 3.19: A comparison of the load voltage magnitudes for an 18 MHz OFDM signal in the ADS and AWR envelope simulators. These results show good agreement of time-domain waveforms.

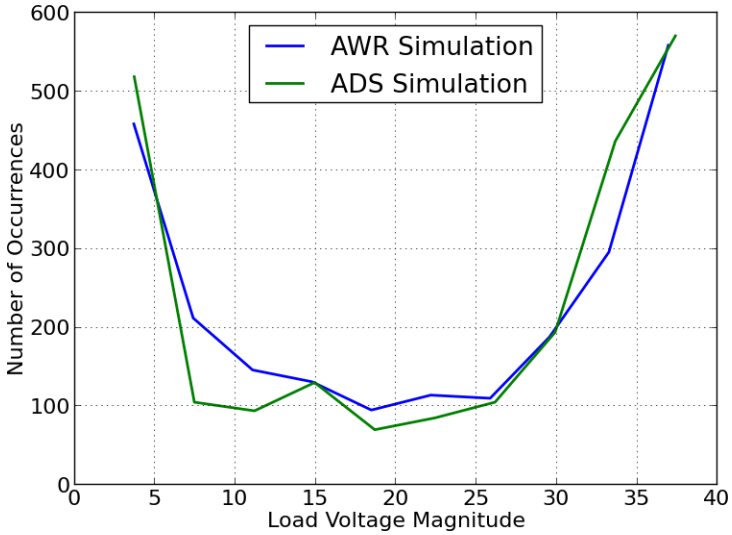

Figure 3.20: Another comparison of the results of ADS and AWR envelope simulators shown as a histogram of signal amplitude. The total number of samples plotted is 2300.

LUT forces the drain voltage in the envelope simulator. This supply modulator is said to be ideal because mathematical blocks do not have any losses associated with them. Although the blocks in the simulator differ between AWR and ADS, they consist of solving for the input wave power,

converting to decibels, limiting the power level, and applying the LUT. The ideal supply modulators are shown in Figure 3.21 for both simulators.

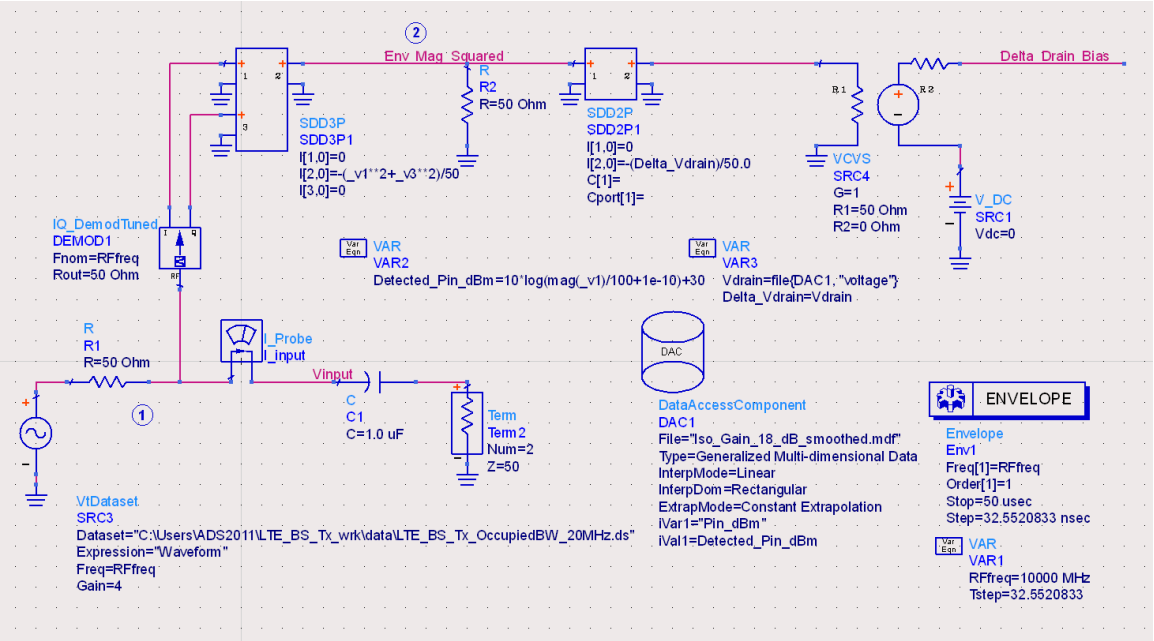

(a) ADS Schematic

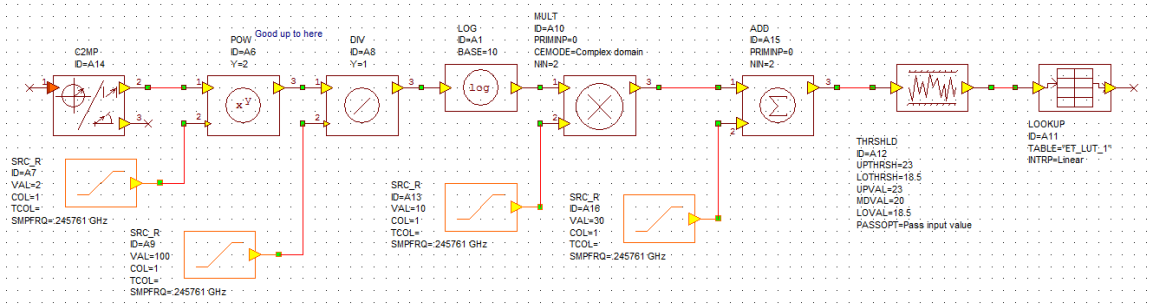

(b) AWR Schematic

Figure 3.21: Schematics of ideal supply modulators for envelope simulators in both (a) ADS and (b) AWR. They perform the necessary functions of solving the input wave power in decibels and applying a LUT.

Two configurations were considered when testing the ideal supply modulation simulations: (1) the first stage of the PA was biased with 20 V while the second was modulated and (2) both stages were modulated with the same drain waveform. The time domain output waveforms of these two simulations are compared to those of a constant bias simulation in Figure 3.22. One should not expect exact agreement since different techniques are being used, but the similarity shows that

supply modulation produces similar results. Figure 3.23 shows the efficiency improvement for the two supply modulated simulations over constant bias. Both cases of supply modulation show an efficiency improvement in the backed off output power region. When backed off 10 dB from the peak power, the constant bias condition has a PAE of about 15% while modulating the final stage shows about 30% and modulating both 35%. Additionally, the average PAE shows an improvement from 32.3% to 47.0% for modulating the final stage and 51.8% for modulating both. It should be noted that while it appears modulating both stages seems preferable from an efficiency standpoint, Figure 3.23 shows that it experiences negative PAE for power levels backed off more that 25 dB. Since the PAE of modulating both stages is increased for high output power levels, there is a clear benefit to modulating both stages, but at the expense of gain for lower power levels. We recommend investigating using separate trajectories for the two stages to optimize PAE without incurring loss at lower output powers. This of course requires a second supply modulator and added complexity, but the first stage modulator would be lower power and it's efficiency would be less important.

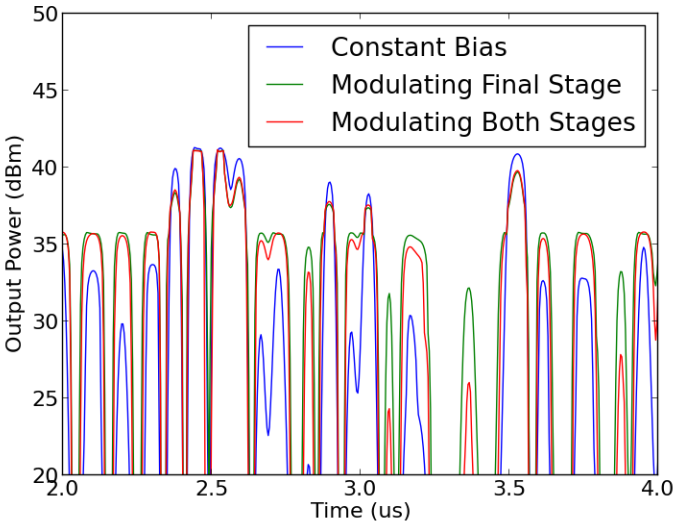

Figure 3.22: A comparison of the output waveforms from the 10-W X-Band GaN MMIC for the cases of constant bias and supply modulation. The supply modulation cases either modulate the final stage of the amplifier only, or both.

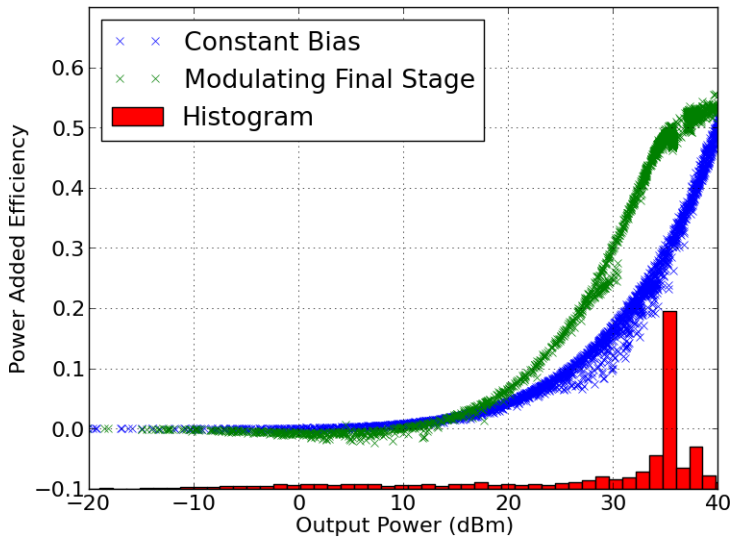

(a) Final Stage Modulation Only

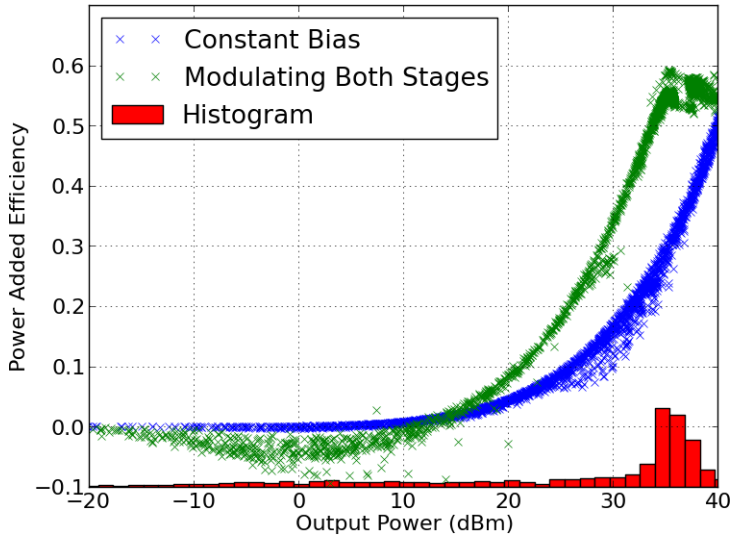

(b) Both Stages Modulated

Figure 3.23: A comparison of efficiency for both supply modulation schemes to a constant bias superimposed on a histogram of the output waveform. Modulating both stages shows an improvement in efficiency, but incurs a loss at low power levels.

3.4.3 Switching Supply Modulator

The ideal mathematical supply modulator provides information on how the PA behaves under supply modulation conditions, but is not physically realizable. A true supply modulator will have

its own efficiency, which will impact total system efficiency. Additionally, the interaction of the modulator and PA will change how the system operates. For instance, the drain of the PA will be constantly changing because of the varying signal level and thus output power. This impedance will load the modulator differently than the static load with which a modulator is normally tested. To understand how the full system behaves, the PA was simulated with the switching modulator shown in Figure 3.24.

The switcher operates at a switching speed of 100 MHz and is controlled by two complimentary PWM sources: one for the high-side switch and the other for the low-side switch. The system is considered "on" when the high-side switch is closed (high-logic) and the low-side is open (low-logic); it is "off" when the opposite is true. The PWM signals are generated by comparing the desired waveform to a 100 MHz sawtooth wave. For instances where the desired wave is greater than the sawtooth, the PWM waves are in the on-state. That is, a high value for the high-side switch and low value for the low-side switch. When the desired waveform is less than the sawtooth, the two PWM waves are in the "off" state. An example of the switcher output compared to a desired waveform is shown in Figure 3.25. In this simulation, the switcher is merely tracking a voltage that varies from 0-20 V, but it is not representative of a drain voltage used in supply modulation since it is not the product of a trajectory application.

It would be ideal to characterize the switching modulator via simulation in the same way that the linear modulator on the test bench was characterized by measurement. However, techniques have not yet been devised in microwave circuit simulators to perform a frequency sweep of the circuit with the system simulator since each frequency point takes a long time to simulate. Instead, the simulation was performed at four different tones with the results shown in Figure 3.26. The figure shows that the circuit is behaving poorly at 30 MHz.

So that we could use the switcher in a supply modulation simulation similar to the ideal simulations, we tested it with the voltage waveform from the trajectory function. The trajectory hard limits the lowest voltage to 10 volts, so it has sharp edges with high frequency content. It was just shown in Figure 3.26 that the modulator is frequency limited, so it is necessary to band-limit

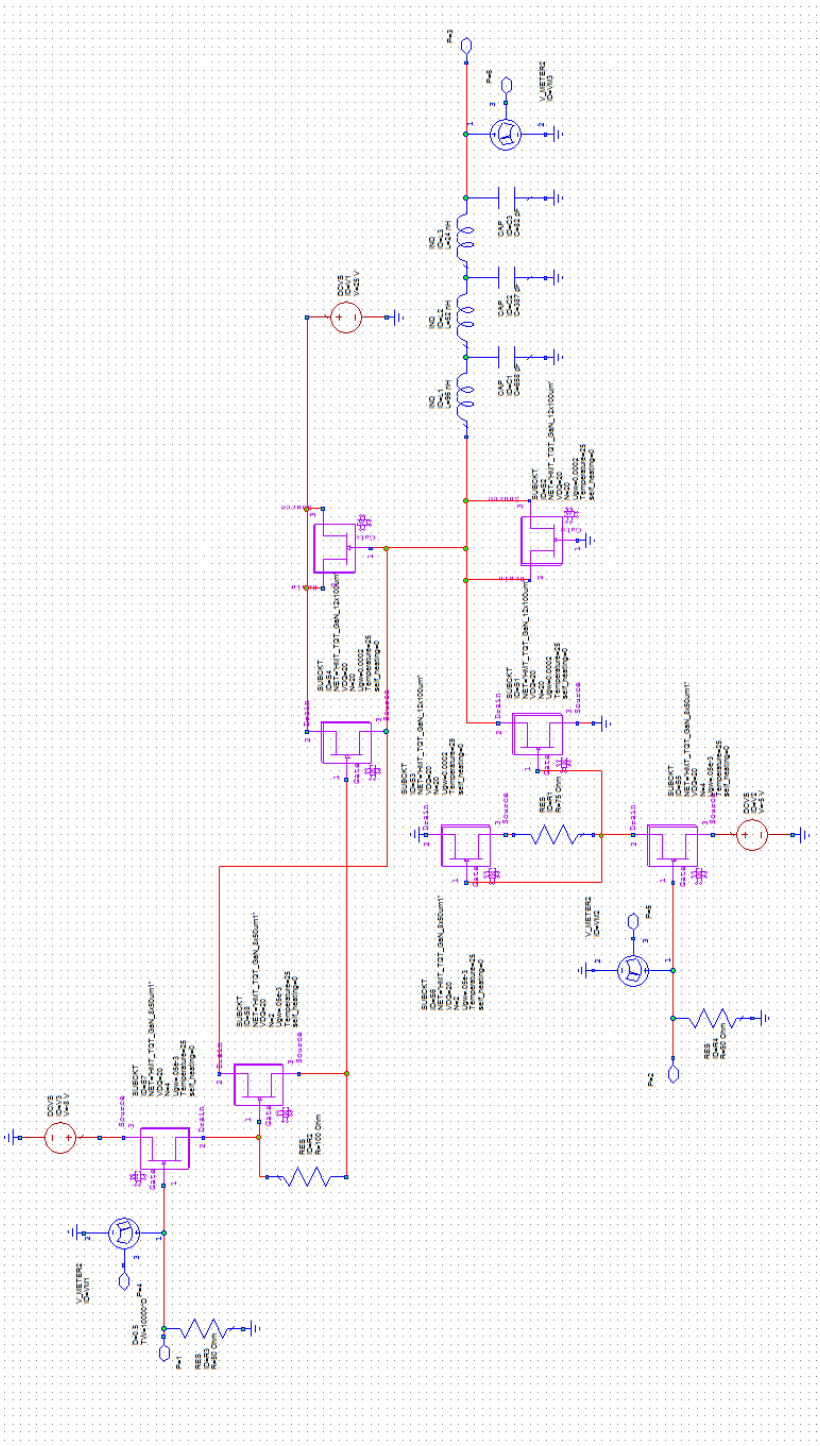

Figure 3.24: Schematic of the switching modulator simulated in AWR. Major components are the high-side switch, which connects the output to the supply voltage, and low-side switch connecting the output to ground. Each are independently controlled by complimentary Pulse Width Modulation (PWM) signals. The output is filtered by the low-pass LC-filter.

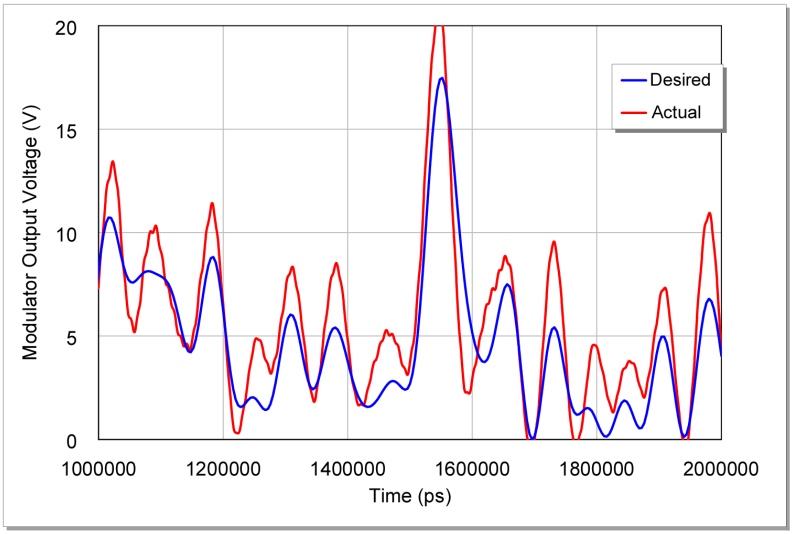

Figure 3.25: Comparison of the switcher's output voltage to the desired voltage. This was the initial test waveform used to ensure the PWM generator was working properly and that the switching modulator could track a varying voltage. The real voltage the switcher must track is the output of the trajectory, which does not go below 10 V and has higher frequency content.

the input of the switcher. This is done with the algorithm of [49] with the block diagram shown in Figure 3.27. The low-pass filters have a -3 dB point at 15 MHz. The output of the algorithm and the switcher's response to it as an input are shown in Figure 3.28.

The results of the full supply modulated circuit are shown in Figure 3.29. The switcher has its own efficiency of 80%, so the peak efficiency is not as high as the constant bias case; however, the backed-off efficiency is much higher than the constant bias, even with the efficiency of the modulator considered. In fact, the CPAE improves from 36.0% for the constant bias to 49.2% for supply modulation.

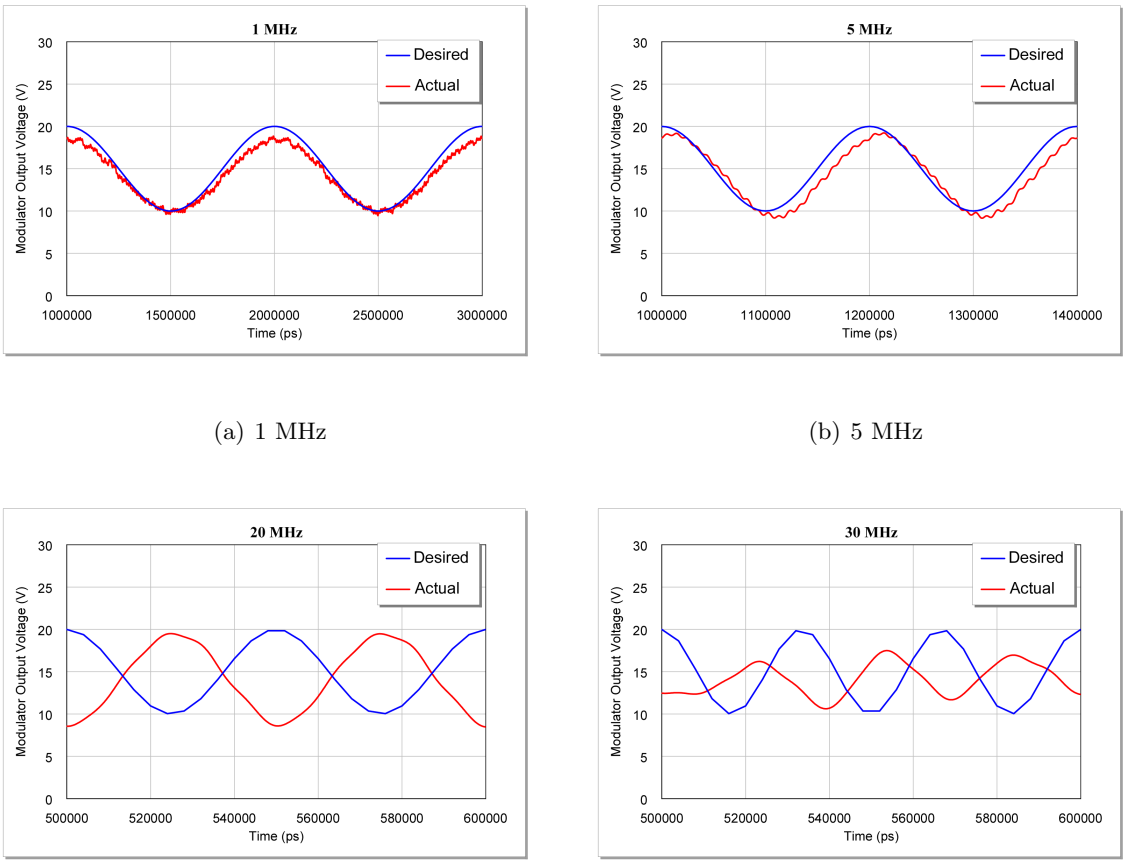

(a) 1 MHz

(b) 5 MHz

(c) 20 MHz

(d) 30 MHz

Figure 3.26: A comparison of the desired sinusoidal output of the switcher to the simulated results. There is a frequency depended phase shift which corresponds to a time-delay for a band-limited signal. At 20 MHz, the switcher starts to show signs that it is not able to track the signal. However, at 30 MHz, the modulator is no longer able to reliably track the signal at all.

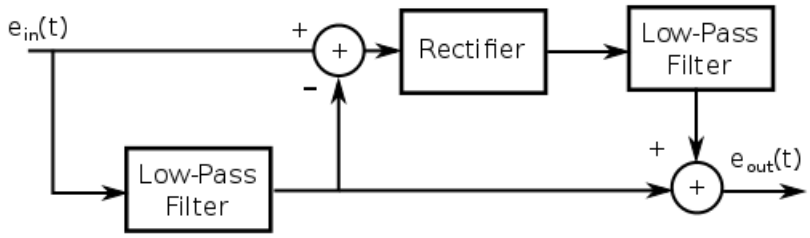

Figure 3.27: Block diagram of the filtering algorithm from [49]. This algorithm ensures that the signal is band-limited while the output waveform traces the peaks of the input waveform. The rectifier is not a circuit block with a non-linear diode model, but rather a mathematical block. It gives the magnitude of positive values and outputs zero for negative values.

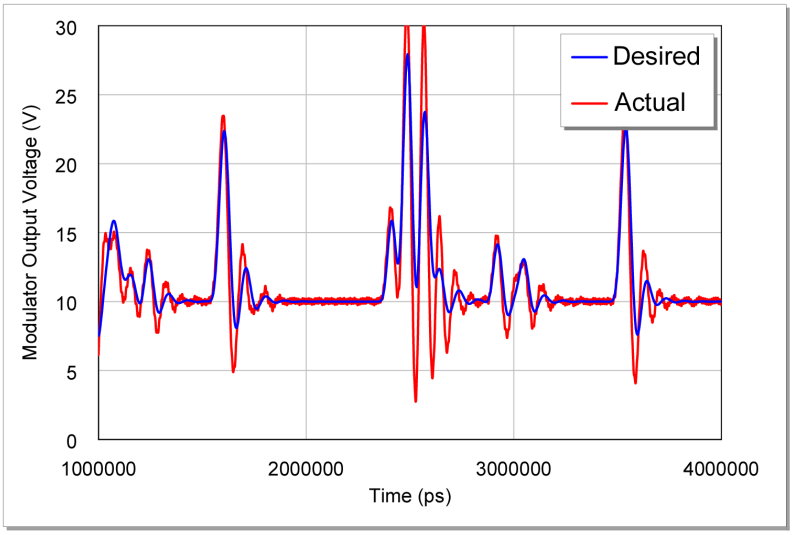

Figure 3.28: Comparison of the switcher's output voltage to the desired trajectory voltage. This measurement is representative of the drain voltage waveform that is applied to the PA, but is simulated into a static 100Ω load for this test.

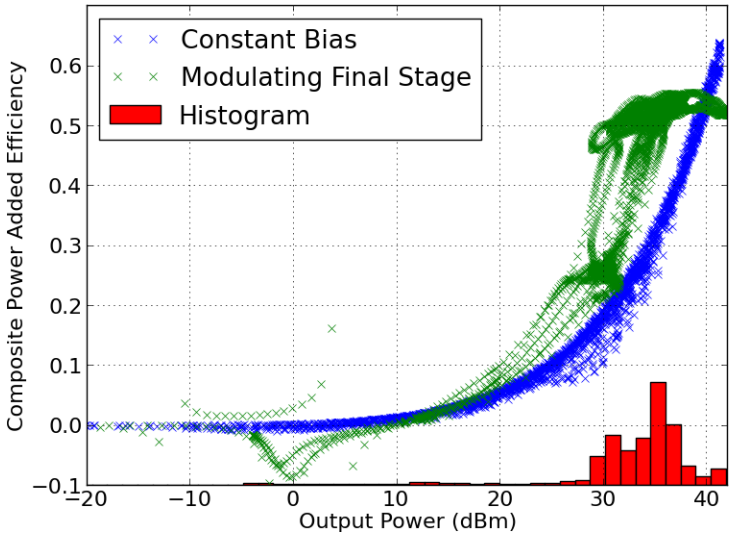

Figure 3.29: A comparison of instantaneous efficiency for a constant bias and switching supply modulated PA. The efficiency metric is CPAE, so the efficiency of the switcher is included. The average efficiency increased from 36.0% for the constant bias to 49.2% for supply modulation. The area of negative gain around 0 dBm of output power is presumed to be caused by low bias voltage levels. Figure 3.28 shows the switching modulator cannot perfectly track the bias voltage and swings down below 5 V, a bias which incurs loss instead of gain.

Chapter 4

Resonant Supply Modulators

4.1 Resonant Modulator Theory

Supply modulation of RFPAs has recently been applied in envelope tracking transmitters, e.g. [56][37], or to improve operation of outphasing [57] and Doherty PAs [58][59], with a primary goal to improve transmitter efficiency for high peak to average ratio signals. In these architectures, the supply modulation is typically done with an efficient switching dc-dc converter assisted with a linear amplifier that provides the required bandwidth [60]. In principle, this approach can be applied to radar transmitters to generate the Gaussian-type amplitude envelope modulation described in the previous chapter. However, supply modulators applied to communication signals with high PAPRs typically cover amplitude values from some V_{min} to V_{max}, where $V_{min} > 0$. In the radar case, the envelope goes to zero between pulses, and the envelope waveform is known *a priori*. A simpler approach, which is also potentially more efficient compared to a more standard envelope modulator, is a supply modulator based on a damped resonant circuit, first demonstrated in [61][62]. In [61], a 15-μs pulse with an approximately Blackman shape (PAPR = 4 dB) and with no frequency modulation was applied to a 2-GHz PA and showed about 10-point improvement in efficiency over a directly driven PA. The modulator in [62] exhibits a very high efficiency of 90% at 20 V peak voltage.

The modulator circuit shown in Figure 4.1 has three different states: (1) has S_1 closed and the other two switches open; this can be thought of as a charging configuration since it is providing energy to the circuit via V_D; (2) the discharging state in which V_D is disconnected from the circuit

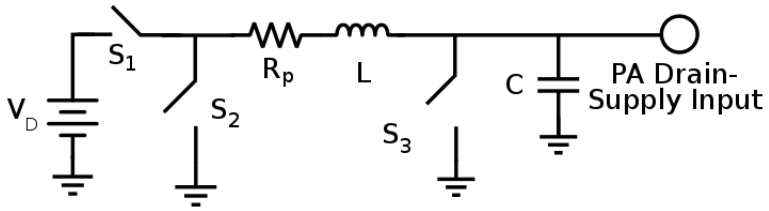

Figure 4.1: The schematic for the resonant modulator circuit. The circuit uses the resonance of the inductor and capacitor to shape the waveform applied to the drain of a PA. Switches S_1 and S_2 are used to connect and disconnect the voltage source. S_3 is used to discharge the circuit when the modulator is not in use. The switches are controlled with digital logic, a Field Programmable Gate Array (FPGA) in this thesis. The timing of switching between states will be discussed in this section.

by opening S_1 while closing S_2. This state essentially replaces V_D with a zero volt source, or short circuit; and (3) the "off" state, with S_2 and S_3 closed and S_1 open. This state is similar to State (2) in that it disconnects the source, but the purpose is to remove energy from the circuit as quickly as possible. State (3) is used at the end of a resonant pulse, and the circuit is left in this state between pulses. The schematic for States (1) and (2) can be simplified to what is shown in Figure 4.2, where R represents the load presented by the PA and R_p represents parasitic resistances in the switches and lumped elements. The source $V = V_D \neq 0$ in State (1) and $V_D = 0$ in State (2).

A state-plane analysis of this circuit was done in [62]. Instead, we focus our analysis in the time-domain. To understand how switching between states shapes the waveforms, consider the general solution to $v_{dd}(t)$ in Figure 4.2. Using Kirchhoff's Voltage Law, one can solve the drain voltage to be

$$v_{dd}(t) = V_D - i_L(t)R_p - \frac{di_L}{dt}L \tag{4.1}$$

and use Kirchoff's Current Law to solve the inductor current to be

$$i_L(t) = \frac{dv_{dd}(t)}{dt}C + \frac{v_{dd}(t)}{R}. \tag{4.2}$$

These equations are fundamental to solving the shape of the waveform as the circuit switches between states. In this analysis, we only consider the voltage waveform. An important point to keep in mind is that lower values of the resonant circuit Q factor will result in lower current peaks,

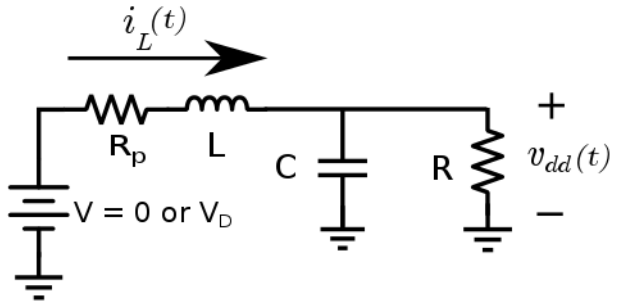

Figure 4.2: Equivalent circuit for the resonant modulator in State (1) and (2). The inductor current, $i_L(t)$, and load voltage, $v_{dd}(t)$, are used in the analysis of the waveform shape.

and thus less resistive losses in R_p. The solution to (4.1) and (4.2) is

$$v_{dd}(t) = e^{-\omega_0 t/2Q}\left(A\cos(a\omega_0 t) + B\sin(a\omega_0 t)\right) + V_D \tag{4.3}$$

where $\zeta = \sqrt{L/C}$, $\omega_0 = 1/\sqrt{LC}$, $Q = 1/(\frac{R_p}{\zeta} + \frac{\zeta}{R})$, $a = \sqrt{1 + (R_p/R) - (1/2Q)^2}$, and $V_D = 0$ in State (2). To solve for the constants A and B, the following initial conditions are used:

$$v_{dd}(t^-_{switch}) = v_{dd}(t^+_{switch}) \tag{4.4}$$

and

$$\frac{dv_{dd}(t^-_{switch})}{dt} = \frac{dv_{dd}(t^+_{switch})}{dt}. \tag{4.5}$$

In the above boundary conditions, t^-_{switch} indicates the time just before switching, t^+_{switch} the time just after, and

$$\frac{dv_{dd}(t)}{dt} = -\frac{\omega_0}{2Q}e^{-\omega_0 t/2Q}\left((2AQa + B)\cos(a\omega_0 t) + (A - 2BQa)\sin(a\omega_0 t)\right). \tag{4.6}$$

Our method uses a numerical approach to solve the coefficients A and B for the three intervals: State (1), State (2), State (1). The first switching time, t_1, is when the circuit transitions from State (1) to State (2), and t_2 is when the circuit returns to State (1) from State (2).

An example of the output of this method is shown in Figure 4.3. In this simulation L = 20 μF, C = 100 nF, $R = 220\,\Omega$, $R_p = 0.8\,\Omega$, and $V_D = 10$ V. The two switching times are at $t_1 = 4\,\mu$s and $t_2 = 6\,\mu$s. The figure shows the solution to (4.3) for the three different intervals with the stitched

together waveform comprising of the three. Obviously, this is not a Gaussian shape and would be an undesirable waveform. These results are shown merely to demonstrate the algorithm which solves how the circuit behaves with switching. The voltage can now be entirely described by

$$v_{dd}(t,t_1,t_2) = \begin{cases} -e^{-\omega_0 t/2Q} V_D \cos(a\omega_0 t) + V_D & : 0 < t < t_1 \\ e^{-\omega_0 t/2Q} \left(A_2 \cos(a\omega_0 t) + B_2 \sin(a\omega_0 t)\right) & : t_1 < t < t_2 \\ e^{-\omega_0 t/2Q} \left(A_3 \cos(a\omega_0 t) + B_3 \sin(a\omega_0 t)\right) + V_D & : t_2 < t < t_{end} \end{cases} \tag{4.7}$$

where A_2 and B_2 are dependent on t_1 and A_3 and B_3 are dependent on t_2.

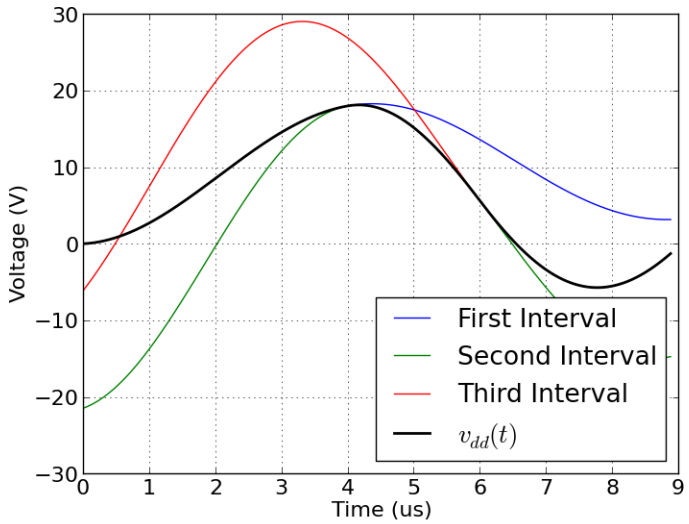

Figure 4.3: An example waveform of $v_{dd}(t)$ for L = 20 μF, C = 100 nF, R = 220 Ω, R_p = 0.8 Ω, and V_D = 10 V. The three intervals are plotted independently with their appropriate boundary conditions solved. The black trace represents $v_{dd}(t)$ as it is switched between these intervals.

To solve for a Gaussian shape using this method, a criteria for optimization needs to be established. For this optimization, two times are defined: t_{max} and t_{end}. The first time annotates the time when $v_{dd}(t,t_1,t_2)$ is at is maximum value, the other when $v_{dd}(t,t_1,t_2)$ is at it's minimum, which we choose to be the end of the pulse. These times are unique from, and not to be confused with, t_1 and t_2, which specify the change from State (1) to State 2 and from State (2) to State (3), respectively. Three conditions need to be satisfied:

$$v_{dd}(t_{end},t_1,t_2) = 0 \tag{4.8}$$

$$t_{end} = 2t_{max} \tag{4.9}$$

and

$$t_{end} = T_p, \tag{4.10}$$

where T_p is the desired pulse width and is enforced by (4.10). Condition (4.8) constrains the voltage to zero at the desired pulse width and (4.9) is meant to approximate symmetry.

To solve the t_1 and t_2 which best meet (4.8)-(4.10), we examine the set of all $v_{dd}(t, t_1, t_2)$ where $0 \leq t_1 \leq t_2 \leq T_0 = 2\pi\sqrt{LC}$ and apply the cost function

$$J(v_{dd}(t_{end}, t_1, t_2)) = |v_{dd}(t_{end}, t_1, t_2)| + |t_{end} - 2t_{max}| + |t_{end} - T_p| \tag{4.11}$$

and use the set member which minimizes the cost function $J(v_{dd}(t_{end}, t_1, t_2))$. Strictly, t_{max} and t_{end} should be the roots of $dv_{dd}(t_{end}, t_1, t_2)/dt$, but they do not always exist and our method uses numerical techniques instead of differentiation. The results of this method are shown in Figure 4.4 for a circuit using the same values as used in Figure 4.3. These results show that pulses close in shape to the Gaussian can be created with this circuit and new method. Additionally, this method allows for the design of pulses where T_p is shorter than the resonant period of the circuit, T_0; however, the shorter pulses have peak voltages lower than the longest pulse because the resonant circuit does not charge as long for shorter pulses. The error for the pulse is calculated as

$$\epsilon_{mod} = \sqrt{\frac{\int_0^{T_p} |v_{out}(t) - v_{desired}(t)|^2 dt}{\int_0^{T_p} v_{desired}(t)^2 dt}} * 100 \tag{4.12}$$

where v_{out} is the simulated output voltage of the resonant modulator and $v_{desired}$ is the desired Gaussian shape. The error for each of the simulated pulses is shown in Table 4.1 and a comparison of v_{out} and $v_{desired}$ is shown in Figure 4.5.

4.2 Resonant Modulator Simulations and Measurement

With the results obtained to solve for the switching times, the circuit is implemented in NI/AWR Microwave Office and VSS. Again, the values L = 20 μF, C = 100 nF, $R = 220\,\Omega$ are used, but R_p is not specified. Rather, R_p depends on the properties of the transistor switches to

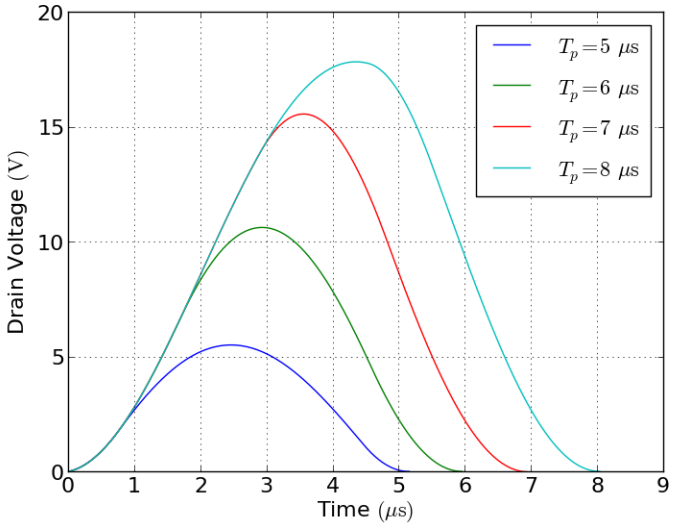

Figure 4.4: The new algorithm described in this section can be used so solve the switching times for decreasing resonant modulator periods at the expense of peak voltage.

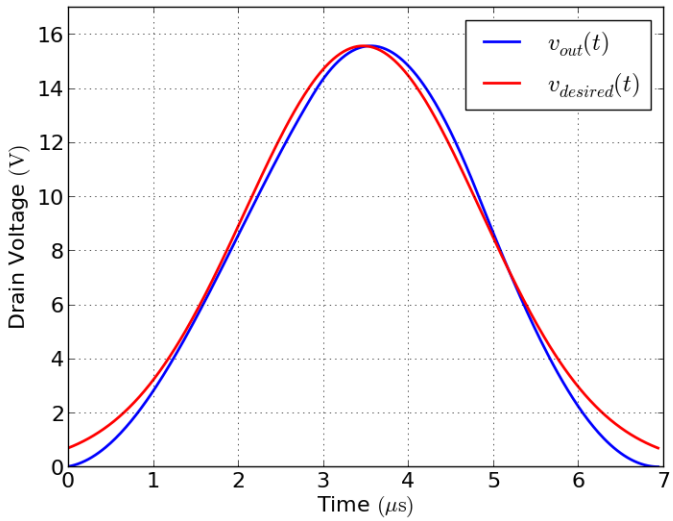

Figure 4.5: A comparison of v_{out} and $v_{desired}$ for the 7 μs pulse.

account for the losses. The losses of the inductor and capacitor are not included in this simulation because real components were not selected at this point in the design. Thus, the parasitic values of the passive elements were still unknown. The transistor model is a Spice model for a NDF08N60ZG

Table 4.1: Ideal Switching Times for Pulses in Fig. 4.4

T_p (μs)	t_1 (μs)	t_2 (μs)	t_3 (μs)	Error
5.0	0.8	4.5	5.2	$\epsilon_{mod} = 16.3\%$
6.0	1.7	4.6	6.0	$\epsilon_{mod} = 6.8\%$
7.0	2.9	4.8	6.9	$\epsilon_{mod} = 5.6\%$
8.0	4.5	5.5	8.0	$\epsilon_{mod} = 7.8\%$

Power MOSFET, the same device used for the fabricated circuit mentioned shortly. The first simulation is for a 7 μs pulse and uses the results of the previous section where $t_1 = 2.78\,\mu$s, $t_2 = 4.78\,\mu$s, and $t_{end} = 7.14\,\mu$s. The result in Figure 4.7 shows that these times do not result in the desired pulse shape, although it is close.

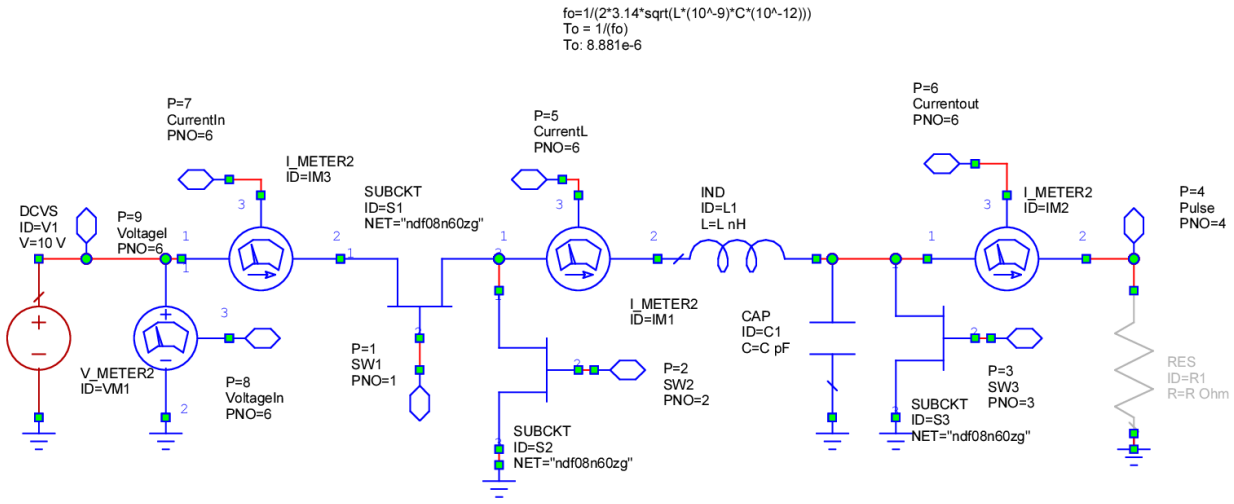

Figure 4.6: The schematic of the resonant modulator used in the AWR circuit simulator.

The waveform in Figure 4.7 never returns to zero until the circuit is in State (3). The fact that the voltage is too high at t_{end} means the circuit was not in State (2) long enough. The same figure also shows how the waveform changes when the switching times are adjusted, in this case to $t_1 = 2.78\,\mu$s, $t_2 = 5.08\,\mu$s, and $t_{end} = 6.78\,\mu$s. This difference may be explained by the fact that the estimate of the switch R_p does not match the true value in Spice simulations.

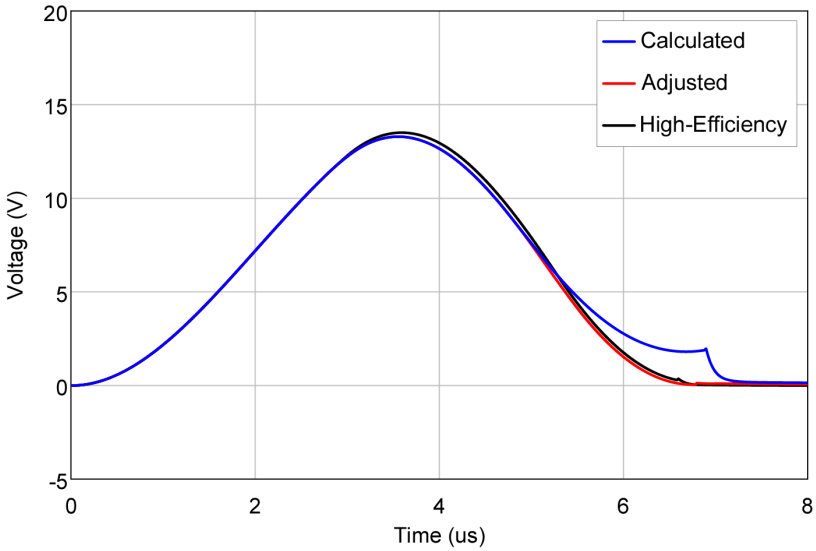

Figure 4.7: The resulting $v_{dd}(t)$ waveform for a resonant modulator simulated in AWR with Spice switch models. The non-ideal characteristics of the switches change the output waveform shape, so the switching times are adjusted to correct the shape. The black trace shows that the waveform shape can be preserved even when there is an off time between transitions when both S_1 and S_2 are off to avoid shorting the voltage source.

Simulating the circuit in VSS allows for the simulation of efficiency, measured as

$$\eta = \frac{\int_0^{T_p} v_{load}(t) i_{load}(t) dt}{\int_0^{T_p} v_{in}(t) i_{in}(t) dt}. \tag{4.13}$$

In the simulations, $v_{load}(t)$ and $i_{load}(t)$ are measured using pins 4 and 6, while $v_{in}(t)$ and $i_{in}(t)$ are measured using pins 8 and 7. A 250 ns delay was used when changing states states to account for turn-on and turn off-times of the switches and to prevent short-circuiting the supply. Simulations showed a modulator efficiency of 83.4% with the resulting waveform shown in Figure 4.7.

The modulator circuit was built and a picture is shown in Figure 4.8.[1] The modulator is designed with a Pulse P0841SNL 22 nH inductor and a variable capacitance that can switch

[1] The author would like to express great gratitude towards Maurico Pinto for building the circuit and assisting with measurements.

between 100 nF and 190 nF. This is included to further demonstrate how pulse width can be modified by the modulator with a digital signal. Measured results into a static 220 Ω load are shown in Figure 4.9 and summarized in Table 4.2. The measured efficiencies into the static load are lower than expected for a few reasons. First of all, the values of the inductor and capacitor give a Q-factor that causes a higher inductor current than necessary, thus increasing parasitic losses. By increasing the inductance and decreasing capacitance, these losses can be lowered. Additionally, the gate drivers are operated conservatively in these measurements so as not to break the part. This results in a lower gate voltage being applied to the switches and an increase in switch R_{on}, another place for power dissipation. Both of these issues are addressed in the next section and the resonant modulator is connected to a PA. With the design modifications and the PA as a load, the modulator efficiency increases to greater than 85%.

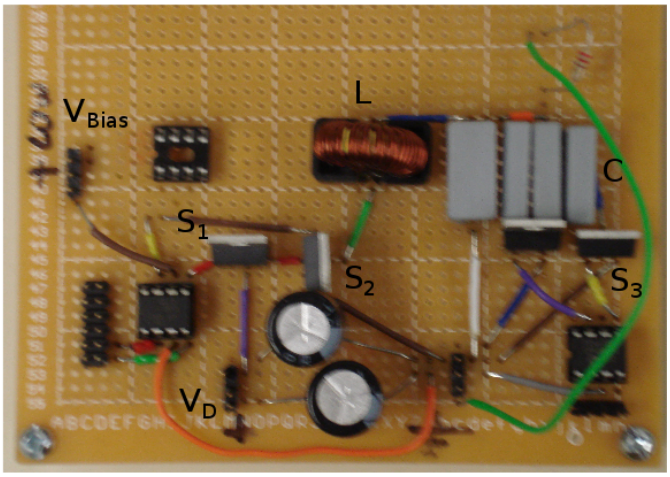

Figure 4.8: Photograph of the modulator circuit designed, built, and used for bench-top measurements. The modulator is designed with a NDF08N60ZG Power MOSFET, Pulse P0841SNL 22 nH inductor, and a variable capacitance that can switch between 100 nF and 190 nF.

4.3 Simulations and Measurements of a Supply Modulated MMIC PA

The resonant modulator is simulated in VSS with a 4-Watt GaN X-Band MMIC and measured. The CW characteristics of the MMIC PA are published in [15]. The simulated and measured

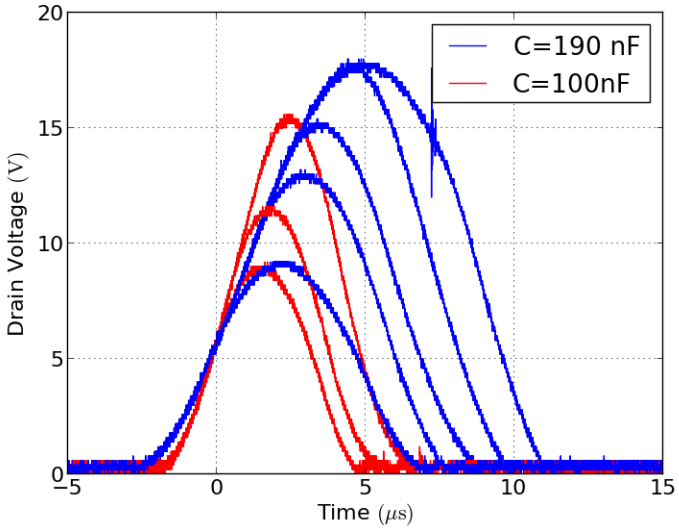

Figure 4.9: The modulator was tested in two configurations into a static load. The measurements demonstrate that by varying the capacitance and switching times, variable pulse widths and amplitudes can be experienced with hardware.

Table 4.2: Summary of Modulator Measurements with $R = 220\,\Omega$

T_p (μs)	Measured T_p (μs)	Capacitance (nF)	Peak Voltage (V)	Efficiency	Error
7.0	6.9	100	9.2	51.2%	$\epsilon_{mod} = 10.3\%$
8.0	8.0	100	11.6	57.3%	$\epsilon_{mod} = 10.0\%$
9.0	9.1	100	15.6	64.1%	$\epsilon_{mod} = 9.8\%$
10.0	9.9	190	9.4	40.8%	$\epsilon_{mod} = 15.8\%$
11.0	10.6	190	13.2	45.8%	$\epsilon_{mod} = 6.8\%$
12.0	12.1	190	15.4	52.4%	$\epsilon_{mod} = 5.2\%$
13.0	13.0	190	18.0	59.3%	$\epsilon_{mod} = 9.4\%$
14.0	14.0	190	18.0	55.2%	$\epsilon_{mod} = 13.2\%$

results of this PA are shown in Figure 4.11. The peak PAE is 50.8% at 35.2 dBm output power. The peak gain is 11.2 dB and the gain is 9.5 dB at peak efficiency. The supply-modulated PA was simulated in a method similar to the simulations in Chapter 3. VSS is used to simulate the combination of the PA and resonant supply modulator circuit using the circuit envelope simulator.

The PA is simulated in two configurations: amplifying a Gaussian LFM with a constant bias and amplifying it with the resonant modulator. The constant bias simulations applies an 8 μs

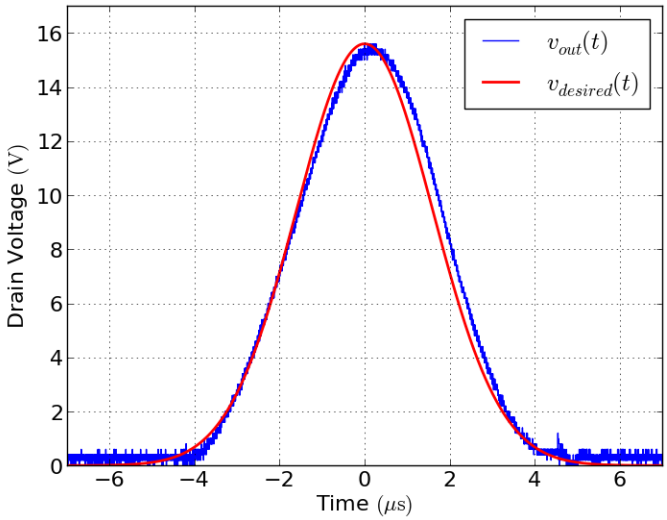

Figure 4.10: A comparison of v_{out} and $v_{desired}$ for the 9 μs pulse.

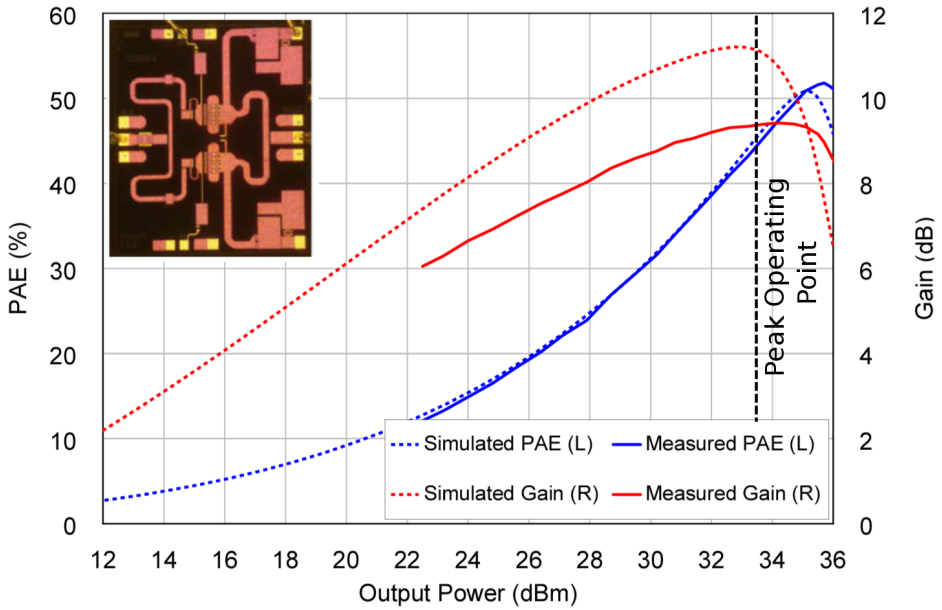

Figure 4.11: Simulated and meausured output power sweep for 4-Watt MMIC PA used in simulation and measurement. The peak PAE is 50.8% at 35.2 dBm output power. The peak gain is 11.2 dB and the gain is 9.5 dB at peak efficiency.

Gaussian pulsed LFM with 5 MHz of bandwidth to the PA input. In both simulations we try to achieve a peak pulse power of 33.5 dBm because this is the location of peak gain, so we are not compressing the amplifier. To quantify the "Gaussianess" of the RF outputs, the following metric is used to measure the error

$$\epsilon = \sqrt{\frac{\int_0^{T_Pulse} |v_{load-RF}(t) - v_{desired}(t)|^2 dt}{\int_0^{T_Pulse} |v_{desired}(t)|^2 dt}} * 100 \tag{4.14}$$

where $v_{load-RF}(t)$ is the complex RF PA load voltage, and $v_{desired}(t)$ is the desired load voltage. The constant bias simulation achieves an $\epsilon = 11.8\%$ without any pre-distortion. The supply-modulated simulations are done in two steps. First, a rectangular LFM is applied to the input of the PA with the resonant modulator modulating the drain voltage. The modulator also has a pulse width of 8 μs and is used to shape the output of the PA. The resulting waveform, shown in Figure 4.12(a), has an $\epsilon = 65.8\%$, so pre-distortion is needed. To pre-distort the wave, it is compared to the desired output wave and element wise division is used to solve the appropriate scaling factor, shown in Figure 4.12(b). This scaling factor is then applied to the rectangular input wave to shape its envelope and improve the error to $\epsilon = 12.8\%$. The way error is defined gives a calculated indicator of large the difference is from the desired signal, but it does not say much about the performance of the waveform. What matters for the desired waveform is how much the spectrum of the pulse changes as a result of the errors and if there are any time side lobes when the matched filter is applied. We show later that errors on the order of $\epsilon = 10\%$ result in a spectrum that still fits inside RSEC, and time side lobes 30 dB below the main lobe of the matched filter response.

The magnitudes of the RF PA load voltages are shown in Figure 4.13 for the constant-supply PA and supply-modulated PA, after pre-distortion. Both are compared to the desired output waveform. Figure 4.14 shows the output spectra of the amplified signals. The spectra of the amplified signals are broader than the desired spectrum, but do not have side-lobes and have properties that would comply with the regulations of Figure 2.1. The modulated PA does have higher out-of-band emissions than the constant bias case, but they are 70 dB below the peak power.

The results from simulations are summarized in Table 4.3. Use of the resonant modulator

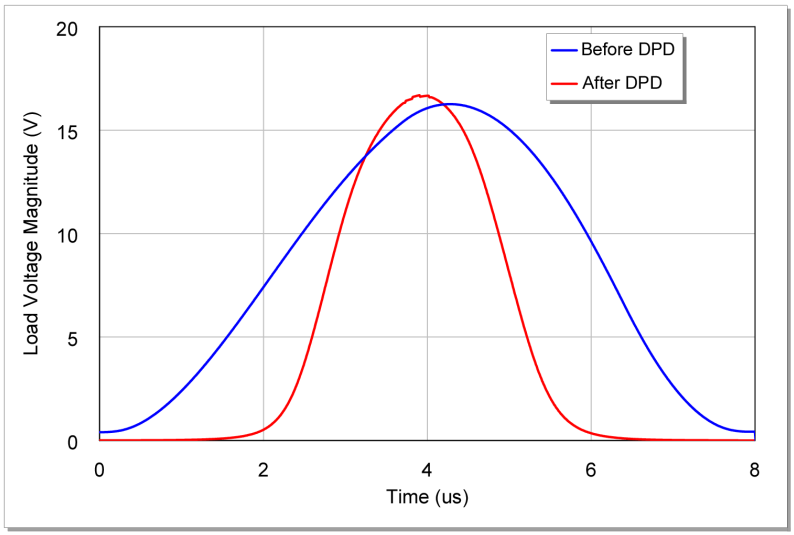

(a)

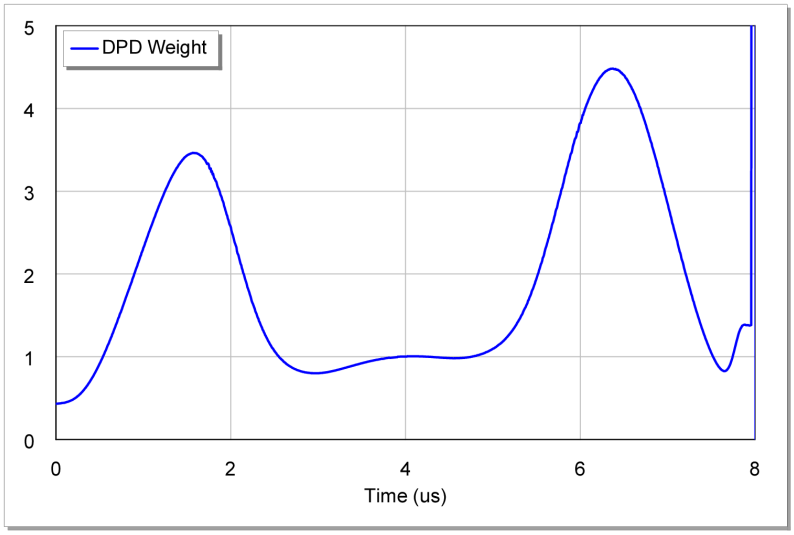

(b)

Figure 4.12: (a)The RF PA load voltage magnitude for both before and after DPD is applied. (b) The amplitude weighting applied to the rectangular input pulse to implement DPD.

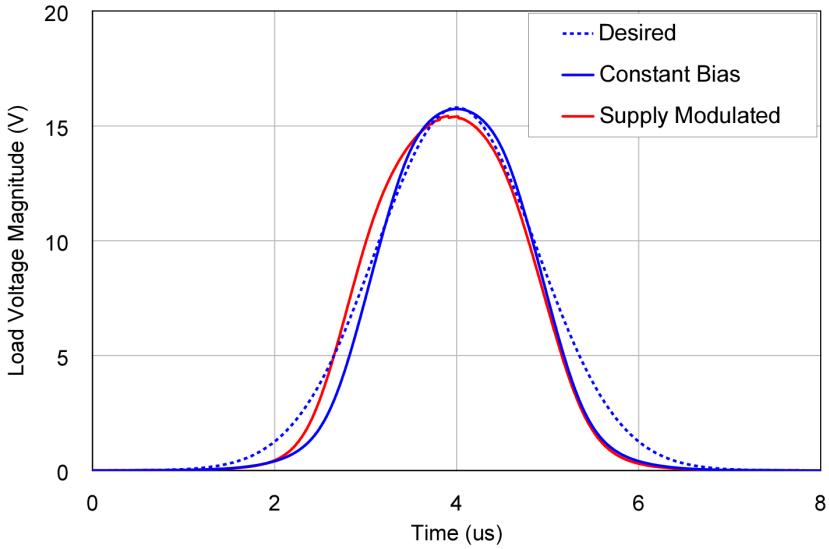

Figure 4.13: Simulations show that a near Gaussian shape can be achieved at the output of the PA for a constant bias and Gaussian LFM, or a pre-distorted rectangular LFM.

provided an increase of 10 points in efficiency over a constant bias. The definitions for efficiencies quoted in Table 4.3 are

$$PAE = \frac{\int_0^{T_p} |v_{load-RF}(t)|^2 - |v_{in-RF}(t)|^2 dt}{100 \int_0^{T_p} v_{drain}(t) i_{drain}(t) dt} \tag{4.15}$$

and

$$CPAE = \frac{\int_0^{T_p} |v_{load-RF}(t)|^2 - |v_{in-RF}(t)|^2 dt}{100 V_{dd} \int_0^{T_p} i_{supply}(t) dt} \tag{4.16}$$

where $v_{in-RF}(t)$ is the voltage at the input to the PA, $v_{drain}(t)$ and $i_{drain}(t)$ are measured at the drain of the PA, and V_{dd} and $i_{supply}(t)$ are measured at the input to the supply modulator. CPAE includes the losses of the modulator for the supply-modulated case, and is the same as PAE for constant bias since there is no modulator. These measurements are lower than the theoretical limits shown in Chapter 2 for two reasons: (1) the maximum efficiency at the output power we are targeting are only 45% instead of the 78% of an ideal Class-B amplifier. (2) The simulator

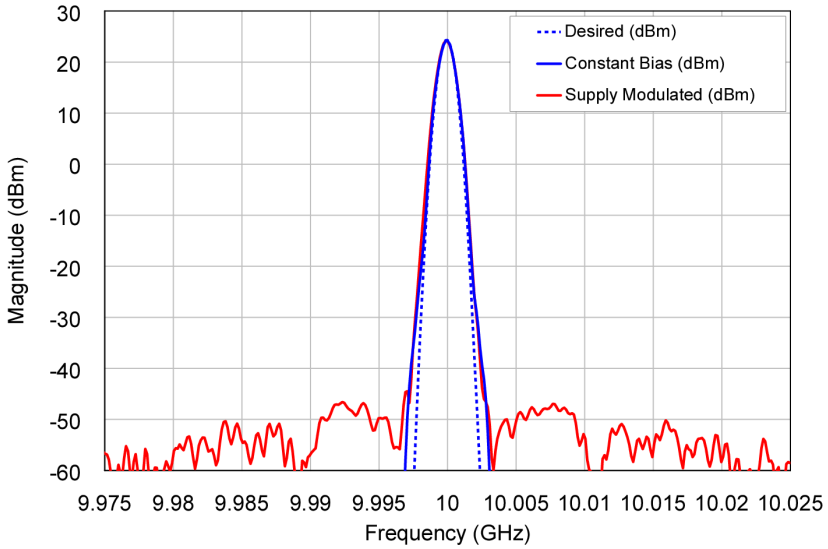

Figure 4.14: The spectra of the Gaussian LFM for a constant bias and modulated bias. Both cases make the spectrum slightly broader, but still operate without side-lobes. The modulated case has out-of-band spurious emissions due to higher non-linearities in the system, but they are 70 dB below the peak power.

produces errors for low power signals which increase the DC power consumption. We are currently working with the AWR team to resolve the second issue.

Measurements are performed with the same PA used in simulations and the modulator described in the Section 4.2 is used for drain modulation. The efficiency results demonstrated in the previous section for a static load are lower than desired, so modifications are made to the modulator to improve it. First of all, the inductance is increased to 44 μH and capacitance decreased to 30 nF so that the Q-factor is lower, thus raising efficiency. Additionally, the pulsed gate voltage for the switches is increased to the maximum available from the driver chips. This decreases the R_{on} of the FET switches. A measurement of the modulator efficiency is performed with the PA as a load and pulsed LFM inputs. The voltage and current between the modulator and PA are measured on an oscilloscope with a voltage and current probe. The measured input and output powers are shown

Table 4.3: Summary of Resonant-Modulated PA Simulaitons

	Constant Bias	Supply-Modulated
P_{max}	34.1 dBm	34.4 dBm
Average Pulse Power	420 mW	470 mW
Average Drain Pulse Power	1830 mW	1260 mW
PAE	21%	33%
CPAE	21%	30%
Error	$\epsilon = 11.8\%$	$\epsilon = 12.8\%$

in Figure 4.15. The efficiency achieved in this measurement when modulating a PA was 92%.

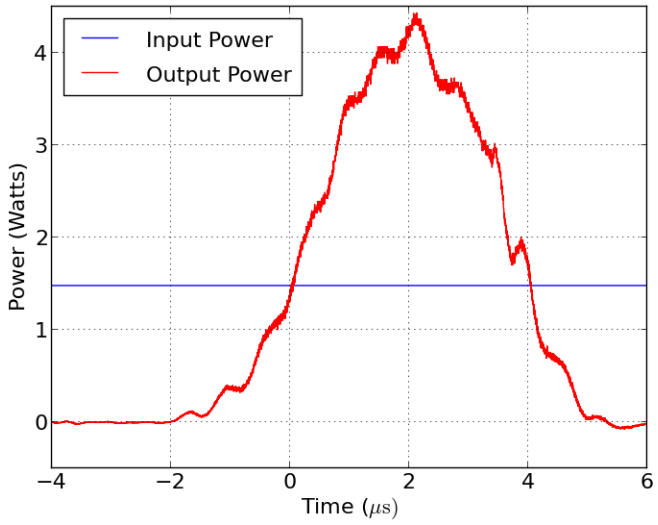

Figure 4.15: Measurement of the input and output power of the supply modulator when connected to a PA with a pulsed Gaussian LFM waveform. With the PA as a load, the modulator demonstrates 92% average efficiency for this measurement. It is not possible to plot instantaneous efficiency due to the pulsed nature of this measurement and the multiple storage devices present in the circuit. The negative times correspond to the trigger used on the oscilloscope. Thus, the pulse at $t = 0$ is the one which triggered the oscilloscope.

Supply-modulated measurements of the PA are performed with the MMIC PA used in simulations and the resonant modulator described in the previous section. A comparison is made between the PA when operated with a constant bias and supply modulation for a 9 μs Gaussian pulse with 5 MHz of LFM bandwidth and a duty cycle of 10%. The amplifier is operated such that the peak output power of the Gaussian pulse is about 32.5 dBm. This output power is chosen because it is

the limit of the amplifier linear operation. If the amplifier is driven any harder, the top of the pulse would flatten and not give the Gaussian shape. As a result, very little pre-distortion is needed in both cases. To pre-distort that amplifier, a Gaussian pulse with few standard deviations ($3\,\sigma$) was applied to the input of the PA. When this is done, the energies at the edges of the pulse are higher and compensates for the decreased gain of the PA in these backed-off regions. Figure 4.16 shows the output pulses from the constant bias and supply-modulated PA. When compared to the desired pulse with four standard deviations, both test cases have similar shape. The spectra of the two test cases are shown in Figure 4.17 and they have the desirable spectral properties that conform with NTIA requirements.

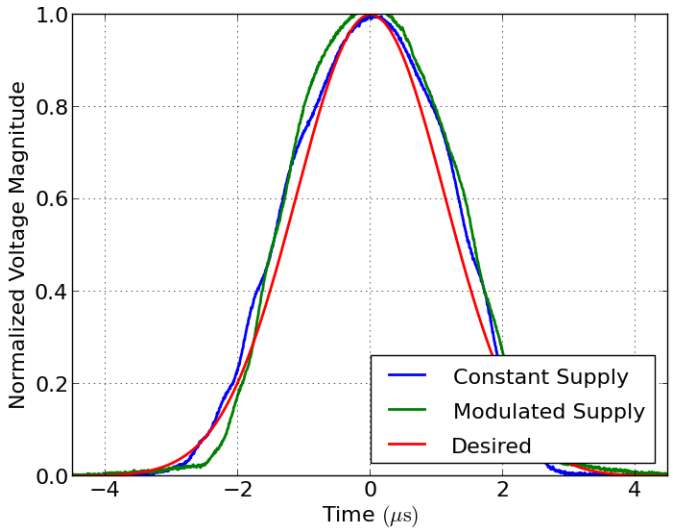

Figure 4.16: A comparison of the voltage magnitude for the measured Gaussian pulses. The constant bias pulse has an error of $\epsilon = 10\%$ and the supply-modulated pulse has an error of $\epsilon = 12\%$.

The time-domain waveform of the supply-modulated PA is shown inf Figure 4.18 and the matched filter response for this waveform is shown in Figure 4.19. This pulse has a range resolution of 80 m. More LFM bandwidth could be used to reduce range resolution. Measurements are not made with larger values of β, but this is only limited by the PA RF bandwidth, which is about 500 MHz. The time side-lobes of the matched filter response are 29 dB below the maximum response.

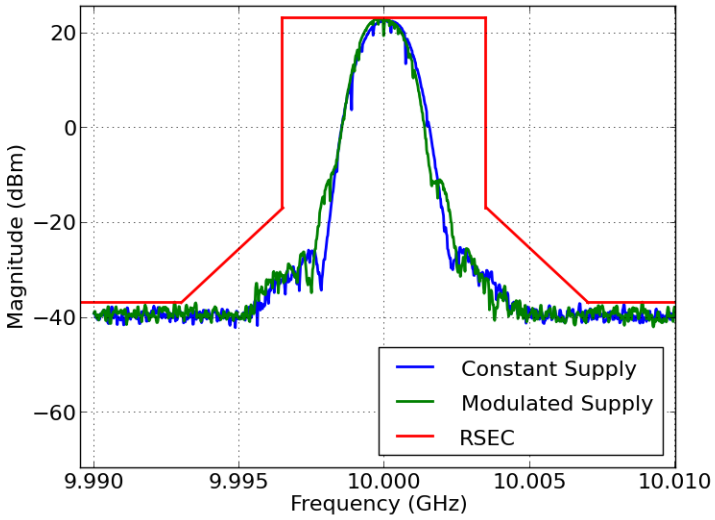

Figure 4.17: Measured spectra of the constant bias and supply-modulated PA. The supply-modulated PA has narrow side-lobes 30 dB below peak power, but they both fit within the NTIA RSEC for a 9 μs, unmodulated rectangular pulse. One should note that a rectangular pulse with equivalent energy (9 μs) would have an even wider RSEC. Also, the RSEC becomes more lenient if phase modulation is included in the definition. Clearly, $G_\beta(t)$ has no issues complying with the most stringent of RSEC.

This shows 14 dB improvement over the time side lobes of $R_\beta(t)$.

A summary of the efficiency measurements are shown in Table 4.4. The instantaneous drain efficiency is shown in Figure 4.20, but is somewhat misleading because it becomes negative when the current flows from the PA to the supply modulator. For this reason, it is helpful to look at the instantaneous drain power and PA power dissipation as well, which are shown in Figure 4.21. As in the case of simulations, this is lower than the theoretical limits derived in Chapter 2, but is to be expected because the maximum PAE is lower than that of an ideal Class-B amplifier. The drain voltages and currents are shown in Figures 4.22.

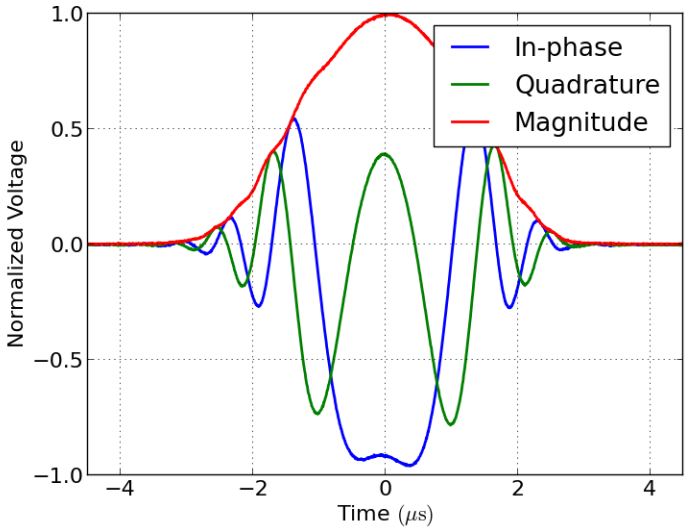

Figure 4.18: The measured time-domain waveform of the supply-modulated PA. The 9 μs pulse has 5 MHz of LFM bandwidth and contains four standard deviations.

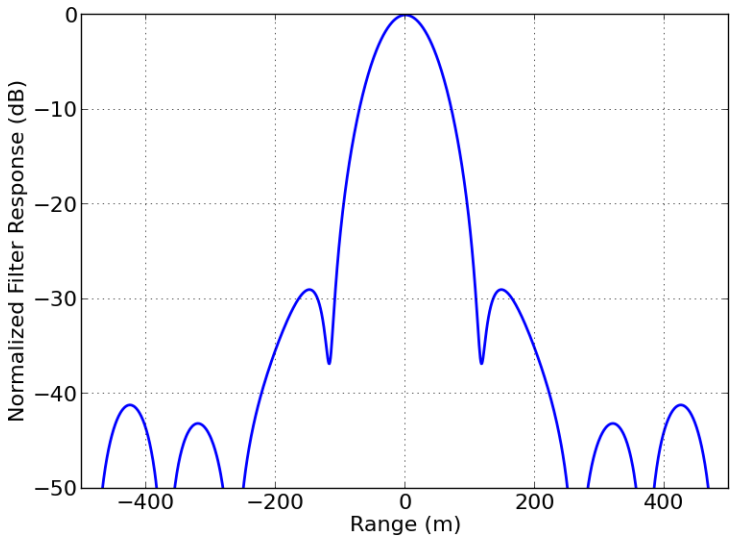

Figure 4.19: Matched filter response of supply-modulated PA. This particular pulse has a range resolution of 80 m, but more bandwidth could be used to improve upon this. The time side-lobes are 29 dB below the maximum.

Table 4.4: Summary of Resonant-Modulated PA Measurements

	Constant Bias	Supply-Modulated
P_{max}	32.5 dBm	32.7 dBm
Average Pulse Power	450 mW	470 mW
Average Drain Pulse Power	1170 mW	1040 mW
PAE	34%	40%
CPAE	31%	36%
Error	$\epsilon = 10\%$	$\epsilon = 12\%$

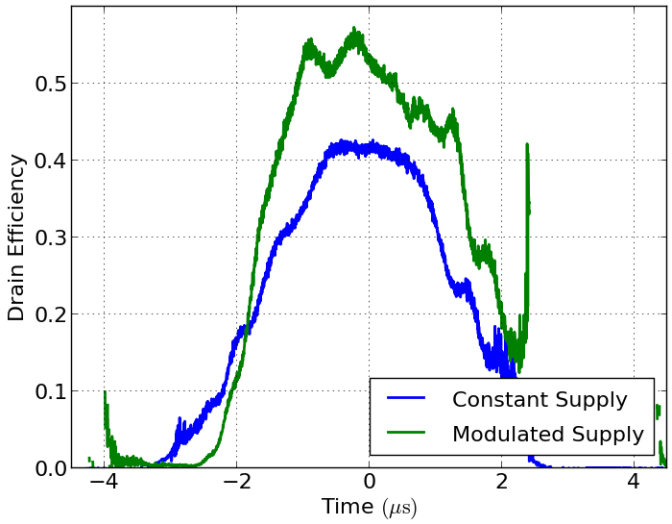

Figure 4.20: The measured drain efficiency of the two configurations.

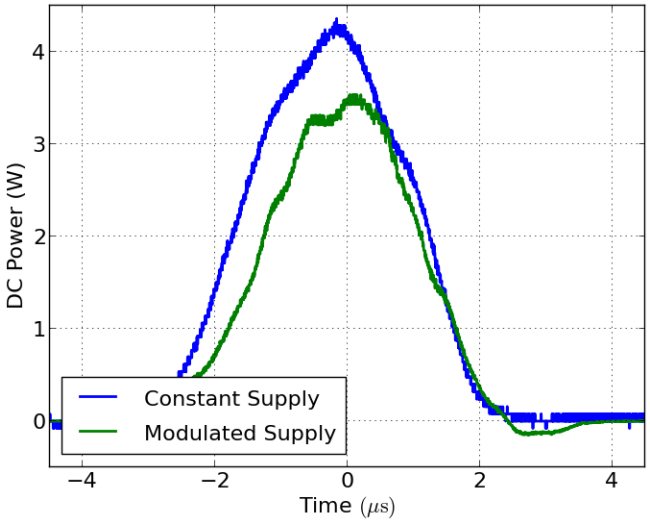

(a)

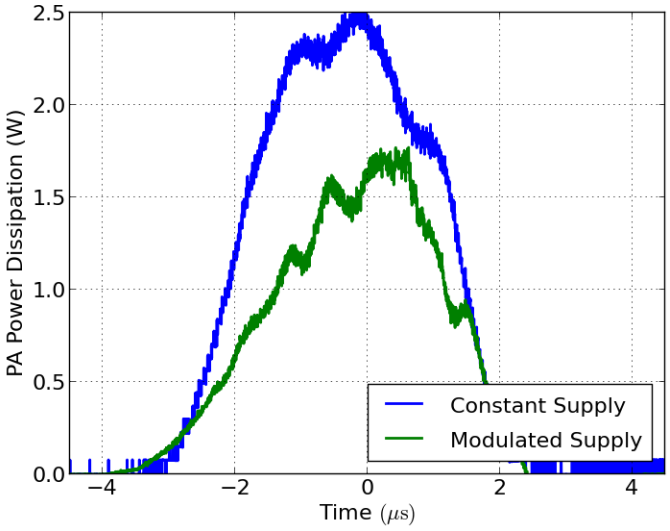

(b)

Figure 4.21: (a)The measured drain power of the constant bias and supply-modulated PA. (b) The calculated power dissipated by the PA.

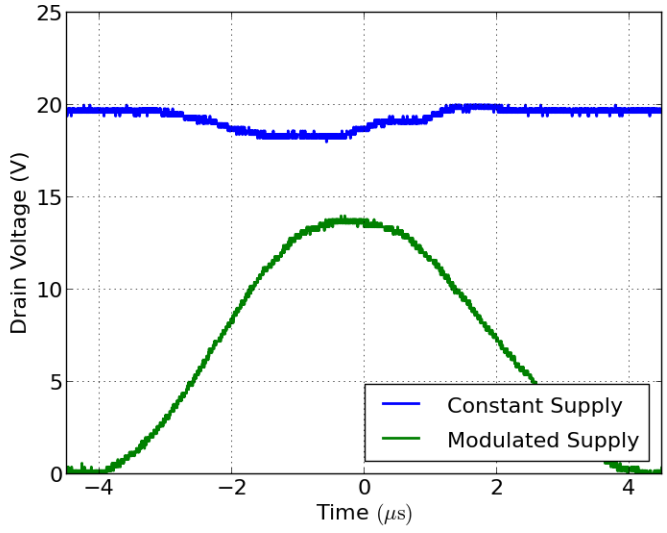

(a)

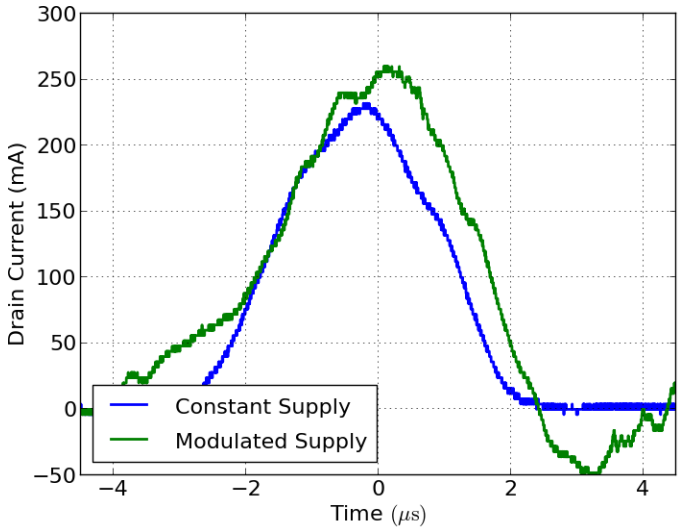

(b)

Figure 4.22: The measured (a) drain voltages and (b) drain currents for the two test cases. There is a dip in the constant bias PAs drain voltage because it is biased by a non-ideal voltage source. The dip is a result of the quick current draw of the PA discharging the power supply's decoupling capacitor.

Chapter 5

Multi-Mode Radar Enabled by Supply-Modulated Power Amplifiers

5.1 Problem Description

There is an interest in a more flexible radar that is able to operate in various power and pulse shape modes, an example of which is depicted in Figure 5.1. Mode 1 is the standard constant-amplitude pulse mode with frequency modulation for improved range resolution. The pulse widths can be adjusted, but the period should also change to maintain a constant average power so that it presents a stable load for the power supply. The peak power of this mode is constant and it is useful to optimize the PA for maximum efficiency at this point since there is no amplitude modulation for this mode. Mode 2 uses shaped pulses so that radar has reasonable spectral characteristics. Additionally, this mode should have variable peak power from pulse to pulse. This feature is useful for clutter rejection algorithms and maximization of radar resources. Mode 3 is the same as Mode 2, except that the peak power is much higher. This allows for the radar to have enhanced capabilities, albeit for a short period of time. The reasoning for this mode is that radars are typically designed for the worst case scenario, which may be very costly. If a radar were designed with this capability and it were used only a small amount of the time, then there could potentially be a large cost savings.

A possible approach to solving the problem is to use a Doherty amplifier and a resonant modulator. In Chapter 1, it was stated that the original Doherty uses two amplifiers to achieve a high backed-off efficiency from peak power with an efficiency versus power characteristic similar to the drawing in Figure 5.2. This efficiency profile lends itself naturally to the three-mode problem

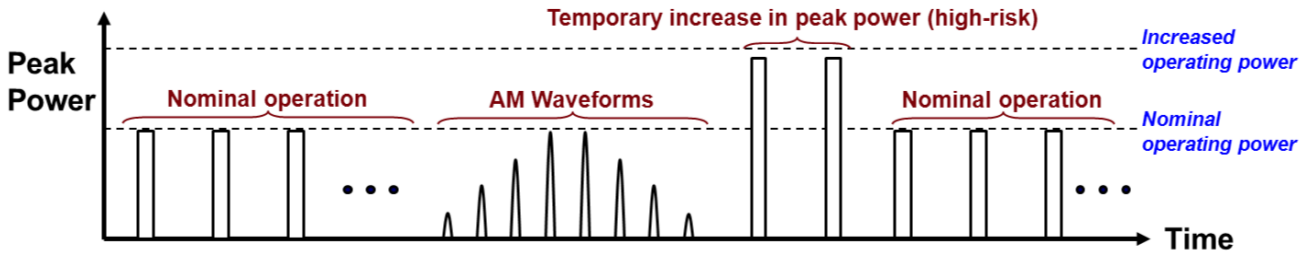

Figure 5.1: Summary of desired three-mode operation. Mode 1 is the normal radar mode with a constant peak and average power rectangular pulses. Mode 2 uses shaped pulses and variable peak power pulse to pulse. Mode 3 uses a higher peak power, but is not used often.

because it can be operated at high efficiency in Mode 1 without dissipating any power in the peaking amplifier because it is off. The peaking amplifier is only turned on when the amplifier is driven hard enough in Mode 3, but will still be efficient because of the load modulation between the peaking and carrier amplifiers. It was shown in Chapter 2 that the shaped pulses desired in Mode 2 will have lower efficiency. To mitigate this, we propose that a resonant supply modulator be used for Mode 2 operation. This chapter discusses the design and simulations of an X-Band Doherty GaN MMIC to be used for this application.

5.2 Design of the Doherty MMIC PA

To our knowledge, there has only been one attempt at an X-Band MMIC PA [63][64], but the design is done in GaAs. They reported simulated results of 31 dBm peak output power with greater than 50% efficiency and 33% efficiency at 6 dB output power back off. Our 4-Watt X-Band Doherty MMIC is designed in the TriQuint 0.15 μm GaN process. Modelithics non-linear models for a $8 \times 100\,\mu$m device (TXTX_3MI15GaN) are used.

Stability is a main concern for this design since it has two parallel transistors which load pull each other. For this reason, the first step in designing the PA is to design gate-bias networks which provide unconditional stability across all frequencies while maintaining gain. The schematic used to tune the stabilizing and biasing circuitry is shown in Figure 5.3. The bias tee consists

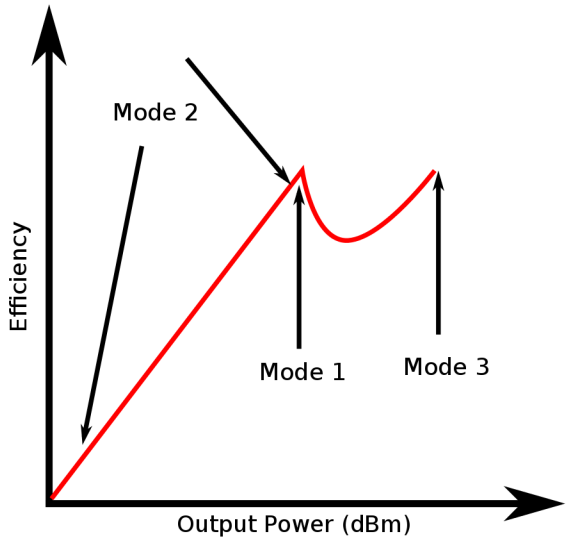

Figure 5.2: The approach to operate the three-mode radar is to use a supply-modulated Doherty. Mode 1 is operated at the first peak in the efficiency curve when only the carrier amplifier is turned on. Mode 3 utilizes the additional power of the peaking for the increase in peak power. The load modulation in Mode 3 ensures high efficiency. Mode 2 is operated in the backed-off region from the first efficiency peak. Here, a resonant modulator is used to increase efficiency.

of a quarter-wave transmission line choke and a blocking capacitor, which must be large enough to be an almost short at X-Band. The stabilizing components are the bypass capacitor at the biasing source, the resistor in the bias path, and the RC-circuit in series with the gate. The bypass capacitor and gate biasing resistor are standard stability techniques and the RC-circuit at the gate is meant to attenuate low frequency signals while passing X-Band frequencies. The result of this stabilization is shown in Figure 5.4 where a linear stability analysis is done. Results show that the K-factor is greater than one for all frequencies, thus ensuring small-signal stability, while gain at the design frequency is maintained. Although small-signal stability of both devices is not sufficient to ensure full-system, large-signal stability, it helps to give confidence that stability will be maintained. Further stability analysis is explained below.

A simulated load-pull is performed with harmonic balance simulation to plot the PAE and output power contours. Load-pull is performed on two devices: a $8 \times 80\,\mu$m device for the carrier amplifier and a $8 \times 100\,\mu$m device for the peaking. The optimal impedance for PAE of both devices

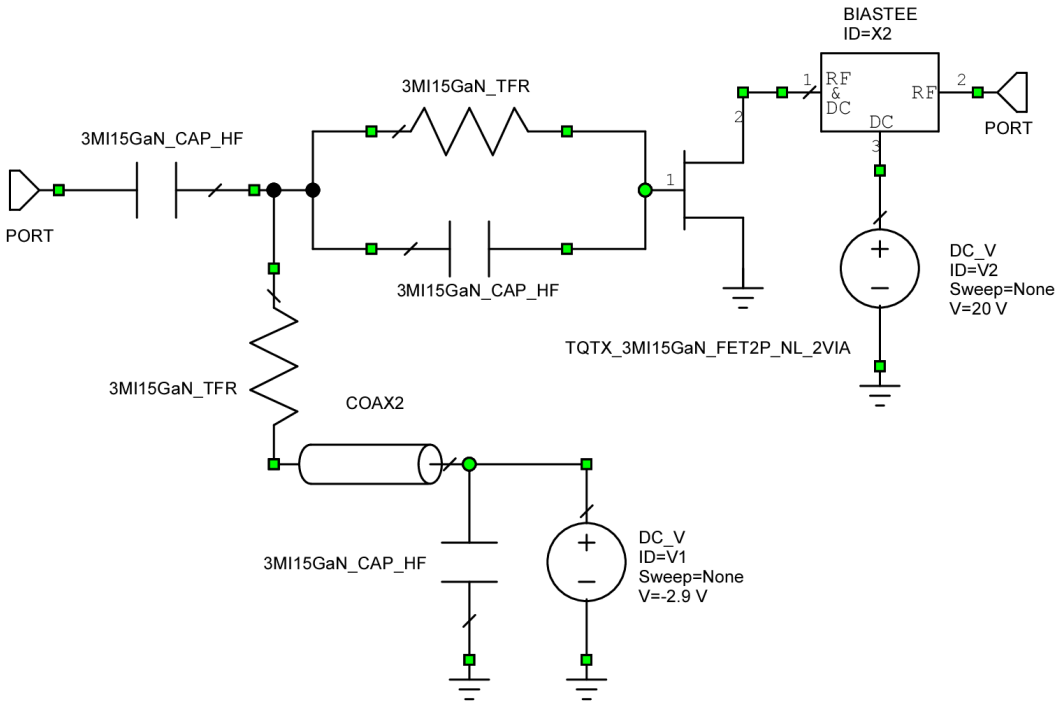

Figure 5.3: A schematic of the gate-biasing and stabilizing circuitry. Linear simulations are done of the circuit so that passive values could be tuned to provide unconditional stability while maintaining gain.

has large inductive components. However, the carrier and peaking amplifiers of the Doherty need to be matched into real loads. Short-circuited stubs are placed on the RF-only side of the blocking capacitor to resonate out the inductive portion of the optimal load. Load-pull results are shown in Figure 5.5 with the gate-stabilizing circuitry and resonant stub present. Simulation results show that the carrier-amplifier device has an optimal PAE load value of about $100\,\Omega$ as does the larger device. We decided to design for maximum efficiency instead of output power, so $100\,\Omega$ is the target load impedance for the carrier and peaking amplifiers when operating at maximum power for the full Doherty PA. For this load impedance, both amplifiers have a PAE=57% and output powers of 33 dBm and 34 dBm for the carrier and peaking amplifier respectively.

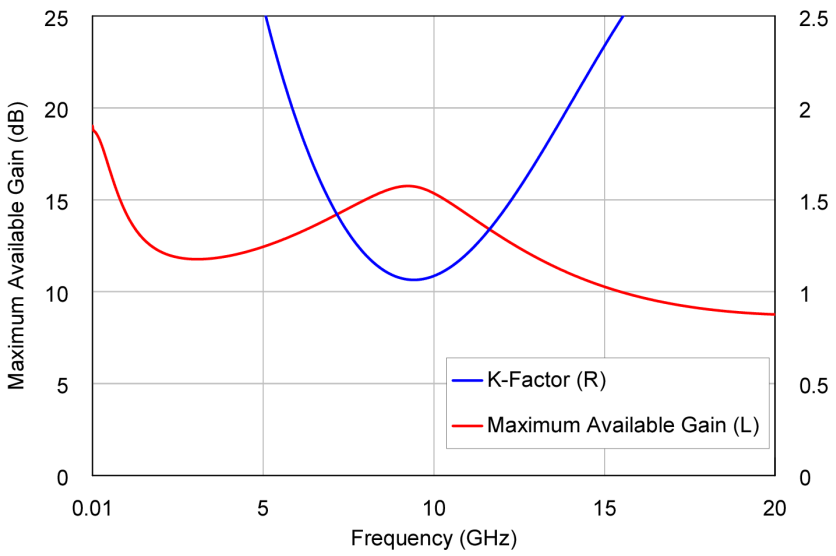

Figure 5.4: Small-signal simulation shows that the stabilizing circuitry is able to ensure unconditional small-signal stability while maintaining a gain greater than 15 dB at the carrier frequency.

It was stated in Chapter 1 that analysis of the Doherty is normally performed assuming a $50\,\Omega$ characteristic impedance, i.e. $Z_0 = 50\,\Omega$ and $Z_L = 25\,\Omega$ in Figure 1.9. Since the optimal impedance from load pull simulations is $100\,\Omega$, we use this value for the Doherty characteristic impedance. This allows for less complexity and lower losses in matching circuitry. With the selection of $Z_0 = 100\,\Omega$, no matching is needed in Z_L or the outputs of the peaking and carrier amplifiers. The quarter-wave transformer presents a $200\,\Omega$ load to the carrier amplifier when the peaking amplifier is off and a $100\,\Omega$ load is presented to each amplifier when both are at full output power.

The bias-tee for the drains of the two amplifiers are designed to ensure low loss at the carrier frequency using a quarter-wave transmission line for the choke. A high-level schematic of the Doherty PA is shown in Figure 5.6. The carrier and peaking blocks contain the transistors, as well as their bias-tees, stabilizing circuits, and resonators. The carrier transformer is the quarter-wave $100\,\Omega$ line which transforms the $50\,\Omega$ load to $200\,\Omega$ when the peaking amplifier is off. The offset

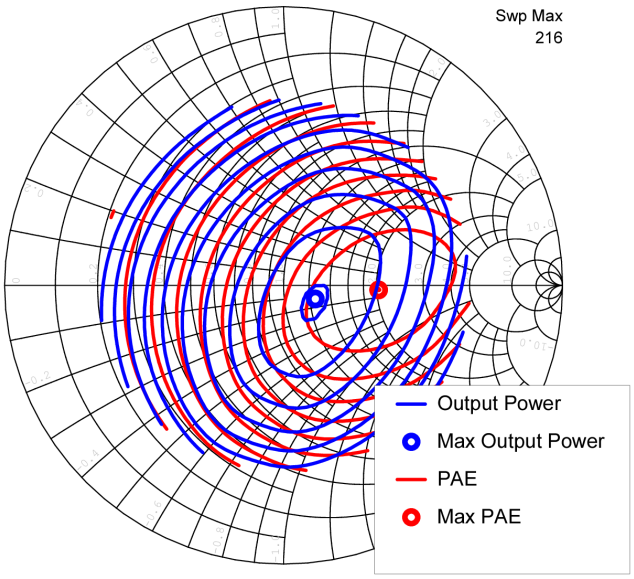

(a)

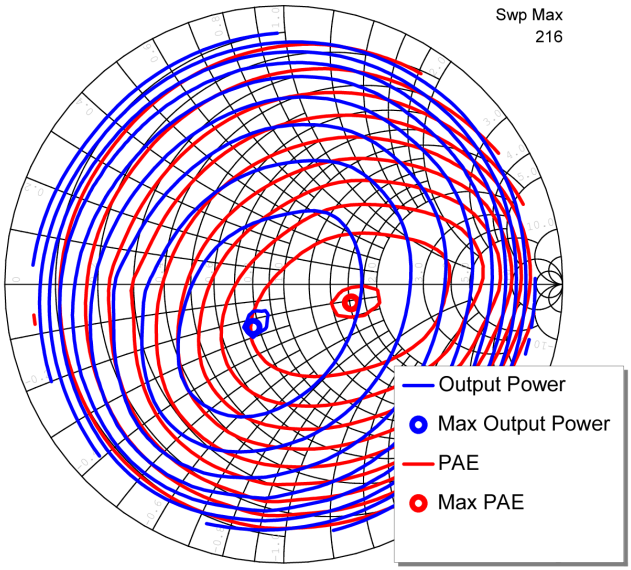

(b)

Figure 5.5: The simulated load-pull result for (a) the carrier amplifier and (b) peaking amplifier when a resonant stub is used to resonate out the inductive portion of the optimal load impedance.

line is to ensure the impedance looking into the output of the peaking amplifier is an open when

the amplifier is off. This is necessary because the peaking amplifier has a non-open impedance in reality and is not isolated from the carrier amplifier, so it must be transformed to an open so that it does not load the carrier when turned off. To ensure the carrier and peaking paths have the same delays, a line is inserted before the peaking amplifier which is a quarter-wave long minus the length of the offset line.

The circuit in Figure 5.6 is simulated with harmonic balance and values of lumped elements are tuned to optimize performance. The goal throughout the design process is to maintain greater than 50% PAE from 30-36 dBm output power. Once all values for lumped elements are chosen, we exchange simulated layout blocks for schematic blocks. The layout is done using the process development kit (PDK) in the layout editor and passively simulated using the AWR Axiem method of moments simulator. These simulated layout blocks systematically replace the schematic models of their associated circuitry one-by-one. Full simulation of the Doherty is repeated every time a new layout block is inserted to ensure the efficiency specification is being met; tuning of the layout block is performed in the cases when the specification is not met. This process is continued until the full layout is complete. A final simulation of the Doherty is shown in Figure 5.7. The design goal of 50% PAE from 30-36 dBm output power is not met in simulation, but 40% PAE is maintained across these power levels. The gain is flat in backed-off regions and is 9 dB whereas the gain in 7 dB when both the carrier and peaking amplifiers are on.

More than individual K-factors of the two amplifiers is needed for the stability analysis of this circuit. K-factor is only useful for a two-port, single stage circuit. Additionally, it only addresses linear instabilities. Since the Doherty uses two non-isolated amplifiers in parallel, we use the general feedback theorem [65] for additional stability analysis. In this method, a perturbation is injected into the circuit and the gain and phase of it in a loop are plotted, which is shown in Figure 5.8. As is the case with loop gain analysis, instability occurs when the gain is greater than unity for -180° of phase delay. The figure shows two regions with greater than unity gain which could be cause for concern: near 6 and 13 GHz. The phase delay in each of these regions is at least 20° greater or less than -180°, so we feel the circuit will be stable when fabricated.

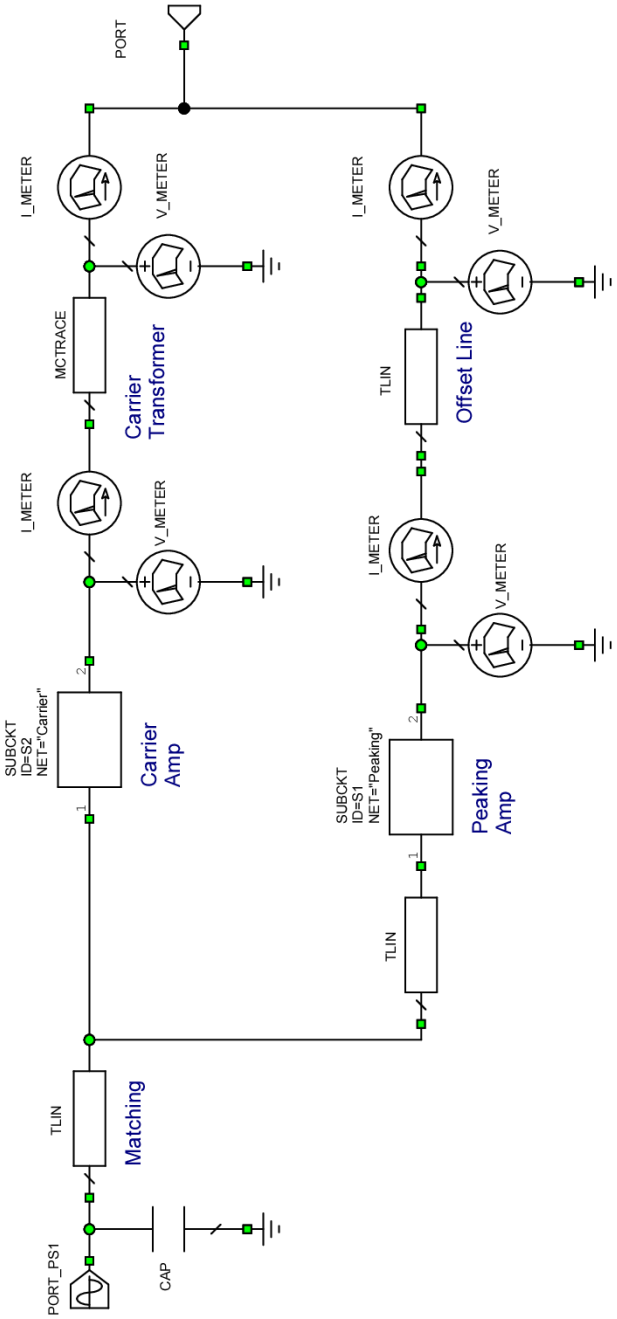

Figure 5.6: High level schematic of Doherty simulations. The carrier and peaking amplifiers contain the transistors, bias networks, stabilizing circuits, and resonators to match the devices into a real impedance. The transformer presents a 200 Ω load to the carrier amplifier at low power levels. The offset line ensures that the output of the peaking amplifier presents an open circuit at low power levels.

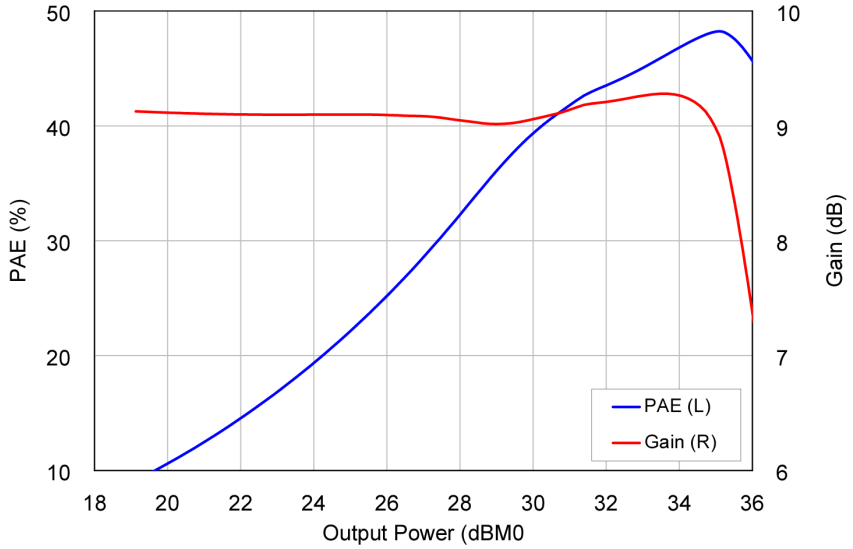

Figure 5.7: Efficiency and gain of the Doherty PA plotted against output power. 40% PAE is maintained across these power levels. The gain is flat in backed-off regions and is 9 dB whereas the gain in 7 dB when both the carrier and peaking amplifiers are on.

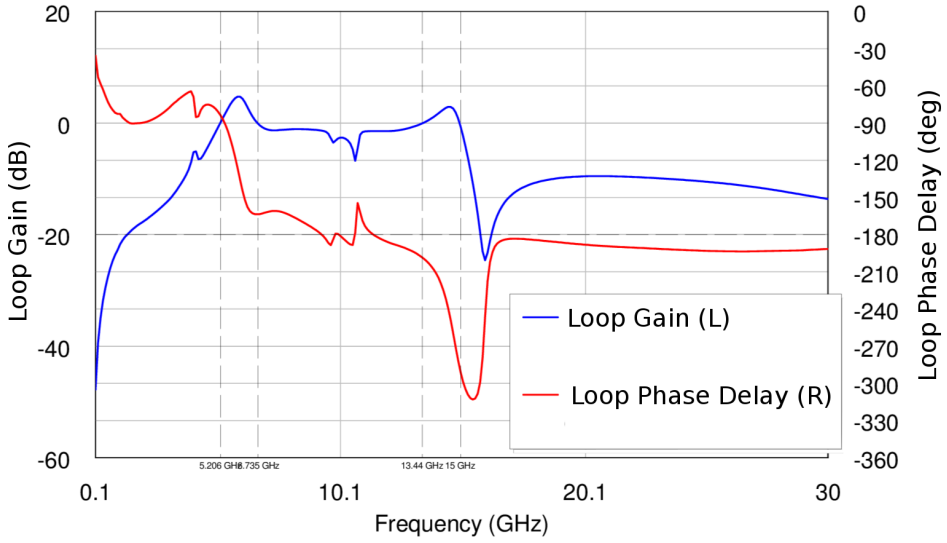

Figure 5.8: Stability analysis of the Doherty PA. The loop gain is greater than one only in the regions around 6 and 13 GHz while the loop phase delay in these regions is at least 20° greater or less than −180°, which indicates stable operation.

The X-band GaN Doherty PA MMIC is fabricated in the TriQuint 0.15 μm GaN foundry. An image of the MMIC is shown in Figure 5.9. The carrier amplifier is on the top and is connected to 100 Ω quarter-wave transformer. The peaking amplifier is on the bottom and is connected to the 100 Ω offset line. The input uses a non-isolated combiner with matching. Preliminary on-wafer measurements made by TriQuint are shown in Figure 5.10.

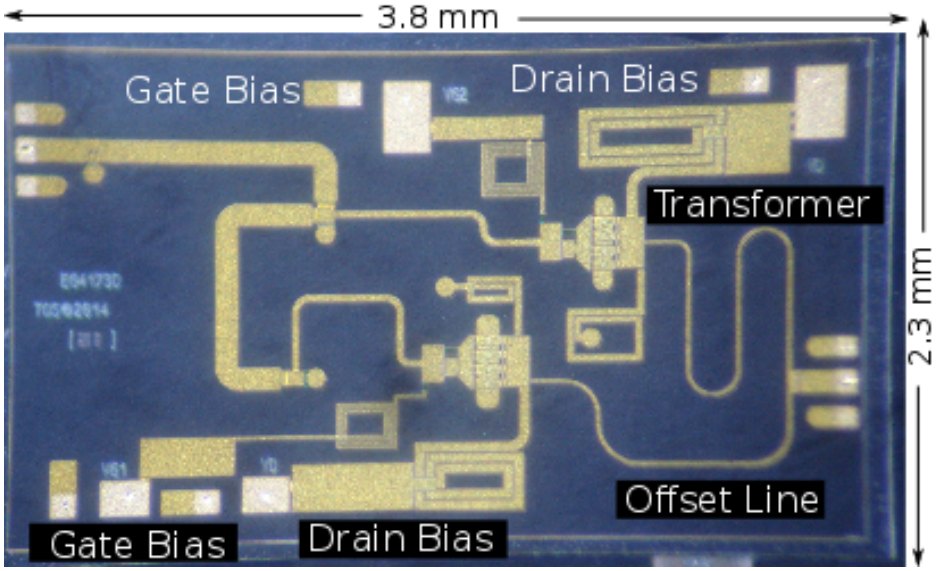

Figure 5.9: A photograph of the Doherty MMIC PA with he carrier amplifier is on the top and connected to 100 Ω quarter-wave transformer. The peaking amplifier is on the bottom and is connected to the 100 Ω offset line. The input uses a non-isolated combiner with matching.

The narrow-band circuit is designed to have a center frequency of 10 GHz. Measurements are made with a drain supply of 20 V, a carrier gate bias of -2.9 V, and peaking gate bias of -4.5 V. These are the values used in simulation but may not be the best choices for the fabricated circuit. We recommend that a sweep of gate bias levels around these selections be performed when further measurements are made of the circuit to find optimal bias levels. On-wafer measurements are made for input power levels of 10 dBm, 16 dBm, 22 dBm, and 28 dBm with gain, output power, and PAE measured at each point. The results of PAE measurements are shown in Figure 5.10 for the 78 best circuits from 3 separate wafers. The figure shows efficiency performance across 200 MHz of bandwidth, but measurements demonstrate similar efficiency and output power measurements

Table 5.1: Summary of Three-Mode Doherty Simulaitons

	Mode 1	Mode 2	Mode 3
PAE	27%	26%	39%
Peak Pulse Power	30.1 dB	30.0 dB	36.2 dB
Gain at Peak Pulse Power	9.2 dB	8.9 dB	7.2 dB

across 1 GHz of bandwidth. The best circuits are selected based on the criteria that they have a PAE of greater than 48% at the input power levels of 22 dBm and 28 dBm. Measurements confirm that the Doherty is able to maintain an efficiency of about 50 % across output powers varying by 5 dB. The gain measurements are shown in Figure 5.11 and demonstrate that the gain is not as consistent as efficiency across circuits. The backed-off gain varies from 8.5-10 dB while the compressed gain varies from 7-9 dB. Although we do not know of any other GaN Doherty MMIC designs at X-Band, results have be published at C-Band [66] and Ku-Band [67]. In [66], measurements demonstrated greater than 50% drain efficiency from 30-37 dBm. The authors of [67] did not present efficiency versus output power measurements, but demonstrated PAE=40% in two-tone tests with a peak output power of 25 dBm.

5.3 Three-Mode Radar Simulations

Simulations similar to those presented in Section 4.3 are performed on the X-Band GaN Doherty MMIC PA with the AWR VSS circuit envelope simulator. The simulation uses a 7 μs chirp with 14 MHz of bandwidth in the three modes of operation: at nominal power, resonant modulated, and at peak power. The RF load voltage magnitudes are shown in Figure 5.12 while the power and efficiency results are summarized in Table 5.1. The simulated efficiency results, calculated with (4.15), are about 10 points lower than expected, consistent with the results of Section 4.3. The results show that Mode 1 loses only 10 points of PAE when backed off 6 dB from Mode 3. Additionally, efficiency is preserved by a resonant modulator in Mode 2, compared to Mode 1, for a Gaussian pulse. The error of the Gaussian pulse, defined in (4.14), is $\epsilon = 8.6\%$.

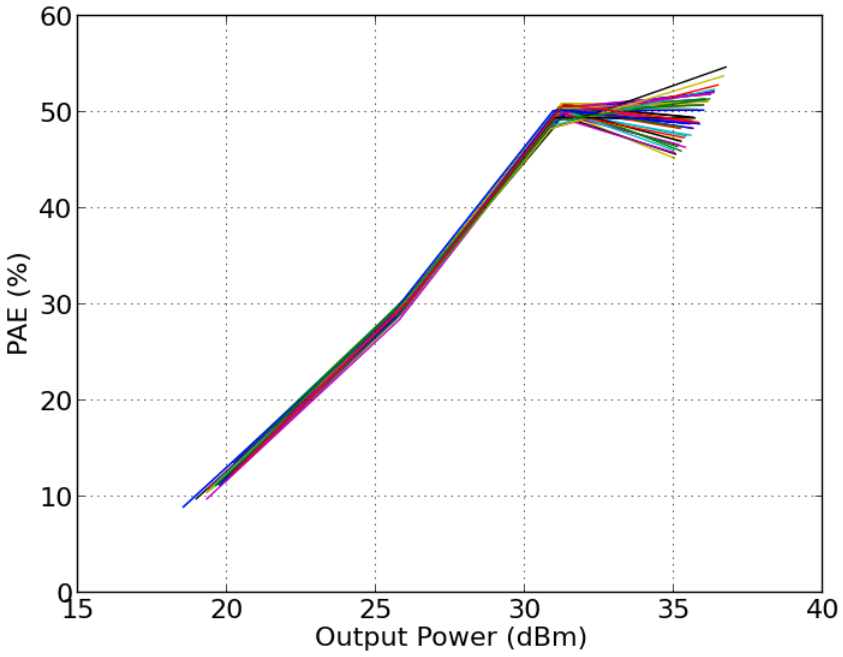

(a)

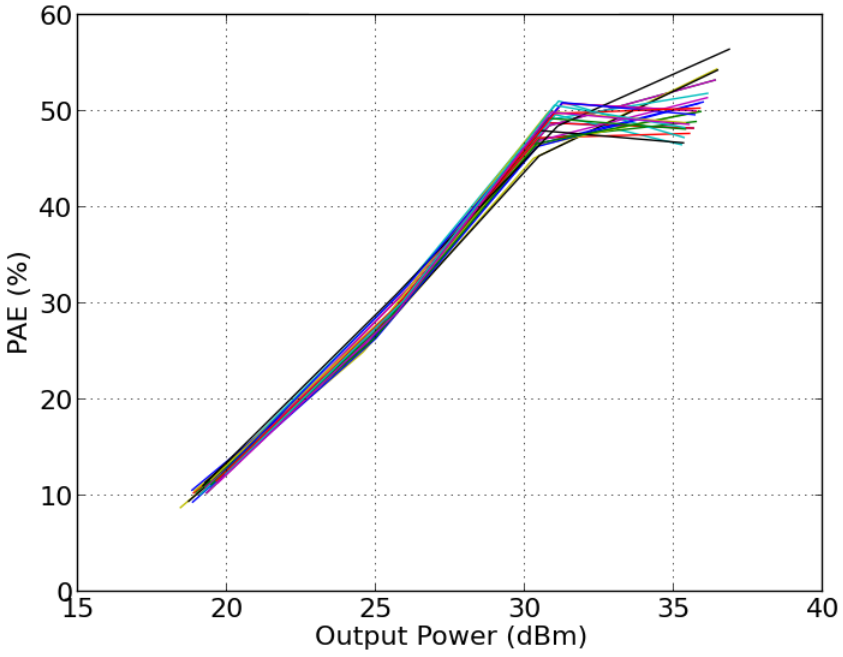

(b)

Figure 5.10: Measured PAE results at (a) 9.9 GHz and (b) 10.1 GHz of 78 circuits demonstrate the Doherty MMIC PA is able to maintain an efficiency of about 50% across 5 dB of output power.

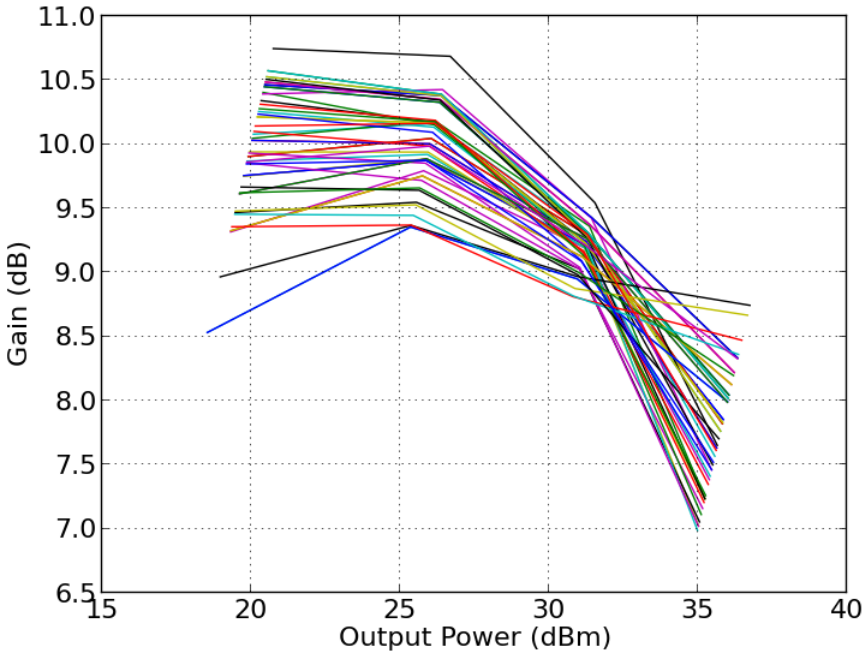

(a)

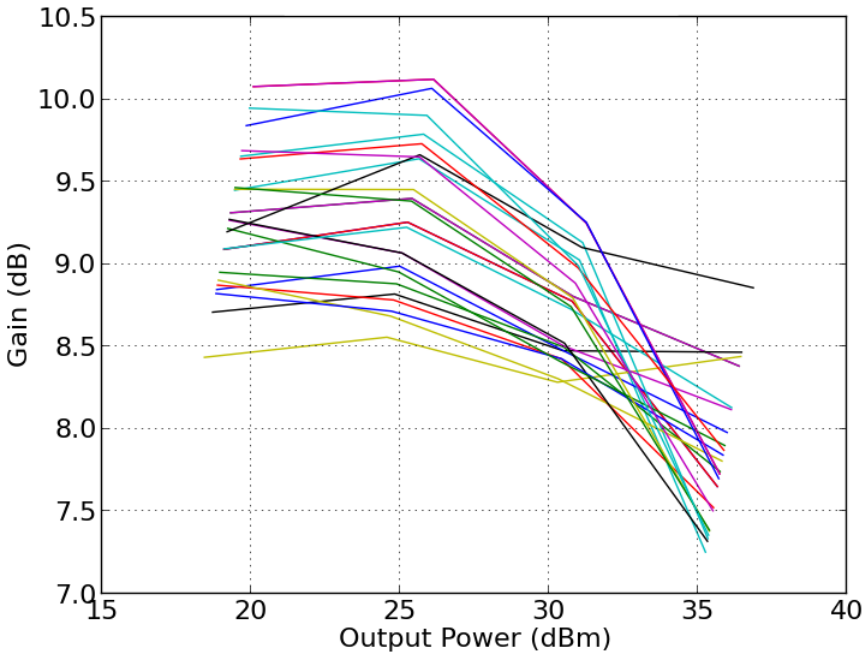

(b)

Figure 5.11: Measured gain results at (a) 9.9 GHz and (b) 10.1 GHz of 78 circuits. The backed of gain varies from 8.5-10 dB while the compressed gain varies from 7-9 dB.

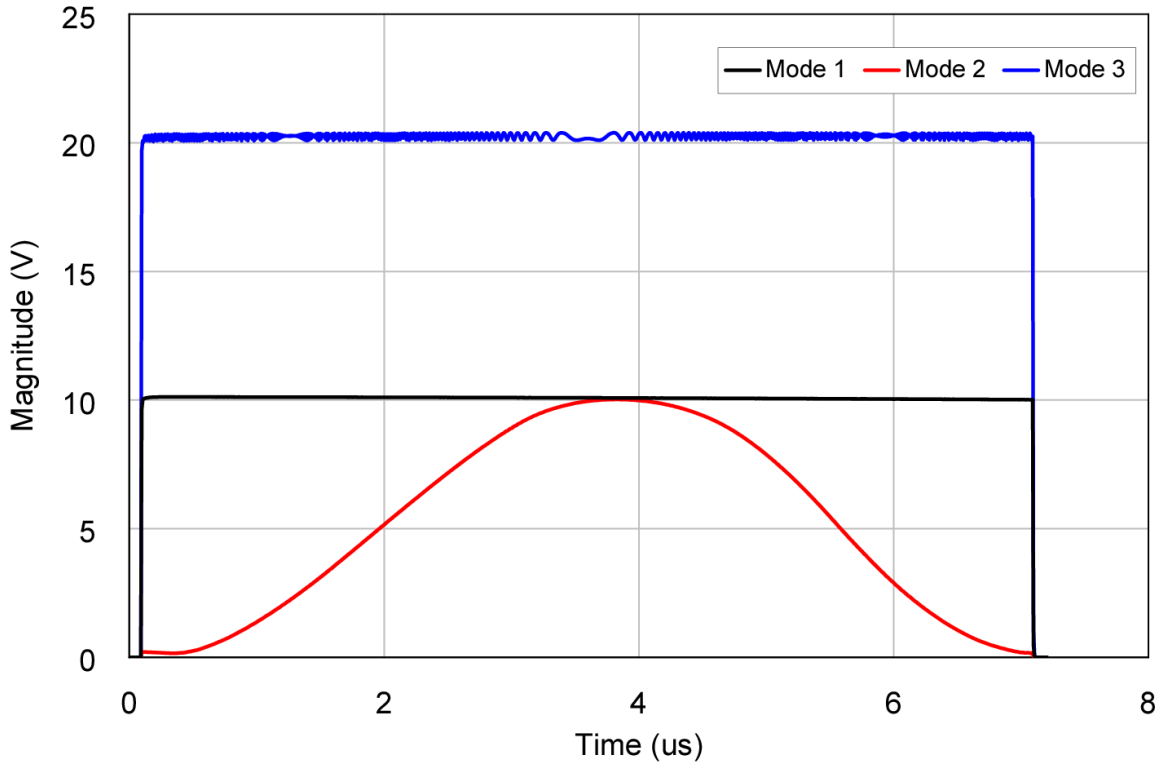

Figure 5.12: RF load voltage magnitudes for the three modes of radar operation. The peak pulse power of Modes 1 and 2 is 6 dB lower than that of Mode 3. The efficiency of Mode 2 is one point lower than that of Mode 1 even though it is a shaped pulse. The preserved efficiency of the shaped pulse is due to the supply modulation from the resonant modulator.

Chapter 6

Conclusions and Future Work

6.1 Conclusions

This thesis presents an approach to efficient, spectrally-confined radar transmitters. Both theoretical and experimental results demonstrate that a time-scaled Gaussian LFM pulse can achieve similar pulse energy and range resolution to a rectangular LFM without requirements on increasing the chirp bandwidth. A theoretical analysis shows that a supply-modulated Class-B PA could achieve a maximum efficiency of 62% for a knee voltage $V_k = V_{max}/12$, and can be extended to any $V_k : V_{max}$ ratio.

A simple variable-pulse-width resonant supply modulator is presented with a new method for solving the switching times of the resonant circuit. The new method allows for variable pulse width operation at the expense of peak voltage. Digitally switching the passive component values allows for further amplitude and pulse-width flexibility. The resonant modulator with a peak efficiency of 92% is connected to the drain supply input of a 4-W GaN X-band MMIC PA, resulting in 36% overall time-average system efficiency, a 5-point improvement compared to the directly-driven PA case. The theoretical investigation pointed to operating the PA in Class B, with a peak measured efficiency of 48% at 10 GHz, and an average PAE=40% when supply modulation is used for pulse envelope modulation. For an LFM pulse, the spectral emissions are reduced by 40 dB relative to the case of a rectangular pulse with the same energy as the Gaussian pulse. In addition to spectral confinement, a 5-MHz chirp bandwidth results in a range resolution of 80 m and the first time side lobe at -29 dB, a 15.5 dB improvement compared to the rectangular pulse shape. The

range resolution can be reduced with a broader-bandwidth chirp, since the PA bandwidth is about 300 MHz [15].

The supply modulator is implemented with low-cost, off-the-shelf components with efficiencies from 86-92%. Supply modulator efficiency can be further improved to an estimated 95% efficiency by using lower-loss MOSFET switches, gate drivers with higher output voltages and a decreased R_{on} and lower-loss surface mount lumped-element components, all of which are commercially available. Additionally, PA efficiency can be improved by using harmonically-terminated, heavily-saturated PAs, at the expense of more requirements on the digital pre-distortion. The efficiency results presented here are for a single pulse and a single PA. In a phased array radar, a watt-level PA such as the one presented here is used at each element, and the efficiency improvement in an array and for many pulses will result in considerable power savings at the system level, with modest complexity increase due to the very simple and efficient supply modulator architecture.

A supply-modulation simulation environment is developed in NI/AWR VSS along with a test bench which allows for the prediction and verification of supply-modulation efficiency environment. The environment is validated on a 4-W GaN MMIC PA connected to a resonant supply modulator for a radar application. The same environment can be applied to communications systems. Full-system circuit-envelope simulations are performed for communications system with a 10-W GaN MMIC and switching supply modulator, demonstrating a full-system efficiency improvement from 36% to 49% over a constant-supply PA with a communications signal having 18 MHz IQ bandwidth. Similar measurements are performed with a 4-W 10-W GaN MMIC PA. PA-only efficiencies with a linear modulator demonstrated at least 15-point improvement in both PAs and a switching supply modulator demonstrated a full-system drain efficiency of 60%.

Supply modulation is generally limited in PAPR when traded with efficiency. To extend the concept of a supply-modulated transmitter to larger PAPR, a Doherty amplifier which by itself efficiently amplifies a PAPR of 5 dB is designed. The 10-GHz 4-W GaN MMIC PA is designed to achieved greater than 50% PAE across 5 dB of output power, from 31-36 dBm in on-wafer tests. When combined with the supply modulator, this PA is a first step towards a variable-power radar

system.

6.2 Future Work

For future work, we recommend the following topics are investigated in relation to the resonant supply-modulated radar transmitter:

- Extend theory from Section 2.4 into a more generalized supply-modulated efficiency calculation. As the theory stands, it only predicts efficiency of a PA while in a linear operating mode and does not compress the PA. The calculation should be expanded to include the drain current and voltage waveform shapes when they enter the non-linear saturation, cut-off, and knee regions. With the extra non-linear information included in the waveforms one can calculate the fundamental output power and DC power consumption to predict efficiency of a non-linear, supply-modulated PA.

- Apply resonant supply modulation to a high-efficiency, switched-mode PA and investigate the output spectrum in terms of out-of-band and spurious emissions. We predict that there will be an efficiency improvement from the enhanced PA efficiency that will come at the expense of higher out-of-band emissions. Digital pre-distortion techniques should be investigated to remove any added out-of-band emissions [68]. The PA efficiency improvement should be weighed against the increased power and complexity required for DPD.

- Study how best to use the resonant supply modulator in a phased array. This work examined using one modulator per PA which corresponds to a resonant modulator for each element of the array. However, if the system has sufficiently narrow bandwidth relative to the carrier frequency, it should be possible to share a modulator amongst many elements, or a sub array. This would help with reliability and heat dissipation because it separates out the power dissipation from the PAs to the modulator as shown in Figure 6.1. This should assist with the peak-power mode of the variable power radar since the devices will be operating at a cooler temperature than they otherwise would without a modulator.

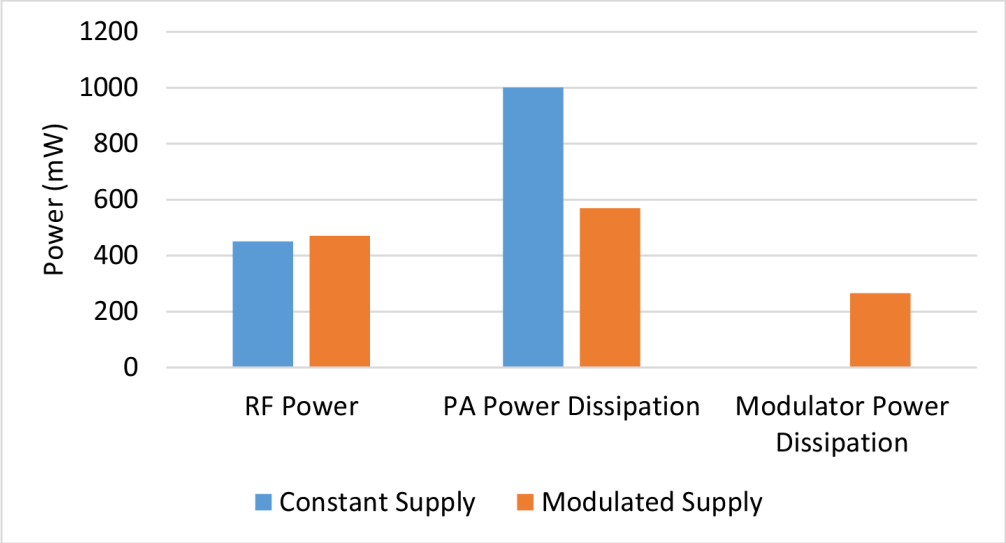

Figure 6.1: Supply modulation not only improves the efficiency relative to PA with constant supply, but it also distributes the power dissipation between the PA and modulator, making it possible to operate the PA with higher reliability.

In addition, we recommend the following topics related to the variable-mode-radar are investigated:

- Testing single devices for reliability when operating at an increased transmit power. We believe that the devices should be cycled between nominal and peak-power pulses to ensure devise reliability. Nominal power mode should drive the PAs in compression with a duty cycle between 1 and 10% and should constitute the majority of testing time. Peak power mode should account for less than 10% of testing time and use a duty cycle that ensures the same average power as nominal power mode. To add additional power, the supply voltage should be increased in conjunction with load modulation which provides the optimal load

for the new supply level. These measurements should be accompanied by a thermal analysis using a CAD tool such a finite element method solver to see how the temperature profile of the device changes for varying power levels.

- Investigate an isolated power-combining architecture in which extra devices may be turned off when operating in nominal power mode. The isolated combiner ensures that all PAs see their optimal load impedance, regardless of the states of other PAs in the transmitter network. This architecture also allows for redundancy since the transmitter can still operate at nominal power levels with one device dead. This should be used in conjunction with the previously mentioned technique of stressing the device at a higher output power for low time periods. To ensure heat is evenly dissipated, the transmitter should cycle between PA 1 and PA 2 in nominal power operation.

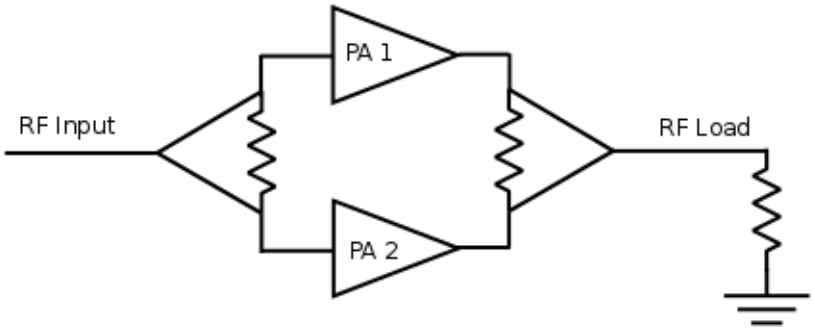

Figure 6.2: Architecture for a power combined variable power radar. In nominal power mode, only one of the two PAs is turned on. For peak power, both are turned on.

- Measurement of the X-Band Doherty MMIC and testing with the resonant supply modulator in the three modes of variable-power operation: Mode 1 should use rectangular LFMs with an output power of 31 dBm, Mode 3 should use the same pulse but operated at 36 dBm of output power, and Mode 2 should use Gaussian shaped LFMs and a resonant modulator. Initial Mode 2 tests should be performed with a peak power of 31 dBm, but they should be compared to supply-modulated results at 36 dBm output power.

6.3 Summary of Thesis Contributions

The thesis contributions can be summarized as follows:

- Chapter 2 presents the theory comparing a rectangular pulse to a Gaussian shaped envelope. A Gaussian-type envelope results in elimination of out-of-band emissions which are characteristic of rectangular pulses. Also, the pulse-compressed response of a measured Gaussian LFM has time side lobes 15 dB below that of a rectangular LFM. The use of a Gaussian shaped pulse decreases the efficiency of the PA, but analysis shows that the efficiency can be recovered by supply modulation. Theoretical efficiency of different classes of amplifiers under supply modulation is also presented, with a conclusion that Class-B PAs are well suited for this transmitter architecture. The theoretical efficiency calculations were presented in talks titled "Supply-Modulated Power Amplifiers for Amplitude Modulation Radar Transmitters" presented at both USNC-URSI National Radio Science Meeting and GOMAC-Tech Conference. Additionally, the entirety of the chapter is discussed in "Supply-Modulated Power Amplifiers for Radar Transmitters with Amplitude-Modulated Pulses", which has been submitted to *IEEE Transactions on Microwave Theory and Techniques.*

- Chapter 3 describes a simulation environment developed for supply-modulated transmitters. System level simulations which include the digital baseband signal are combined with microwave harmonic balance simulations with non-linear GaN transistor models. The simulation environment is designed to correspond closely to a hardware test bench which is also described in this chapter and used to evaluate well-known communications type signals amplified by supply-modulated transmitters. The supply-modulation measurements are discussed in "High-Efficiency X-Band MMIC GaN Power Amplifiers with Supply Modulation" of the *2014 IEEE MTT-S International Digest (IMS)*. The measurement bench was also used for results in "Simulation and measurement-based X-parameter models for power amplifiers with envelope tracking" of *2013 IEEE MTT-S International Digest (IMS)* and "RFPA supply modulator using wide-bandwidth linear amplifier with a GaN HEMT

output stage" in *2013 IEEE Workshop on Control and Modeling for Power Electronics.*

- Chapter 4 develops the implementation of a Gaussian-type envelope transmitters for radar. A Class-B X-Band GaN MMIC is measured in two modes: (1) drive-modulated and (2) supply-modulated. For supply modulation, a simple resonant modulator is developed and implemented with inexpensive off-the-shelf components. The supply modulator is capable of producing pulses of various widths and amplitudes, between 7-15 μs and up to 20 V. The pulse width is controlled digitally. Both simulations and measurements of a resonant supply-modulated X-Band GaN MMIC demonstrate that this topology provides an improved efficiency relative to a system using a constant supply. Resonant supply modulator theory was first presented in *Transactions on Power Electronics*, but the theory has been expanded to include variable pulse-width modulators and will has been submitted to *IEEE Transactions on Microwave Theory and Techniques.* The MTT Journal paper will also include simulations and measurements of the supply-modulated MMIC PA.

- Chapter 5 introduces a new variable power radar concept which uses resonant supply modulation. The envisioned radar transmitter is required to support three distinct power modes designed to provide increased capabilities for shorts bursts of time. An X-Band GaN Doherty MMIC is designed as the basic PA that can support these advanced radar transmitter specifications. The design is related to work published in *2013 IEEE Workshop on Control and Modeling for Power Electronics* titled "X-band MMIC GaN power amplifiers designed for high- efficiency supply-modulated transmitters." Because initial on-wafer measurements are so promising, we plan to submit full measured results of the Doherty MMIC to *Electronics Letters.*

- Chapter 6 presents other concepts to explore for variable power radar and how the resonant supply modulator can be used in a phased array. Variable power radar and resonant supply modulation can be used in a phased array in conjunction in with other techniques, outlined in US Patent 8,817,927 by Zai et al.

Bibliography

[1] M. Skolnik, Radar Handbook: Third Edition. McGraw Hill, 2008.

[2] S. Haykin and M. Moher, Modern Wireless Communications. Pearon Prentice Hall, 2005.

[3] R. Symons, "Tubes: still vital after all these years," Spectrum, IEEE, vol. 35, no. 4, pp. 52–63, Apr 1998.

[4] N. Pond, The Tube Guys. Russ Cochran, Publisher, 2008.

[5] R. Abrams, B. Levush, A. Mondelli, and R. Parker, "Vacuum electronics for the 21st century," Microwave Magazine, IEEE, vol. 2, no. 3, pp. 61–72, Sep 2001.

[6] S. Gold and G. Nusinovich, "Review of high-power microwave source research," Review of Scientific Instruments, vol. 68, no. 11, pp. 3945–3974, Nov 1997.

[7] A. S. Gilmour, Principles of Traveling Wave Tubes. Artech House, 1994.

[8] P. Draxler, S. Lanfranco, D. Kimball, C. Hsia, J. Jeong, J. van de Sluis, and P. Asbeck, "High efficiency envelope tracking ldmos power amplifier for w-cdma," in Microwave Symposium Digest, 2006. IEEE MTT-S International, June 2006, pp. 1534–1537.

[9] C. Dragon, W. Brakensiek, D. Burdeaux, W. Burger, G. Funk, M. Hurst, and D. Rice, "200w push-pull amp; 110w single-ended high performance rf-ldmos transistors for wcdma basestation applications," in Microwave Symposium Digest, 2003 IEEE MTT-S International, vol. 1, June 2003, pp. 69–72 vol.1.

[10] D. Gruner, R. Sorge, O. Bengtsson, A. Markos, and G. Boeck, "A 1 w si-ldmos power amplifier with 40 Microwave Symposium Digest (MTT), 2010 IEEE MTT-S International, May 2010, pp. 517–520.

[11] C. Nguyen and M. Micovic, "The state-of-the-art of gaas and inp power devices and amplifiers," Electron Devices, IEEE Transactions on, vol. 48, no. 3, pp. 472–478, Mar 2001.

[12] T. Yamasaki, Y. Kittaka, H. Minamide, K. Yamauchi, S. Miwa, S. Goto, M. Nakayama, M. Kohno, and N. Yoshida, "A 68power amplifier for space applications," in Microwave Symposium Digest (MTT), 2010 IEEE MTT-S International, May 2010, pp. 1384–1387.

[13] K. Yamauchi, H. Noto, H. Nonomura, S. Kunugi, M. Nakayama, and Y. Hirano, "A 45Microwave Symposium Digest (MTT), 2011 IEEE MTT-S International, June 2011, pp. 1–4.

[14] A. Brown, K. Brown, J. Chen, K. Hwang, N. Kolias, and R. Scott, "W-band gan power amplifier mmics," in Microwave Symposium Digest (MTT), 2011 IEEE MTT-S International, June 2011, pp. 1–4.

[15] S. Schafer, M. Litchfield, A. Zai, Z. Popovic, and C. Campbell, "X-band mmic gan power amplifiers designed for high-efficiency supply-modulated transmitters," in Microwave Symposium Digest (IMS), 2013 IEEE MTT-S International, June 2013, pp. 1–3.

[16] M. N. Sadiku, Elements of Electromagnetics. Oxford University Press, 2005.

[17] P. Lavrador, T. Cunha, P. Cabral, and J. Pedro, "The linearity-efficiency compromise," Microwave Magazine, IEEE, vol. 11, no. 5, pp. 44–58, Aug 2010.

[18] S. C. Cripps, RF Power Amplifiers for Wireless Communications. Artech House, 2006.

[19] F. Raab, P. Asbeck, S. Cripps, P. Kenington, Z. Popovic, N. Pothecary, J. Sevic, and N. Sokal, "Power amplifiers and transmitters for rf and microwave," Microwave Theory and Techniques, IEEE Transactions on, vol. 50, no. 3, pp. 814–826, Mar 2002.

[20] A. Grebennikov, N. O. Sokal, and M. J. Franco, Switchmode RF and Microwave Power Amplifiers. Academic Press, 2012.

[21] L. Kahn, "Single-sideband transmission by envelope elimination and restoration," Proceedings of the IRE, vol. 40, no. 7, pp. 803–806, July 1952.

[22] H. Chireix, "High power outphasing modulation," Radio Engineers, Proceedings of the Institute of, vol. 23, no. 11, pp. 1370–1392, Nov 1935.

[23] R. Langridge, T. Thornton, P. Asbeck, and L. Larson, "A power re-use technique for improved efficiency of outphasing microwave power amplifiers," Microwave Theory and Techniques, IEEE Transactions on, vol. 47, no. 8, pp. 1467–1470, Aug 1999.

[24] A. S. W. Alan V. Oppenheim, Signals and Systems. Prentice Hall, 1997.

[25] N. Levanon and E. Mozeson, Radar Signals. Wiley-Interscience, 2004.

[26] C. Balanis, Antenna Theory: Analysis and Design. Wiley, 2005.

[27] P. Pace, Detecting and Classifying Low Probability of Intercept Radar: Second Edition. Artech House, 2009.

[28] H. Poor, An Introduction to Signal Detection and Estimation: Second Edition. Springer, 1994.

[29] M. Richards, Fundamentals of Radar Signal Processing. McGraw Hill, 2005.

[30] "Manual of regulations and procedures for federal radio frequency management," U.S. DEPARTMENT OF COMMERCE National Telecommunications and Information Administration, Tech. Rep., 2013.

[31] R. H. F.H. Sanders and B. Ramsey, "Analysis of electromagnetic compatibility between radar stations and 4 ghz fixed-satellite earch stations," U.S. DEPARTMENT OF COMMERCE National Telecommunications and Information Administration, Tech. Rep., 1994.

[32] N. News, "Fcc warns of mobile's looming spectrum crisis," NBC News, Oct. 2009. [Online]. Available: http://www/nbcnews.com

[33] C. Baylis, M. Fellows, L. Cohen, and R. Marks, "Solving the spectrum crisis: Intelligent, reconfigurable microwave transmitter amplifiers for cognitive radar," Microwave Magazine, IEEE, vol. 15, no. 5, pp. 94–107, July 2014.

[34] J. De Graaf, H. Faust, J. Alatishe, and S. Talapatra, "Generation of spectrally confined transmitted radar waveforms: experimental results," pp. 8 pp.–, April 2006.

[35] Probability, Statistics, and Random Processes for Electrical Engineering. Prentice Hall, 2008.

[36] D. C. Schleher, Electronic Warfare in the Information Age. Artech House, 1999.

[37] J. Hoversten, S. Schafer, M. Roberg, M. Norris, D. Maksimovic, and Z. Popovic, "Codesign of pa, supply, and signal processing for linear supply-modulated rf transmitters," Microwave Theory and Techniques, IEEE Transactions on, vol. 60, no. 6, pp. 2010–2020, June 2012.

[38] K. Bumman, M. Junghwan, and K. Ildu, "Efficiently amplified," Microwave Magazine, IEEE, vol. 11, no. 5, pp. 87–100, Aug 2010.

[39] D. Morgan, Z. Ma, J. Kim, M. Zierdt, and J. Pastalan, "A generalized memory polynomial model for digital predistortion of rf power amplifiers," Signal Processing, IEEE Transactions on, vol. 54, no. 10, pp. 3852–3860, Oct 2006.

[40] P. Draxler, "Behavioral modeling of nonlinearitites and memory effects in power amplifiers," Ph.D. dissertation, University of California, San Diego, 2012.

[41] D. Li, M. Rodriguez, A. Zai, D. Sardin, D. Maksimovic, and Z. Popovic, "Rfpa supply modulator using wide-bandwidth linear amplifier with a gan hemt output stage," in Control and Modeling for Power Electronics (COMPEL), 2013 IEEE 14th Workshop on, June 2013, pp. 1–6.

[42] M. Rodriguez, Y. Zhang, and D. Maksimovic, "High-frequency pwm buck converters using gan-on-sic hemts," Power Electronics, IEEE Transactions on, vol. 29, no. 5, pp. 2462–2473, May 2014.

[43] T. Moon and W. Stirling, Mathmatical Methods and Algorithms for Signal Processing. Prentice Hall, 2000.

[44] Microelectronic Circuits. Oxford University Press, 1991.

[45] F. Wang, A. Yang, D. Kimball, L. Larson, and P. Asbeck, "Design of wide-bandwidth envelope-tracking power amplifiers for ofdm applications," Microwave Theory and Techniques, IEEE Transactions on, vol. 53, no. 4, pp. 1244–1255, April 2005.

[46] F. Raab, "Intermodulation distortion in kahn-technique transmitters," Microwave Theory and Techniques, IEEE Transactions on, vol. 44, no. 12, pp. 2273–2278, Dec 1996.

[47] T. Rautio and T. Rahkonen, "The effects of timing skew in envelope tracking and eer type transmitters," in Microwave Conference, 2009. EuMC 2009. European, Sept 2009, pp. 346–349.

[48] Agilent N8241A/N8242A Arbitrary Waveform Generators Users Guide.

[49] J. Jeong, D. Kimball, M. Kwak, C. Hsia, P. Draxler, and P. Asbeck, "Wideband envelope tracking power amplifier with reduced bandwidth power supply waveform," in Microwave Symposium Digest, 2009. MTT '09. IEEE MTT-S International, June 2009, pp. 1381–1384.

[50] F. Demuynck and M. Petersen, "Choosing the right em simulation technology for antenna design and analysis," in Antennas and Propagation (EUCAP), 2012 6th European Conference on, March 2012, pp. 1296–1300.

[51] I. Angelov, H. Zirath, and N. Rosman, "A new empirical nonlinear model for hemt and mesfet devices," Microwave Theory and Techniques, IEEE Transactions on, vol. 40, no. 12, pp. 2258–2266, Dec 1992.

[52] I. Angelov, L. Bengtsson, and M. Garcia, "Extensions of the chalmers nonlinear hemt and mesfet model," Microwave Theory and Techniques, IEEE Transactions on, vol. 44, no. 10, pp. 1664–1674, Oct 1996.

[53] J. Pedro and T. Reis Cunha, "Predictable behavior: Behavioral modeling from measured data," Microwave Magazine, IEEE, vol. 15, no. 6, pp. 75–90, Sept 2014.

[54] D. Held and A. Kerr, "Conversion loss and noise of microwave and millimeterwave mixers: Part 1 - theory," Microwave Theory and Techniques, IEEE Transactions on, vol. 26, no. 2, pp. 49–55, Feb 1978.

[55] Circuit Envelope Simulation.

[56] D. Kimball, J. Jeong, C. Hsia, P. Draxler, S. Lanfranco, W. Nagy, K. Linthicum, L. Larson, and P. Asbeck, "High-efficiency envelope-tracking w-cdma base-station amplifier using gan hfets," Microwave Theory and Techniques, IEEE Transactions on, vol. 54, no. 11, pp. 3848–3856, Nov 2006.

[57] P. Godoy, D. Perreault, and J. Dawson, "Outphasing energy recovery amplifier with resistance compression for improved efficiency," Microwave Theory and Techniques, IEEE Transactions on, vol. 57, no. 12, pp. 2895–2906, Dec 2009.

[58] D. Kang, J. Choi, D. Kim, and B. Kim, "Design of doherty power amplifiers for handset applications," Microwave Theory and Techniques, IEEE Transactions on, vol. 58, no. 8, pp. 2134–2142, Aug 2010.

[59] J. Choi, D. Kang, D. Kim, and B. Kim, "Optimized envelope tracking operation of doherty power amplifier for high efficiency over an extended dynamic range," Microwave Theory and Techniques, IEEE Transactions on, vol. 57, no. 6, pp. 1508–1515, June 2009.

[60] C. Hsia, A. Zhu, J. Yan, P. Draxler, D. Kimball, S. Lanfranco, and P. Asbeck, "Digitally assisted dual-switch high-efficiency envelope amplifier for envelope-tracking base-station power amplifiers," Microwave Theory and Techniques, IEEE Transactions on, vol. 59, no. 11, pp. 2943–2952, Nov 2011.

[61] M. Roberg, M. Rodriguez, D. Maksimovic, and Z. Popovic, "Efficient and linear amplification of spectrally confined pulsed am radar signals," Microwave and Wireless Components Letters, IEEE, vol. 22, no. 6, pp. 279–281, June 2012.

[62] M. Rodriguez, M. Roberg, A. Zai, E. Alarcon, Z. Popovic, and D. Maksimovic, "Resonant pulse-shaping power supply for radar transmitters," Power Electronics, IEEE Transactions on, vol. 29, no. 2, pp. 707–718, Feb 2014.

[63] P. Colantonio, F. Giannini, R. Giofre, E. Limiti, and L. Piazzon, "An x-band gaas mmic doherty power amplifier," in Integrated Nonlinear Microwave and Millimeter-Wave Circuits (INMMIC), 2010 Workshop on, April 2010, pp. 41–44.

[64] L. Piazzon, P. Colantonio, F. Giannini, and R. Giofre, "Design of an x-band gaas mmic doherty amplifier accounting for device ron resistance," in Microwave Conference (EuMC), 2010 European, Sept 2010, pp. 862–865.

[65] R. Middlebrook, "The general feedback theorem: a final solution for feedback systems," Microwave Magazine, IEEE, vol. 7, no. 2, pp. 50–63, April 2006.

[66] V. Camarchia, J. Fang, J. Moreno Rubio, M. Pirola, and R. Quaglia, "7 ghz mmic gan doherty power amplifier with 47Microwave and Wireless Components Letters, IEEE, vol. 23, no. 1, pp. 34–36, Jan 2013.

[67] C. Campbell, "A fully integrated ku-band doherty amplifier mmic," Microwave and Guided Wave Letters, IEEE, vol. 9, no. 3, pp. 114–116, March 1999.

[68] J. Wood, "What's new in digital pre-distortion." Denver Chapter of IEEE MTT, December 2014.

[69] R. Caverly, F. Raab, and J. Staudinger, "High-efficiency power amplifiers," Microwave Magazine, IEEE, vol. 13, no. 7, pp. S22–S32, Nov 2012.

[70] M. Roberts, Signals and Systems. McGraw Hill, 2004.

[71] G. Stimson, Introduction to Airbourne Radar: Second Edition. SciTech, 1998.

[72] C. Baylis, L. Wang, M. Moldovan, J. Martin, H. Miller, L. Cohen, and J. de Graaf, "Designing transmitters for spectral conformity: power amplifier design issues and strategies," Radar, Sonar Navigation, IET, vol. 5, no. 6, pp. 681–685, July 2011.

[73] R. Chen and B. Cantrell, "Highly bandlimited radar signals," in Radar Conference, 2002. Proceedings of the IEEE, 2002, pp. 220–226.

[74] J. A. J. de Graaf, H. Faust and S. Talapatra, "Generation of spectrally confined transmitted radar waveforms: Experimental results," in Radar, 2006 IEEE Conference on, Apr. 2006, p. 8.